

Bayesian Inference for Truck-based Methane Quantification Uncertainty

by

Daniel Christopher Blackmore

A thesis

presented to the University of Waterloo

in fulfilment of the

thesis requirement for the degree of

Master of Applied Science

in

Mechanical and Mechatronics Engineering

Waterloo, Ontario, Canada, 2024

© Daniel Christopher Blackmore 2024

Author's Declaration

I hereby declare that this I am the sole author of this thesis. This is a true copy of the thesis, including any required final revisions, as accepted by my examiners.

I understand that this thesis may be made electronically available to the public.

Abstract

Methane emissions from the oil and gas sector are one of the most important factors to address with respect to human-driven forces of climate change. Within Canada, the United States, and other jurisdictions worldwide, significant progress has been made in the measurement and regulation of methane emissions. While this progress has been beneficial for methane emission reduction, far less work has been performed in the understanding of uncertainties associated with methane emission measurements. Understanding these uncertainties is crucial for regulation, repair activities, and inventorying of emissions to be performed.

This thesis covers a multi-year project related to the investigation of methane emissions quantification uncertainty, with a focus on the development of an uncertainty model for truck-based emissions estimates using a generalized Bayesian inference. A literature review of uncertainty analysis for methane quantification technologies is presented, as well as a detailed overview of specific technologies that were investigated during controlled release field measurement campaigns. The controlled release measurements are detailed, as well as the empirical results for the technologies that were evaluated.

Subsequent chapters focus on truck-based tunable diode laser absorption spectroscopy measurements, combined with atmospheric data in the Gaussian plume model. The Gaussian plume model is derived, and the method of modelling the errors associated with this measurement technique is described. Bayesian inference is used to quantify the emission estimate uncertainty, which relies upon a CFD investigation into the errors associated with the Gaussian plume model. This thesis presents the details of how the Bayesian inference is performed – namely the form of the likelihood function, the treatment of priors, and the construction of credible intervals on the

resulting posterior distributions. Then, the procedure for investigating the model error using high-fidelity detached eddy simulations is detailed.

Next, the results of the Bayesian inference on the controlled release data are presented. It was found through the analysis of the applicability of the credible intervals to the true emission rates that the procedure resulted in an accurate representation of the true uncertainty of the measurement technique. Further investigation into the factors affecting the uncertainty of emission estimates revealed the measurement distance to be a significant contributor to the uncertainty, as well as very low wind speeds being a potential limitation to the technique.

This thesis concludes with some discussion of the implications of the results, what limitations are present in the study, and some recommendations for future research relating to this work.

Acknowledgements

Acknowledgements must first be given to the supervisor of this thesis, Dr. Kyle Daun, for providing the opportunity to work on this project, and within the Waterloo Laboratory for Inverse Analysis and Thermal Sciences (WatLIT). Dr. Daun's guidance, dedication, and hard work has contributed significantly to the success of this thesis, and myriad of other contemporary research projects within WatLIT.

Dr. Jean-Pierre Hickey of the University of Waterloo provided significant expertise in CFD modelling and aided in the analysis of the CFD data presented in this work. He was also directly responsible for the generation of plume visualizations from the CFD data that are used in this thesis, and was a main contributor to a research paper related to this thesis that will shortly be published.

Members of the Department of Statistics and Actuarial Sciences at the University of Waterloo, Dr. Christiane Lemieux, Dr. Audrey Béliveau, and Augustine Wigle as well as Dr. Paule Lapeyre from the Department of Mechanical engineering and WatLIT, were key in developing and supporting the understanding of Bayesian inference needed for this work.

The efforts of Kirk Osadetz from Carbon Management Canada in organizing and facilitating the field measurement campaigns were incredibly important, as the data from which this thesis is built upon relied on the execution of these campaigns. Furthermore, Hamish Adam and Brian Sinfield from Boreal Laser provided assistance in analyzing the controlled release data for the results presented in this work, as well as their industrial perspective.

Finally, the other students who work at WatLIT, Arpan Singh, Alireza Kaveh, Stephen Robinson-Enebeli, Paule Lapeyre, Nishant Sriram Narayanan, Michael Nagorski, Ardhendu Bhattacharya, Jun Wang, Fatima Suleiman, Halil Yazici, Michio Kagaya, and Horace Looi, have

each in their own way contributed to the success of this work, through team discussions, conference presentation reviews, individual whiteboarding sessions, and more.

Below is a detailed list of specific contributions to this thesis:

- Kirk Osadetz is responsible for the setup and facilitation of the field measurements detailed in Chapter 2, as well as the identification of the gas composition shown in Table 2-1
- The empirical results of the field measurements shown in Chapter 2 are the results of analysis performed by a number of operators: AGAT technologies, Michael Nagorski (University of Waterloo), and Montrose Environmental (QOGI); Boreal Laser (truck-based TDLAS with the BLS model); GHGSat and Telops (aerial hyperspectral measurements).
- Equation (4-2) is built directly from the likelihood function derived by Zhou et al. [1]
- Dr. Jean-Pierre Hickey performed the RANS and DES simulations described in Chapter 5, as well as the plume visualizations shown in Figure 5-1

Table of Contents

Author’s Declaration.....	ii
Abstract.....	iii
Acknowledgements.....	v
List of Figures.....	x
List of Tables	xiii
1 Introduction and Motivation.....	1
1.1 Methane Emissions in the Oil and Gas Industry	1
1.2 Project Scope and Purpose	2
1.3 Methane Quantification Technologies	3
1.3.1 Review and Characterization of Quantification Technologies	3
1.3.2 MWIR QOGI	6
1.3.3 Aerial Hyperspectral Measurements.....	7
1.3.4 Truck-based TDLAS Measurements	7
1.4 Uncertainty Quantification.....	9
1.4.1 Overview of Uncertainty.....	9
1.4.2 Introduction to Bayesian Inference for Uncertainty Analysis	12
1.4.3 Empirical Uncertainty Analysis.....	13
1.4.4 Model-based Uncertainty Analysis.....	14
1.5 Research Objectives	17
1.6 Overview of Thesis	18

2	Controlled-release Experiments	20
2.1	Overview of field measurement campaign.....	20
2.2	Meteorological data.....	24
2.3	Empirical Results of the Field Measurement Campaign.....	28
2.3.1	QOGI Measurements	28
2.3.2	Aerial NIR and LWIR Hyperspectral Measurements	31
2.3.3	Truck-based TDLAS Measurements	35
3	Vehicle-based Methane Emissions Quantification.....	39
3.1	Characteristics of plume dispersion	39
3.2	Overview of vehicle-based methane emissions quantification	41
3.3	Gaussian Plume Model	43
3.4	Uncertainty Analysis and Model Error	46
4	Emission Rate Inference.....	48
4.1	Likelihood Function	48
4.2	Treatment of Priors	49
4.3	The Posterior PDF.....	51
5	CFD Investigation into Model Error	54
5.1	Initial RANS simulations	54
5.2	Detached Eddy Simulation (DES).....	55
5.3	Comparison of CFD concentration data to GPM predictions	57
6	Results of Field Data Analysis.....	62

6.1	Defining uncertainty for investigating the results	62
6.2	Overall results	63
6.3	Factors affecting uncertainty	67
6.3.1	True release rate.....	67
6.3.2	Downwind Distance.....	68
6.3.3	Wind Effects	70
7	Conclusions and Future Work.....	74
7.1	Key Findings	74
7.2	Limitations	75
7.3	Recommendations for Future Work.....	77
	References.....	79
	Appendix A: Summary Table of Candidate Methane Quantification Technologies	92
	Appendix B: QOGI Datasheets.....	100
	Appendix C: Aerial LWIR Datasheet	104
	Appendix D: Boreal Gasfinder3-VB Datasheet.....	106
	Appendix E: Release notebook from the April 2022 field measurement campaign.....	107
	Appendix F: Release notebook from the September 2022 field measurement campaign.....	140

List of Figures

Figure 1-1: Methane Quantification Technologies Categorized by Measurement Technique	4
Figure 1-2: Methane Quantification technologies categorized by application	4
Figure 1-3: Schematic of sources contributing to overall emission estimate uncertainty.	11
Figure 2-1 Location of CMC's field research station in Newell County, Alberta	21
Figure 2-2: Setup of methane releases	22
Figure 2-3: Modular stack configured for releases from 1.7m above the ground	23
Figure 2-4: Releases from a storage tank.....	23
Figure 2-5: Aerial view of the site with approximate release locations.	24
Figure 2-6: Wind speed and temperature data from April 21, 2022.....	25
Figure 2-7: Wind speed data from September 26, 2022	26
Figure 2-8: Ambient temperature data from September 26, 2022	26
Figure 2-9: Modulation of release rate (normalized to the scale of the graph) compared to wind and temperature measurements for September 28th, 2022	27
Figure 2-10: Release rates vs windspeed for the September 2022 measurements	28
Figure 2-11: Release rates vs temperature for the September 2022 measurements	28
Figure 2-12: Summary of UW operated FLIR emissions estimates for the April 2022 field measurement campaign.....	29
Figure 2-13: Summary of AGAT operated FLIR emissions estimates for the April 2022 field measurement campaign.....	29
Figure 2-14: Summary of UW operated FLIR emissions estimates for the September 2022 field measurement campaign.....	30

Figure 2-15: Summary of OPGAL emissions estimates for the September 2022 field measurement campaign.....	30
Figure 2-16: Summary of NIR hyperspectral emissions estimates for the April 2022 field measurement campaign.....	32
Figure 2-17: Summary of NIR hyperspectral emissions estimates for the September 2022 field measurement campaign.....	33
Figure 2-18: Summary of LWIR hyperspectral emissions estimates for the September 2022 field measurement campaign.....	33
Figure 2-19: Example of path taken by the truck during a release.	35
Figure 2-20: Summary of truck-based TDLAS emissions estimates for the April 2022 field measurement campaign using the BLS and IGM analysis	36
Figure 2-21: Summary of truck-based TDLAS emissions estimates for the April 2022 field measurement campaign using the BLS and IGM analysis	37
Figure 3-1: Diagram of GPM boundary condition for flux through a downwind plane.....	44
Figure 4-1: Visualization of the Gaussian prior on σ_y	50
Figure 4-2: Visualization of the posterior distribution, q^{MAP} , and credibility interval.....	51
Figure 4-3: Asymmetric distribution, typical of the posterior distributions of the emission rate.	53
Figure 5-1: Isocontours of methane concentration from CFD simulation at two separates time instances. Four cross-plane slices of the local concentration are shown for identical isocontour lines for both cases.....	57
Figure 5-2: Instantaneous map of ϵ at a measurement height of $z = 1$ m.	59
Figure 5-3: Average values for ϵ for a transect located 100 m downwind of the release point. Error bars correspond to a 90% credible interval.	60

Figure 5-4: Comparison of GPM to LES concentrations for an instantaneous transect located 100 m downwind of the source location.....	60
Figure 6-1: Representative set of q^{MAP} and CIs for the transects analyzed, with a visualization of the posterior PDF for transect number 8.....	65
Figure 6-2: Comparison of q^{MAP} to the true emission rates for the entirety of the analyzed transects.....	66
Figure 6-3: Relative uncertainty vs true release rate	67
Figure 6-4: Relative uncertainty vs transect distance	69
Figure 6-5: Relative uncertainty vs wind speed.....	71
Figure 6-6: Relative uncertainty vs wind speed variance	72
Figure 6-7: Relative uncertainty vs wind direction variance	72

List of Tables

Table 2-1: Gas composition for controlled release measurements	21
Table 3-1: Determination of stability class from wind speed and solar radiation [72] [74] [75] .	45
Table 6-1: Strengths of Correlations [87]	63
Table 6-2: Summary of transects performed for different releasing equipment.....	64
Table 6-3: Number of transects performed for each release rate.....	64
Table 6-4: Frequency of q being outside of the CI vs true release rate	68
Table 6-5: Frequency of q being outside of the CI vs measurement distance	69
Table 6-6: Frequency of q being outside of the CI vs wind speed	71

1 Introduction and Motivation

1.1 Methane Emissions in the Oil and Gas Industry

Methane (CH₄) emissions to the atmosphere are one of the most important factors with respect to anthropogenic forces in climate change, second only to atmospheric carbon dioxide (CO₂) emissions [2]. The global warming potential – a measure of the ability of a greenhouse gas (GHG) to trap heat in the atmosphere – of 1 kg of CH₄ is over 25 times higher than 1 kg of CO₂ over a 100-year period [3, 4]. Over a shorter, 20-year period, the global warming potential of CH₄ is over 80 times larger than CO₂ [4]. Canada accounts for 1.5% of the world’s GHG emissions, at 708 Mt of CO₂ equivalent in 2022, with CH₄ representing the second largest constituent of GHG emissions in the country [2]. Anthropogenic methane emissions in Canada are largely attributable to the oil and gas industry, landfills, and agriculture – with the oil and gas industry contributing the largest amount of CH₄ emissions with 56 Mt CO₂ equivalent per year [2]. It is clear to see the need for a reduction in CH₄ emissions, specifically in the oil and gas sector, to curb the effects of climate change [5, 6].

In an effort to reduce CH₄ emissions, the Canadian Government has implemented regulations aiming at a 75% reduction of methane emissions by 2030 [5]. Similarly, other jurisdictions internationally have begun implementing regulations on CH₄ emissions, such as the United States’ Methane Emissions Reduction Program (MERP) [7], and the European Union’s Methane Emissions Reduction Strategy (MERS) [8]. The MERP aims to reduce CH₄ emissions from the United States’ oil and natural gas sectors by providing technical and financial assistance to support CH₄ reporting and monitoring activities, as well as through the introduction of a progressively increasing waste emissions charge, starting in 2024 at \$900 per metric ton of reported CH₄ emissions [7, 9]. Similarly, the MERS aims to minimize the releases of CH₄ in Europe’s fossil fuel

inventory through the establishment of measurement, reporting, and verification processes; obligating operators in the fossil fuel sector to monitor emissions and implement mitigation strategies; and in the establishment of transparent public methane inventories [8, 10]. Other regulations across jurisdictions have included the regulation of leak detection and repair (LDAR) programs, such as how frequently these programs should be implemented, what size leaks require repair, and how quickly leaks need to be repaired after being identified [10, 11]. Adequate enforcement of these regulations, and implementation of these programs, relies on accurate data regarding fugitive CH₄ emissions from leaking components, as well as accurate data on overall emissions inventories [12]. To achieve this, significant work has been performed in the development of technologies capable of detecting and quantifying CH₄ emissions [12, 13], however the uncertainties associated with the estimates obtained from these technologies are less understood [14, 15].

1.2 Project Scope and Purpose

With a diverse range of applicability for methane quantification technologies, it is important for regulators to understand how accurate emissions estimates from a specific technology are for the specific measurements taking place. This relies on an understanding of the uncertainty associated with measured emissions. Understanding the uncertainties in emissions estimates can help to answer questions such as “how likely is it that an operator is complying with methane emissions regulations?”, “What is the best technology to use to measure specific emissions?”, and “How should leaks be prioritized within the context of LDAR programs?”.

To investigate methane emissions quantification uncertainty, a team of researchers from the University of Waterloo (UW), Arolytics, Inc. [16], and Carbon Management Canada (CMC) [17]

conducted a multi-year research project on the evaluation of methane emissions quantification technologies. This project was funded through the Clean Resources Innovation Network (CRIN) [18], Petroleum Technology Alliance Canada (PTAC) [19], and the Natural Sciences and Engineering Research Council (NSERC). The project was broken down into distinct phases. First, a comprehensive review of methane quantification technologies was performed. Then, specific technologies were chosen to participate in multiple field measurement campaigns. The third phase was the execution of the field campaign, where the selected technologies participated in controlled release measurements to gather data for analysis. The final phase of the project was the analysis of data for the purpose of modelling the uncertainty in these technologies.

1.3 Methane Quantification Technologies

1.3.1 Review and Characterization of Quantification Technologies

The first phase of the project was a review of emerging methane quantification technologies. These technologies include quantitative optical gas imaging (QOGI) [20], aerial hyperspectral measurements [21, 22], vehicle-based measurements [23, 1, 24], and satellite imaging [25]. Quantification technologies can be categorized a variety of ways, such as by the measurement/imaging technique (Figure 1-1), the specific applicability of the technology with respect to what type of emissions the technology can monitor (Figure 1-2), or more generally as “top-down” or “bottom-up”. “Bottom-up” emissions estimates are methane emissions estimates that are comprised of a representative sample of small-scale emitting devices/equipment, while “top-down” emissions estimates refer to more large-scale emissions estimates, such as regional measurements from an aerial or satellite-based technology [26]. Technologies were also evaluated based on factors such as reported precision, and the technology readiness level (TRL), a measure

of how developed a technology is, from basic principles to full-scale, successful deployment in real-world operations [27].

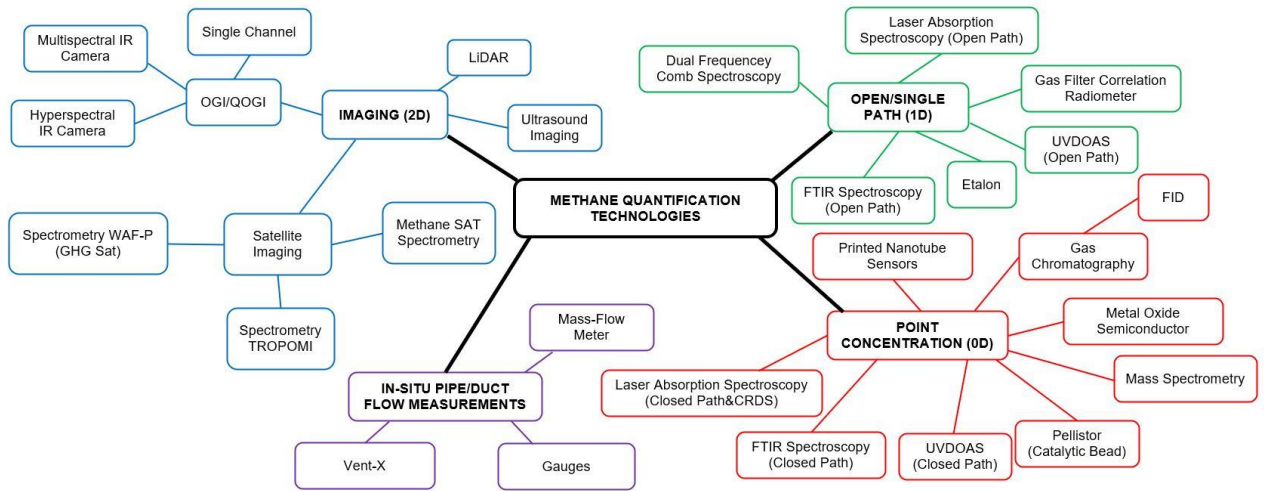


Figure 1-1: Methane Quantification Technologies Categorized by Measurement Technique

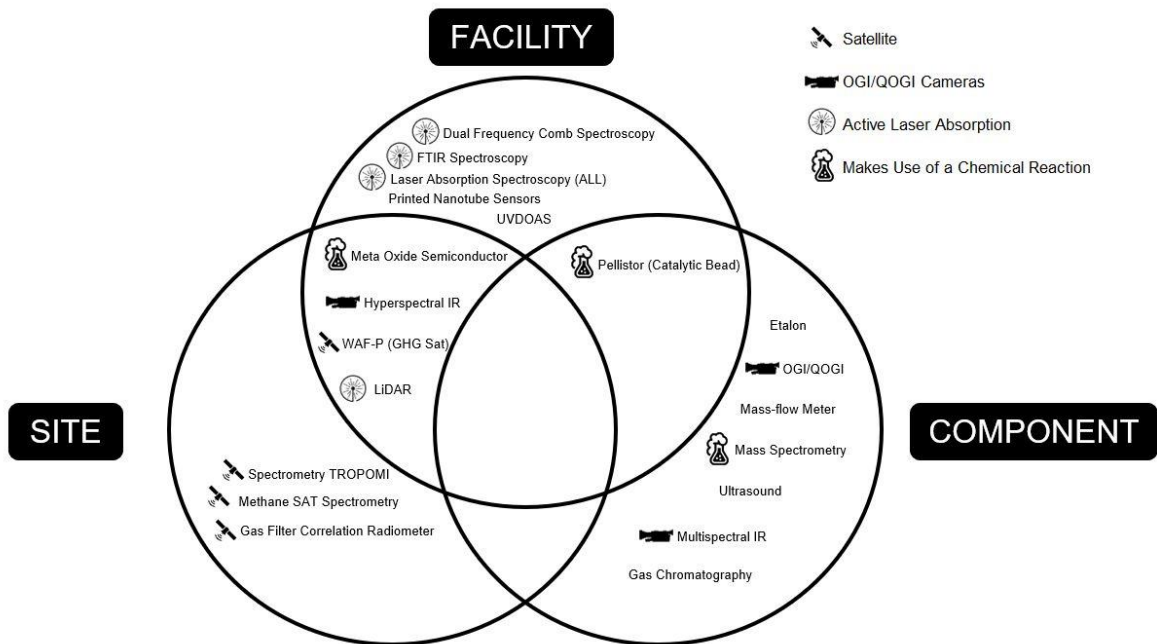


Figure 1-2: Methane Quantification technologies categorized by application

Generally, these technologies work by combining concentration measurements with some atmospheric transport model to derive the emission rate of a particular source. Closed path or point

concentration estimates are derived from the combination of a local CH₄ concentration measurement (e.g. a ppm measurement) with some dispersion model (such as the Gaussian plume model [28] or a Lagrangian stochastic model [29]) based on local anemometry or meteorological measurements. Open path measurements are similar in that the CH₄ measurements are combined with meteorological data to obtain emissions estimates, however the measurements themselves are made over longer distances (path lengths), with the resulting measurement being a column density measurement, integrated over the path length (e.g. ppm·m measurements). Imaging techniques work by generating a map of column densities, which can then be used with wind measurements or an inferred velocity field to obtain emissions estimates. Finally, in-situ measurements work by directly measuring flow in confined environments such as pipes and vents through the use of gauges. The outcome of the review was a summary of 23 different technologies/techniques, which are summarized in Appendix A.

From the technologies surveyed, a subset of technologies was chosen to be evaluated in field measurement campaigns, then further analyzed throughout the remainder of the project. These technologies were chosen to be representative of a variety of measurement techniques and applicability to emission sources. The technologies chosen included mid-wavelength infrared quantitative optical gas imaging (MWIR QOGI); truck-based tunable-diode laser absorption spectroscopy (TDLAS); and aerial hyperspectral measurements in the near-infrared (NIR) and long-wave infrared (LWIR). The planning and execution of these measurement campaigns is detailed in Chapter 2 of this thesis.

1.3.2 MWIR QOGI

The main principle of QOGI is in the measurement of plumes through the detection of thermal radiation emitted or absorbed by the gas. When the temperature of the gas is hotter than the background, the plume is detected as a radiation emission (known as a “white plume”), while colder plumes are detected through the absorption of radiation (known as “black plumes”) [30]. QOGI cameras measure thermal radiation across a range of wavelengths, and these measurement wavelengths correspond to the absorption bands of the target gas [31]. Mid-wavelength infrared cameras operate in the 3 μm to 5 μm measurement spectrum, where hydrocarbons such as CH₄ (3.3 μm) exhibit absorption features [32]. Using a spectroscopic model, with knowledge of the plume composition and ambient temperatures, the column densities along the line of sight of the QOGI camera are inferred from the intensity of the radiation measured (i.e., the brightness of a pixel in a QOGI image). The output of this is a 2-D map of column densities that can then be used to infer an emission rate using an advection model that is usually identified by analyzing the motion of the plume across successive QOGI images [30, 31].

The specific QOGI cameras evaluated during the field measurement campaigns included a FLIR GFx320 camera with a QL320 tablet operated by a researcher from the University of Waterloo (UW) [33], a second FLIR GFx320 system operated by AGAT technologies, as well as an OPGAL EyeCGas camera with an EyeCSite tablet that was operated by personnel from Montrose Environmental Ltd [34, 35]. Both cameras have similar technical specifications in terms of the spectral range of detection, resolution, optics, and sensitivity. The tablets for each camera use proprietary algorithms to infer column densities and the advection model to then output an emission rate estimate. Technical specifications for each QOGI technology can be found in Appendix B.

1.3.3 Aerial Hyperspectral Measurements

Hyperspectral measurements of methane are performed by generating thousands of images of the same scene, each corresponding to different wavelength measurements (known as a “hypercube”). through the use of an imaging Fourier transform spectrometer (IFTS) that maps the intensity of each pixel across a range of wavelengths [36] [37]. Like QOGI, the output of these measurements is a 2-D column intensity map, which is then related to an emission rate using an advection model.

The hyperspectral techniques evaluated during the field measurements are both examples of aerial hyperspectral measurements, where downward facing hyperspectral cameras are mounted to an aircraft that flies overhead a facility/site where measurements are taking place. One of these cameras was the IFTS package from GHGSat, operating in the near infrared (NIR) spectrum (1630nm to 1655nm), mounted to an airplane [38]. This system relies on reflected sunlight off the ground, that is attenuated by the gas layer as it reflects back up to the measurement location. The other system was the Telops Hyper-Cam xLW Airborne Mini [39], which is another example of a downward facing IFTS package. However, the Telops hyper-cam operates in the long-wavelength infrared (LWIR) spectrum between 7.4 μ m and 12.5 μ m and does not rely on reflected sunlight. Instead, this system relies on a thermal contrast between the ground and the gas being measured in order to properly detect and quantify the emission. The specifications for the LWIR aerial hyperspectral technology can be found in Appendix C.

1.3.4 Truck-based TDLAS Measurements

TDLAS measurements work by scanning a precisely tuned laser, emitted from a diode, back and forth across the absorption line for a target gas at a known emitted intensity [40]. The emitted light is directed through a gas sample, before reaching a detector that measures the intensity of the light after having passed through the gas sample [40, 41]. While the light passes through the gas sample

at the specific absorption line, the light intensity will decrease as a portion of the emitted radiation is absorbed by the gas; the difference between the emitted light intensity and the detected light intensity is related to the concentration of the gas within the sample by the Beer-Lambert law.

$$A = \log\left(\frac{I_0}{I}\right) = \varepsilon_{abs} l c_M \quad (1-1)$$

where A is the absorbance; I_0 and I are the intensities of the light emitted by the diode and the light detected after passing through the gas, respectively; ε_{abs} is the molar absorption coefficient for the specific gas; l is the path length; and c_M is the molar concentration [41, 42]. The molar concentrations can then be converted to a parts per million (ppm) concentration, or another useful unit of concentration depending on the application. The concentration data can be combined with an advection model to infer an emission rate of the source.

The specific truck-based TDLAS technology that is the focus of this thesis is Boreal Laser's Gasfinder3 VB™ [43] system. This system uses an enhanced TDLAS technique known as wavelength modulated spectroscopy (WMS). In WMS, the wavelength of the emitted laser is scanned rapidly and usually sinusoidally centred on the absorption wavelength of interest through the harmonic modulation of the supply current [44]. The absorption information is then detected on the harmonics of the modulation frequency, and post-processed to obtain concentration data [45]. WMS is an enhancement of TDLAS due to improved noise rejection, allowing for lower thresholds of detection [44]. The absorption wavelengths correspond to natural frequencies of vibrational and rotational motion of the molecules, which are governed by the mass of the molecules, and the strength of the molecular bonds (analogous to a spring-mass system) [46, 47]. When radiation of different wavelengths passes through a gas, the molecules absorb radiation at the specific wavelengths that match either the natural vibrational frequencies, or overtones of the natural vibration due to higher vibrational states [46, 48]. Boreal Laser's system is centred on the

1512 nm absorption line for CH₄ in the near infrared. It uses tuning mirrors and a retroreflector, and a photodiode to collect a laser signal, all mounted within a 1.3m wide chamber that is mounted to the back of a truck. The measurement chamber is perforated such that as the truck drives through a methane plume, particles of methane diffuse into the chamber. The path integrated concentrations are reported as ppm concentrations with a frequency of 1 Hz [43]. The reported accuracy of the technology is reported to be less than 2% concentration error, however at near ambient concentrations, the errors have been shown to be larger than this reported value [46]. Even at near ambient concentrations, however, the uncertainties in emission estimates are still expected to be dominated by errors in the advection model used to infer an emission rate. Technical specifications for the Gasfinder3-VB system can be found in Appendix D.

1.4 Uncertainty Quantification

Following the review and characterization of methane quantification technologies, it is important to identify how uncertainty arises in the emission estimates these technologies provide. This section provides an overview of how uncertainty arises from different sources, introduces Bayesian inference as a tool for quantifying uncertainty, and discusses different ways of analyzing uncertainty from a model-based or empirical approach.

1.4.1 Overview of Uncertainty

Understanding uncertainties associated with quantification technologies is essential in ascertaining what the reality of methane emissions is in the context of reported emission rates. This affects both the prioritization of LDAR programs, as well as in ensuring that policies and regulations are enforced with a science-based approach, using the most accurate representation of the data as possible [5]. As an example, uncertainties associated with emissions estimates has been attributed as a cause for discrepancies between top-down, and bottom-up emissions inventories [14] [47, 48,

49]. Johnson et al. showed that using a hybrid methane inventory procedure combining top-down and bottom-up emissions measurements, the actual methane inventory of British Columbia's oil and gas industry was likely 1.7 times higher than the reported values [47]. Using previously identified probability of detection (POD) and uncertainty models for an aerial measurement technology, they combined top-down measurements across British Columbia's oil and gas sector with more traditional bottom-up emissions factors and measurements within a Bayesian and Monte Carlo framework that considered both the probability of missed detections, and the measurement uncertainty for the aerial technology [47, 50]. Through this, they were able to construct a probability density function (PDF) that described the probability distribution for the total CH₄ inventory of the region's oil and gas sector. They found that even at the lowest inferred inventory within a 95% credible interval, the measured inventory was significantly larger than what was being reported as the official inventory. From this, it is clear to see how methane emission quantification uncertainty can impact the proper regulatory and emission reduction strategies.

Uncertainty in emissions estimates arises from three major sources. As seen in Figure 1-3, these are the measurement noise, uncertainty arising from assumption/simplifications used in measurement models, and uncertainties in model parameters.

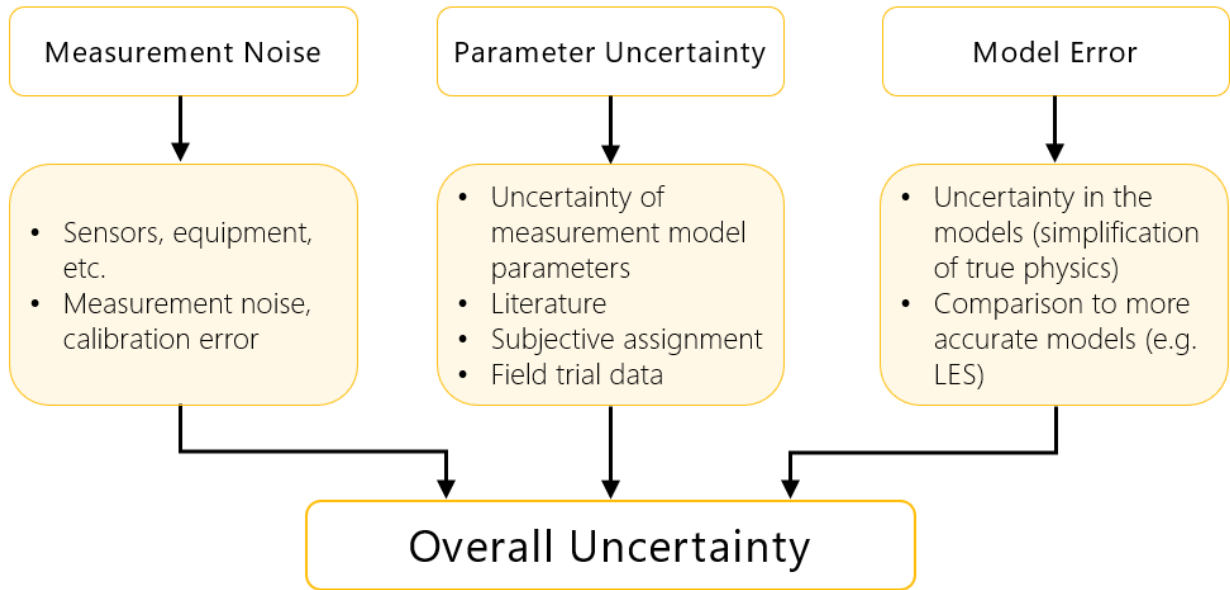


Figure 1-3: Schematic of sources contributing to overall emission estimate uncertainty.

From Figure 1-3, measurement noise refers specifically to errors associated with the methane measurement sensors. An example of this would be uncertainties in parts per million (ppm) point concentration measurements from a tunable diode laser absorption spectroscopy (TDLAS) measurement of methane. Parameter uncertainty is imparted by uncertainties in any parameters used in a measurement model. Typically, methane emissions estimates are a combination of a methane measurement (e.g. concentration), and a measurement model that links the concentration to an emission rate [51]. These measurement models typically include variables relating to the atmospheric conditions and other ancillary parameters (e.g. windspeed, temperature, etc.). Like the measurements of methane, the measurement and/or identification of these parameters comes with associated uncertainty that contributes to the overall uncertainty of the subsequent emission estimate. The final source of uncertainty is the model error. This refers to the uncertainties associated with simplifications and assumptions made by the model, that depart from what is

actually occurring. Generally, the uncertainties arising from model error dominate the overall emission estimate uncertainty.

1.4.2 Introduction to Bayesian Inference for Uncertainty Analysis

One of the main tools used in this thesis for the analysis of uncertainty is Bayesian inference. One of the difficulties in inferring an emission rate from data is the uncertainty introduced by uncertainties in model parameters, Φ , and by errors in the model itself. These uncertainties mean that deterministic emission estimates obtained directly from the measurement model are less robust than methods that factor in these uncertainties. Bayesian inference, however, provides a useful way to deal with these errors.

In Bayesian inference, the quantity of interest, the measurement data, and the nuisance parameters (which are contained within Φ) are all treated as random variables that obey PDFs [52]. These PDFs are related by Bayes' equation. As it relates to methane emissions quantification, Bayes equation is

$$p(q, \Phi | \mathbf{c}) = \frac{p(\mathbf{c} | q, \Phi) p_{\text{pr}}(q) p_{\text{pr}}(\Phi)}{p(\mathbf{c})} \quad (1-2)$$

where $p(q, \Phi | \mathbf{c})$ is the posterior PDF defining the probability of a given release rate and set of model parameters conditional on the measurements \mathbf{c} and prior information, and is a statement on what is known about q and Φ after the measurements have been performed; $p(\mathbf{c} | q, \Phi)$ is the likelihood of observing the measurements for a given release rate and set of model parameters, $p_{\text{pr}}(q)$ and $p_{\text{pr}}(\Phi)$ are known as “priors” and are PDFs that describe what is known about each respective parameter before the measurement take place; and $p(\mathbf{c})$ is the evidence, which normalizes the right hand side of Eq. (1-2) to ensure the Law of Total Probability is satisfied.

1.4.3 Empirical Uncertainty Analysis

Uncertainty can be modeled in one of two ways. If the measurement model is complex, unavailable, or unknown (i.e., a “black box”), empirical uncertainty models build upon controlled release measurements can be used to describe the uncertainty of a particular technology using real field data [51]. For example, Conrad et al. used controlled release data to quantify the probabilities of detection, and emission estimate uncertainties associated with three separate airborne methane quantification technologies [50]. Using controlled release data for each technology, they evaluated different probability of detection (POD) functions using a binary regression, modelling the successful or unsuccessful detection of a release as a Bernoulli distribution of the POD function. Furthermore, they used the controlled release data for each technology to model the uncertainty of emissions estimates as a function of the true emission rate, based on the observed bias and precision of the technologies’ controlled-release data.

Wigle et al. investigated the characterization of methane emission quantification uncertainty using controlled release data for a truck-based TDLAS technology, an aerial TDLAS technology, an aerial hyperspectral technology, and two QOGI technologies [51]. Their work builds upon Conrad et al. [50], however the modelling performed by Wigle et al. is more flexible in the way the relationship between the true emission rate and the emission estimate is modelled. Furthermore, the estimation of model parameters is done through Bayesian inference, rather than the frequentist approach taken by Conrad et al. Through their analysis, Wigle et al. identify different likelihood functions for each technology, and use these likelihoods to model the uncertainty of these technologies through the construction of predicted credibility intervals (CIs) based on the emission estimate. Finally, they demonstrate how these results can be applied to quantify the uncertainty of new measurements, using a QOGI measurement as an example. Note that some of the data used

by Wigle et al. is the same data used for the analysis performed in this thesis, and the specific technologies investigated (with the exception of the aerial TDLAS technology), as well as the design and execution of the controlled release measurements are expanded upon in Chapter 2 of this thesis.

1.4.4 Model-based Uncertainty Analysis

When the measurement model used by a technology is simple, well-defined, and invertible, it is possible to take a “model-based” approach to emission estimate uncertainty, by propagating the uncertainty through the measurement model [51]. Model-based approaches have been used for a variety of technologies, such as Montazeri et al., who investigated the uncertainties associated with a QOGI method of methane quantification [53]. Specifically, they used a CFD phantom of a turbulent methane jet to investigate the performance of emissions estimates that combined column densities with a derived 2D velocity field from image feature-tracking. Through this analysis, they show how the uncertainties associated with emission estimates derived from this technique can be exacerbated by factors such as small data acquisition times, and by measurements very close to the source (<10m distance) [53].

Caulton et al. investigated how uncertainties in model parameters of the GPM model propagate through the model to the overall emission estimate uncertainty for truck-based measurements of well pads from a LiCOR 7700 methane sensor [23, 54]. For a number of model parameters, they investigate the uncertainty analytically by investigating through the well-defined GPM how emission estimates changed with uncertainties in source location, wind speed, background methane concentration, and source height. The uncertainties in the model parameters were in some cases defined by data collected during controlled release measurements (such as the average variance of the wind speed), or in other cases determined heuristically, such as in assumptions

relating to how much error would be expected in the atmospheric dispersion parameters used by the GPM to approximate the turbulent plume dispersion. They also examined the error associated with the GPM itself, by comparing emissions estimates obtained from well pads to CFD simulations of similar emission characteristics. Large eddy simulations (LES) were performed for a number of sites where a large number (>10) of transects were performed. The emissions derived from the truck-based measurements using the GPM were then compared to the LES data, and the uncertainty arising from the model was defined as the average discrepancy between LES and GPM-derived emissions estimates. Finally, they performed a Monte Carlo analysis, where the expected uncertainties in model parameters were defined, and combined with the expected uncertainties in the emission estimate resulting from the errors in each model parameter. From this analysis, the uncertainties associated with different GPM approaches are expressed as 95% credible intervals, that are a function of the true emission rate, q , ranging from $0.05q$ to $6.5q$ (i.e. between 5% and 650% of q) [23].

Finally, Zhou et al. examined truck-based methane emissions uncertainty using a Bayesian statistical analysis [55]. First, they describe the overall emission uncertainty as a combination of stochastic uncertainty, errors in the dispersion model, and data errors associated with the dispersion model's parameters.

$$\sigma_e^2 = \sigma_s^2 + \sigma_m^2 + \sigma_D^2 \quad (1-3)$$

where σ_e^2 is the total uncertainty; and σ_s^2 , σ_m^2 , and σ_D^2 represent the stochastic uncertainty, model uncertainty, and data error uncertainty, respectively [55]. They define the stochastic uncertainty as the variance of the measured cross-plume integrated concentrations; the model error is assigned via a literature review of performance evaluations of the dispersion model used (in this case, the

GPM); and the data errors are further parametrized by the different sources of data error, before being assigned by further literature review of these model parameter errors.

They combine these sources of error into an overall “uncertainty” term to describe the total uncertainty of emissions estimates. This uncertainty is the basis for a Gaussian likelihood function they use in their Bayesian analysis. Through their Bayesian analysis, they are able to numerically solve Bayes’ equation for a range of discretized emission rates. Emission estimates are obtained from the mode of the resulting posterior PDF, while their uncertainty is defined by the width of the posterior PDF. Zhou et al. also then investigated different likelihoods to be used within the Bayesian analysis – specifically the Gaussian likelihood function – and a log-normal likelihood function using vehicle-based concentration measurements of controlled releases [1]. Transects were performed between 10 m and 30 m downwind of the source location, with a Picarro G2204 cavity ring-down spectrometer [56], and a LiCOR 7700 methane analyzer [54]. Releases were performed both with and without obstacles to the downwind dispersion of the plume. Emissions estimates in this work involved repeated transects of the same emission. With repeated measurements, emissions estimates were refined through a process known as Bayesian updating. With this procedure, the posterior PDF from one transect becomes the prior for the next transect; the effects of the initial prior on the emission estimate becomes less important, and the statistical properties of the final posterior PDF begin to converge [57]. Through this analysis, they found that the log-normal likelihood function performed better than the Gaussian likelihood function when no obstacles were present, while the Gaussian likelihood function performed better than the log-normal likelihood function when obstacles were present [1]. The analysis presented by Zhou et al. points to an important phenomenon known as plume meandering. This phenomenon is elaborated on in Chapter 3, as well as its implications on quantification uncertainty.

1.5 Research Objectives

While there has been some investigation into uncertainties associated with methane quantification, this work has been far outpaced by the development of new technologies that are subject to uncertainties that need to be addressed. This thesis presents a generic Bayesian procedure for quantifying uncertainties in methane emissions estimates using a truck-based TDLAS technology as an example application for the procedure. The primary objectives of the thesis are to:

1. Within a Bayesian statistical framework, quantify the uncertainties associated with emissions estimates from truck-based TDLAS concentration measurements combined with a Gaussian Plume Model (GPM).
2. Understand the model error associated with the Gaussian Plume Model using high-fidelity computational fluid dynamics (CFD) analysis.
3. Investigate and explain factors affecting the uncertainties of emissions estimates, including atmospheric, release, and measurement factors.
4. Develop a procedure that can be applied to a variety of measurement techniques and technologies.
5. Identify limitations with the analysis/research performed for this thesis, and what future work can be performed to build on this work.

1.6 Overview of Thesis

This section provides a high-level summary of the following chapters of this thesis.

Chapter 2 outlines the controlled-release measurements that were used to gather data for the analysis described in later chapters of this thesis. This chapter outlines the specific measurements that took place, where and when measurements were performed, and the high-level empirical results for each technology present at the field measurement campaigns.

Chapter 3 discusses vehicle-based methane quantification, which is the focus of the analysis of this thesis. It briefly provides an overview of how vehicle-based methane quantification is performed, and then a detailed derivation of the Gaussian plume model. This chapter identifies the assumptions that the model makes that can lead to error and uncertainty in emissions estimates. It concludes with a discussion on how the uncertainty for truck-based measurements can be modelled.

Chapter 4 details the Bayesian inference procedure performed to infer emission rate estimates, with associated uncertainty, from the data obtained during the controlled release measurements. The form of the likelihood is presented, with a comparison to the likelihood function derived by Zhou et al. The chapter continues with a description of the treatment of priors in the Bayesian inference procedure and how the resulting posterior PDF can be used to obtain emissions estimates with uncertainty quantification.

Chapter 5 describes the CFD simulations that were performed to investigate the model error associated with the GPM. First, it outlines the initial, simplified simulations that were performed, and the issues that arose from them. Then, it details the high-fidelity detached-eddy simulations that were performed and describes how those simulations were used to investigate the GPM model error.

Chapter 6 provides the results of the Bayesian inference. It describes how investigations into uncertainty are performed and provides sample results of the posterior distributions for the emission rates. The chapter continues with an investigation into what factors affect the uncertainty of emission estimates, including the wind characteristics and measurement distance.

Chapter 7 concludes the thesis with some discussion of the key findings, as well as identifying some limitations for the study and recommendations for future research.

2 Controlled-release Experiments

To investigate the uncertainties associated with the selected quantification technologies, a series of controlled release measurement campaigns were conducted in April 2022 and September 2022 near Brooks, Alberta. The purpose of these measurements was to gather data for the development of an empirical-based uncertainty analysis for the participating technologies, as well as a more generalized model-based approach to uncertainty, which is the focus of this thesis. This chapter provides the location, schedule, and setup of the controlled releases, as well as the details of the specific measurements performed by each technology. Finally, this chapter outlines the relevant meteorological data gathered, and the importance of this data for the following analysis.

2.1 Overview of field measurement campaign

The field measurement campaigns were performed at Carbon Management Canada's field research station (FRS) in Newell County, Alberta [58] southwest of the town of Brooks. Measurements from the first campaign were conducted from April 20 to April 24, 2022, while the second set of measurements were performed from September 25 to October 1, 2022. The location of the site can be seen in Figure 2-1. To help perform controlled release measurements, the FRS is equipped with a variety of equipment to facilitate releases, including a flare stack, a modular vent stack, storage tanks, and a storage shed. The operations of the field measurements are coordinated from an ATCO trailer, where a Davis WeatherLink Pro + weather station is used for monitoring relevant meteorological parameters such as wind speed, wind direction, and temperature [59].

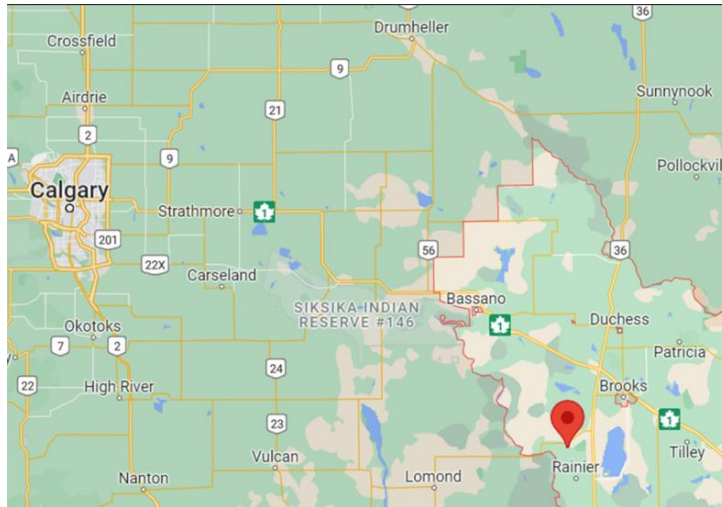


Figure 2-1 Location of CMC's field research station in Newell County, Alberta

Releases were performed from pressurized methane tanks stored in a trailer. The composition of the gas was determined through gas chromatography of five samples of the gas. The results of this are summarized in Table 2-1.

Table 2-1: Gas composition for controlled release measurements

Component	Volumetric Percentage
Methane (CH ₄)	94.2%
Ethane	3.4%
Propane	1.1%
Other components (mostly N ₂ and O ₂)	1.3%

The release apparatus can be seen in Figure 2-2. Gas, as described in Table 2-1, was released from tanks via a regulator, before flowing through a heat exchanger. The heat exchanger is necessary to raise the gas temperature to near ambient conditions, as the Joule-Thomson effect causes the gas to cool as it is initially released from the pressurized tanks. The gas then flows

through an Alicat Model MCR-2000SLPM-D-PAR mass flow controller [60], which controls the release rate of gas to the environment. A thermocouple was used near the release location to confirm that the temperature of the released methane was near ambient conditions.



Figure 2-2: Setup of methane releases

The releases were performed in a “semi-blind” manner, in that the technology operators were aware that the release was taking place and where the release was, but they were not aware of the true emission rate. The releases relevant to the truck-based TDLAS technology ranged from 0.25 kg/h to 80 kg/h, as well as a number of “null” releases where the release rate was 0 kg/h.

Releases were performed from a 13m tall flare stack, a modular vent stack (Figure 2-3) varied between 1.7m, 3.4m, and 4.8m heights, a storage tank (Figure 2-4), and an equipment storage shed. Figure 2-5 shows an aerial view of the site, with the approximate locations of releases. The full release schedules can be found in Appendix E and Appendix F.



Figure 2-3: Modular stack configured for releases from 1.7m above the ground



Figure 2-4: Releases from a storage tank

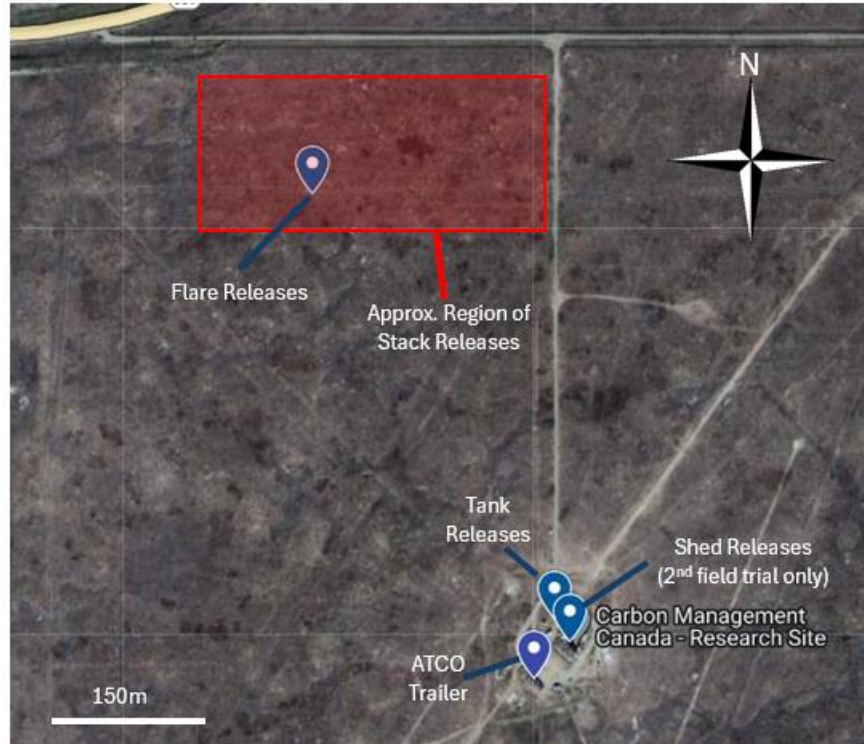


Figure 2-5: Aerial view of the site with approximate release locations.

2.2 Meteorological data

As mentioned previously, emissions estimates are typically obtained by combining concentration measurements with meteorological data within an atmospheric dispersion model. As such, it was necessary to gather accurate meteorological data throughout the releases. For the first measurement campaign in April 2022, meteorological data was primarily obtained through the Davis Weatherlink Pro + weather station equipped at the field research station. For the second measurement campaign, meteorological data was gathered from both the weather station, and a portable 81000L RM Young UVW 3D ultrasonic anemometer [61]. Of particular importance was collecting accurate wind (speed and direction) and temperature data across all measurement times. Figure 2-6 shows representative wind and temperature data from the first measurement campaign, while Figure 2-7 and Figure 2-8 show the wind and temperature respectively, for a representative

day from the second measurement campaign. Importantly, for the second set of data there was good agreement between the two sources of meteorological data. For the purposes of analysis for the second measurement campaign, only the portable ultrasonic anemometer was used.

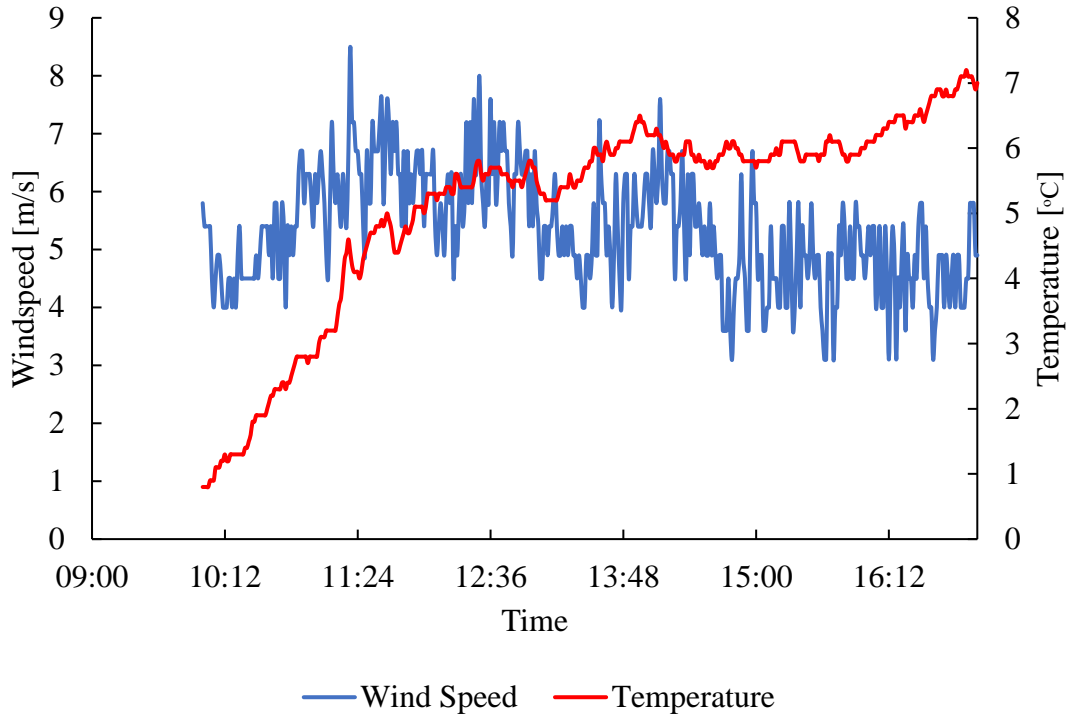


Figure 2-6: Wind speed and temperature data from April 21, 2022.

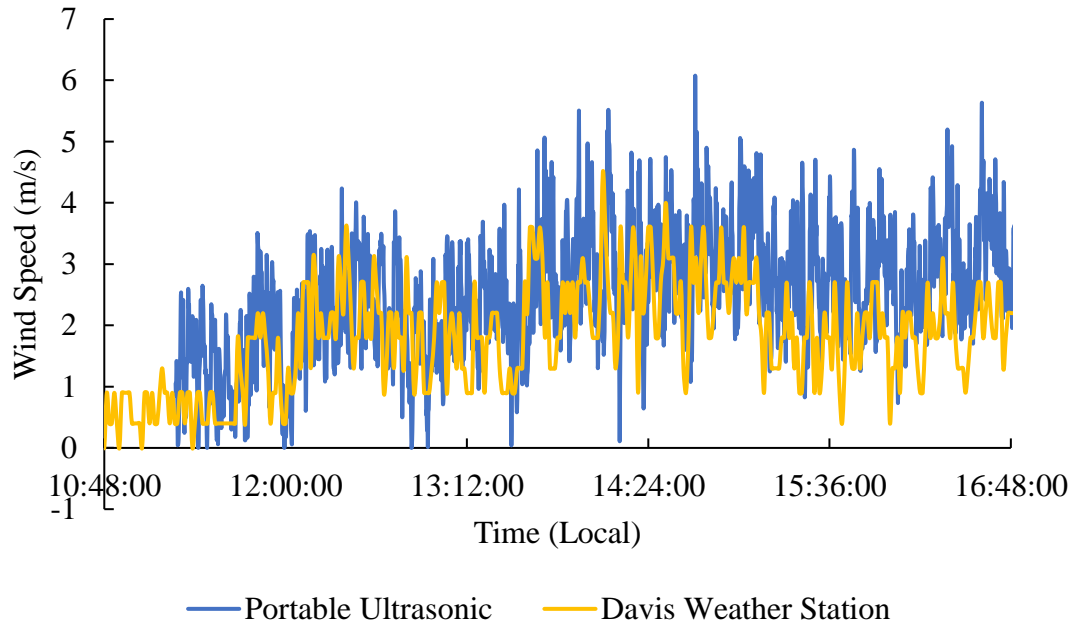


Figure 2-7: Wind speed data from September 26, 2022

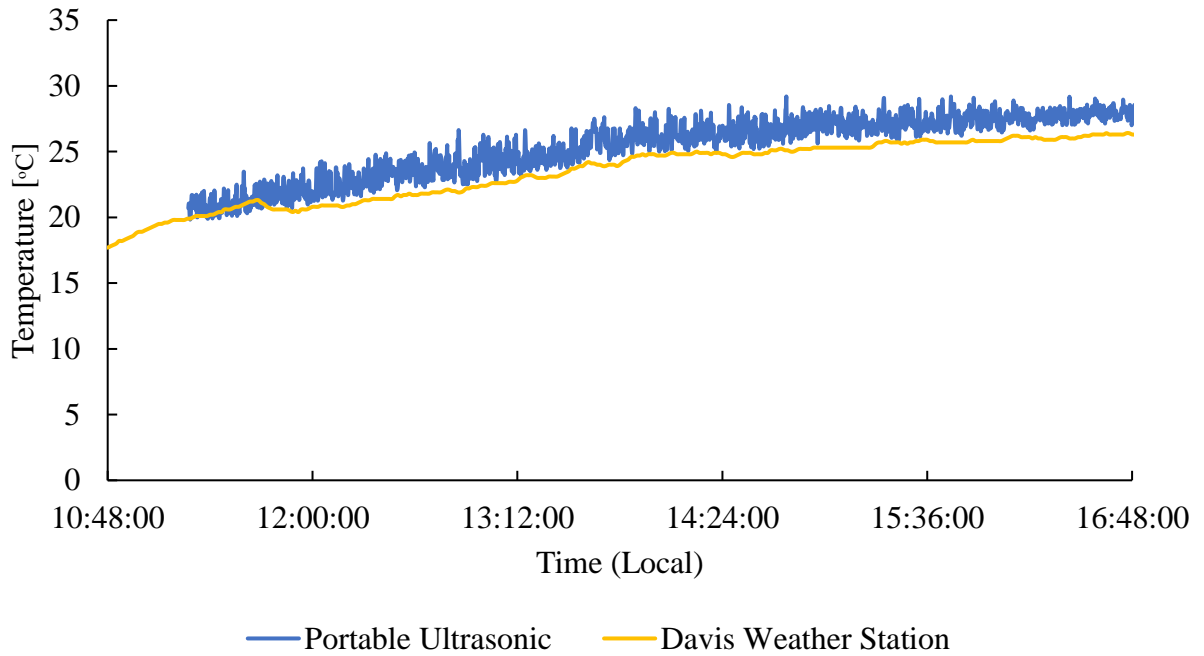


Figure 2-8: Ambient temperature data from September 26, 2022

In an effort to avoid any temporal correlations in the data, during the second field measurement campaign, the release rate was randomized throughout the day, to try and obtain a variety of meteorological conditions corresponding to each emission rate. An example of this can be seen in Figure 2-9. Furthermore, Figure 2-10 shows the release rates for the entirety of the second measurement campaign compared to the average windspeeds during the release windows, while Figure 2-11 shows the same for temperature. The spread of data seen in Figure 2-10 and Figure 2-11 show that every release rate performed corresponded to a representative sample of meteorological conditions.

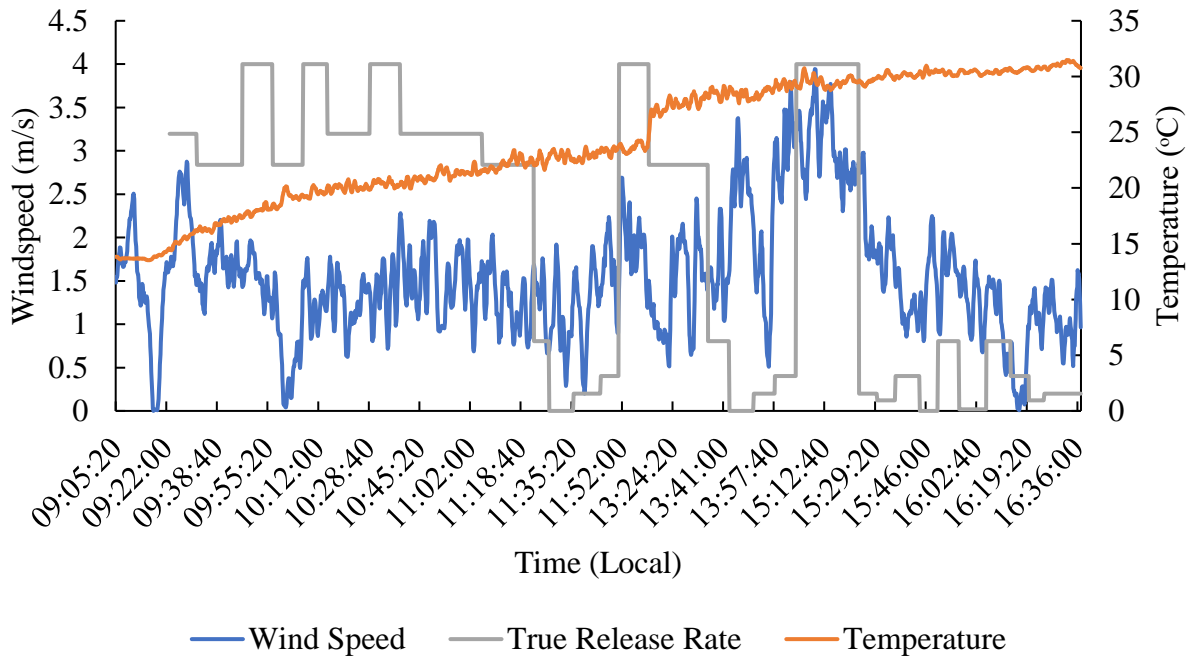


Figure 2-9: Modulation of release rate (normalized to the scale of the graph) compared to wind and temperature measurements for September 28th, 2022

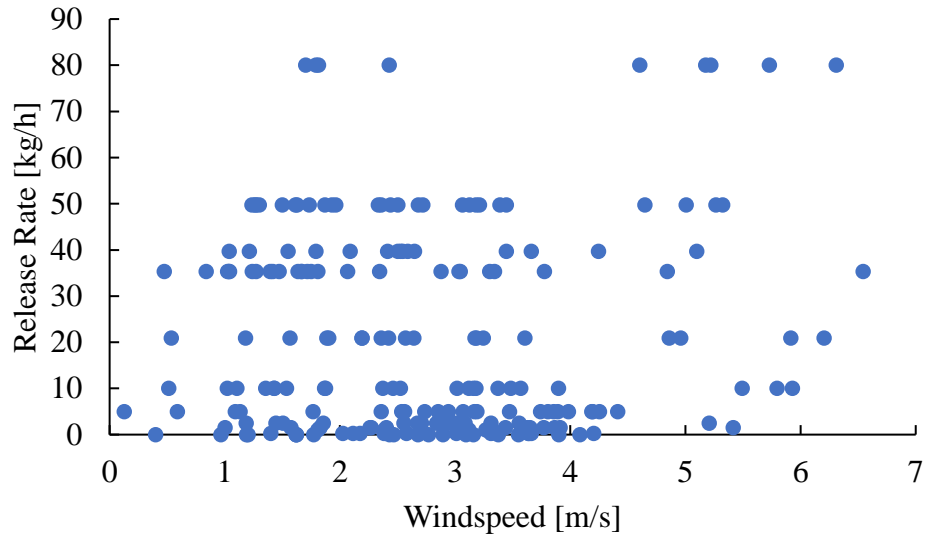


Figure 2-10: Release rates vs windspeed for the September 2022 measurements

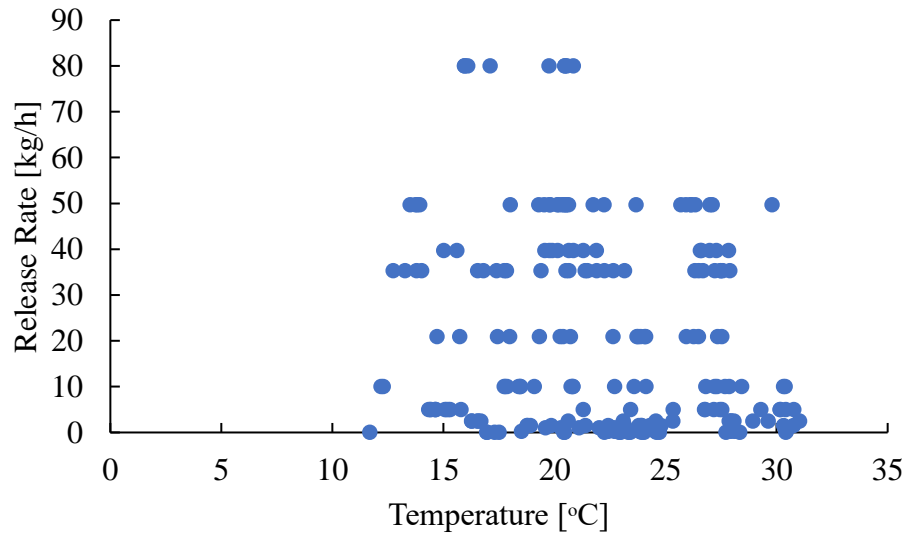


Figure 2-11: Release rates vs temperature for the September 2022 measurements

2.3 Empirical Results of the Field Measurement Campaign

2.3.1 QOGI Measurements

At the first field measurement campaign, the UW and AGAT operated FLIR GFx320 systems were tested. For the second set of measurements, the OPGAL EyeCCGas camera was present along with

the UW operated FLIR GFx320 camera. A summary of the high-level empirical results for each QOGI technology can be found in Figure 2-12 to Figure 2-15.

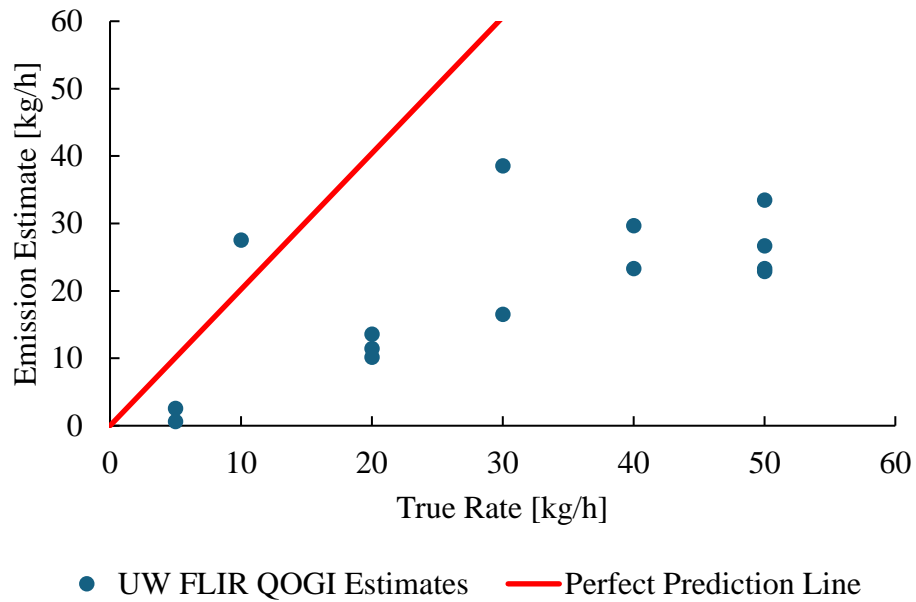


Figure 2-12: Summary of UW operated FLIR emissions estimates for the April 2022 field measurement campaign

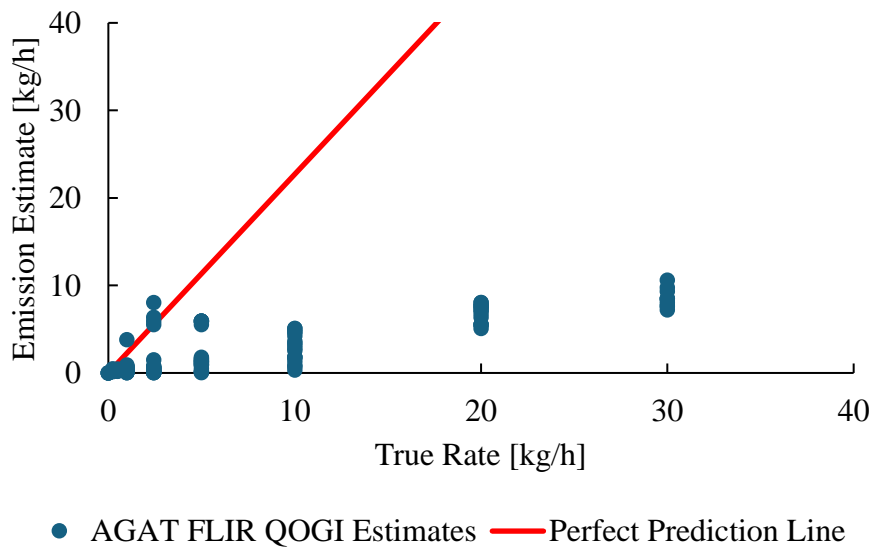


Figure 2-13: Summary of AGAT operated FLIR emissions estimates for the April 2022 field measurement campaign

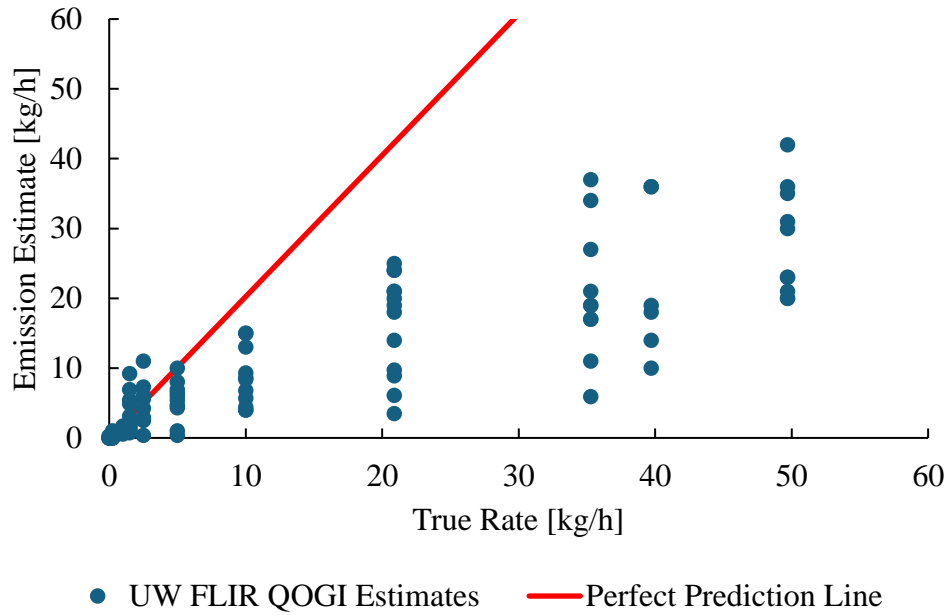


Figure 2-14: Summary of UW operated FLIR emissions estimates for the September 2022 field measurement campaign

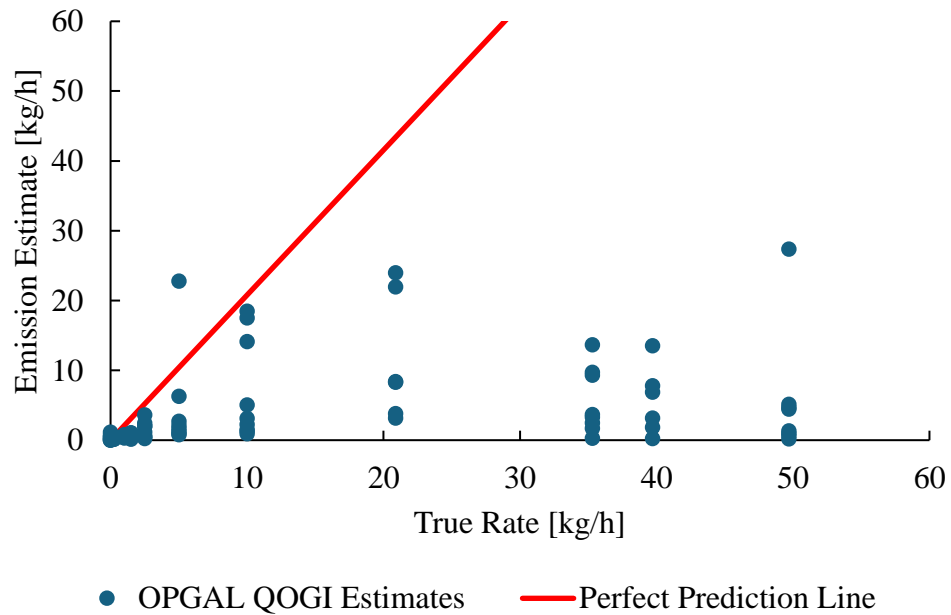


Figure 2-15: Summary of OPGAL emissions estimates for the September 2022 field measurement campaign

From the first field measurements, the UW operated FLIR camera provided more accurate estimates, with an average error of 40%, compared to 67% for the AGAT operated camera. This was attributed to the fact that the UW operator was using a newer version of the QL320 tablet used for quantification. From the second measurements, the UW operated FLIR camera outperformed the OPGAL camera, with an average error of 59% for the FLIR camera, compared to an average error of 68% for the OPGAL camera. The reduced accuracy of the OPGAL system compared to the UW operated camera was attributed to challenges that arose due to the operator's unfamiliarity with the OPGAL system at the time of the field trial. Some of the key factors that were found to influence the accuracy of the QOGI quantification methods included the distance between the source and the camera (which was a factor for the different equipment from which releases took place), the temperature difference between the methane plume and the background, and "pooling" of the methane at very low wind speeds.

2.3.2 Aerial NIR and LWIR Hyperspectral Measurements

During the first and second field measurement campaigns, the NIR hyperspectral camera provided by GHGSat was deployed from an aircraft flying approximately 1500m above the ground at an airspeed of 240 km/hr. In contrast to the other quantification technologies that measured releases from all of the different types of emitting equipment, due to the availability of the technology, the NIR hyperspectral camera was only used to measure emissions from the 13m tall flare, and the modular stack at a height of 1.7m. During the first field measurement campaign, technical issues primarily related to dense cloud cover prevented measurements from being taken for most of the releases performed. During the second field measurement campaign conditions fared better, and more data was gathered from the NIR hyperspectral camera. During the second field campaign,

the LWIR hyperspectral camera from Telops was also deployed and took measurements from a helicopter flying at approximately 100 m above the ground at 35 m/s. The empirical results for each aerial hyperspectral technology can be found in Figure 2-16 to Figure 2-18.

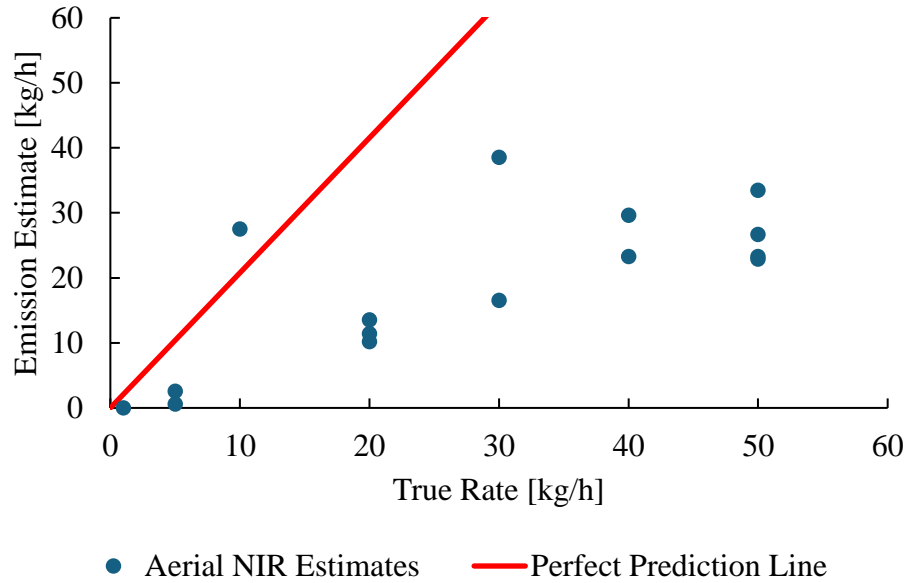


Figure 2-16: Summary of NIR hyperspectral emissions estimates for the April 2022 field measurement campaign

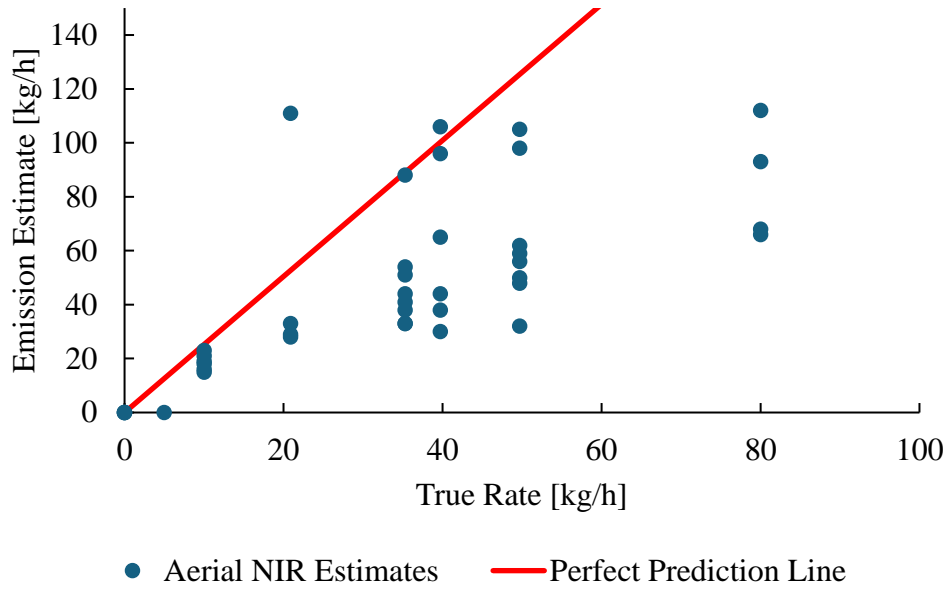


Figure 2-17: Summary of NIR hyperspectral emissions estimates for the September 2022 field measurement campaign.

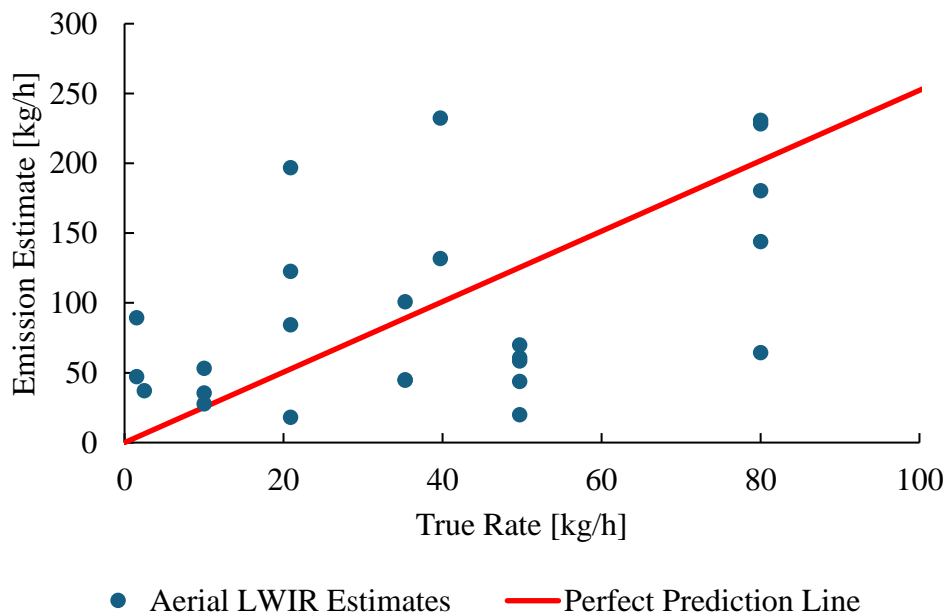


Figure 2-18: Summary of LWIR hyperspectral emissions estimates for the September 2022 field measurement campaign

One important factor for the NIR measurements was cloud cover. As mentioned, this quantification method relies upon sunlight reflected from the ground back to the camera. During the April 2022 measurement campaign, where the cloud density was high, nearly half of the releases were missed by the camera. However, during the September 2022 measurements, the skies were nearly completely clear of cloud during the NIR hyperspectral measurements, and only 2 out of 46 releases were missed by the camera. It is worth mentioning that the measurement conditions the technology was operated under were not normal operating conditions for the technology, and the operator of the technology made a number of comments in their analysis specifically relating to cloud cover. The overall accuracy of the aerial NIR hyperspectral technology was comparable to that of the QOGI cameras, with an average error of approximately 62%.

The LWIR hyperspectral camera was far less accurate compared to the other technologies evaluated during the field measurement campaigns. However, at the time the measurements took place, the LWIR hyperspectral camera was in a far earlier stage of development compared to the other technologies. For example, the method used to generate an emission estimate from a column density map was very rudimentary and resulted in systematic overestimation of the true emission rate. Furthermore, the second field measurement campaign was one of the first deployments of the technology, and there were some issues that resulted from the application of a new technology. Firstly, technical errors relating to the focusing of the camera affected the majority of the measurements. Secondly, some of the collected data was inadvertently deleted by the technology provider. This resulted in meaningful data being recorded for less than half of the measurements, and primarily during times when the thermal contrast between the gas and the background was very low, which further negatively impacted the emission estimates. Following the second field measurement campaign, researchers at the University of Waterloo worked to improve the

quantification method of the technology, and a separate set of field measurements specifically for the LWIR hyperspectral camera took place in September 2023.

2.3.3 Truck-based TDLAS Measurements

During releases at both field measurement campaigns, the Gasfinder3-VB system from Boreal Laser and a GPS sensor were mounted to a truck that performed downwind transects of the plume. These transects were at distances ranging from 20m to 200m downwind from the source, but typically around 100m. For each release, only one or two transects were performed, which results in an instantaneous representation of the methane dispersion in the concentration data. An example of a typical truck measurement path can be found in Figure 2-19.

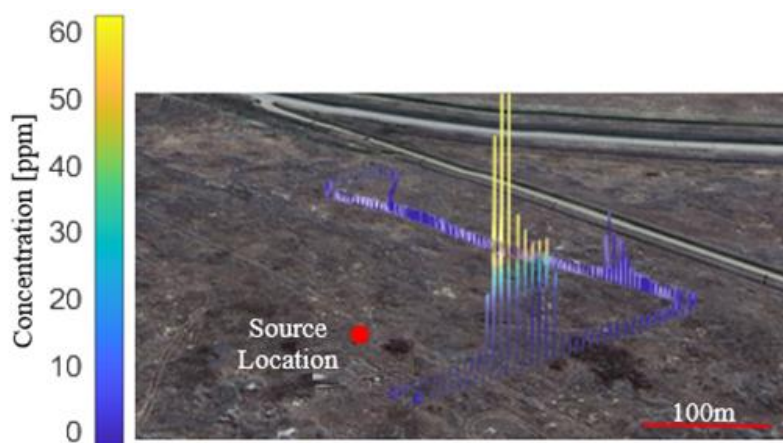


Figure 2-19: Example of path taken by the truck during a release.

Emissions estimates from Boreal Laser were obtained by combining the concentration and GPS data with a backwards Lagrangian stochastic (BLS) dispersion model [29, 62]. The BLS model is a dispersion model that describes the trajectories of particles based on random perturbations in the mean flow field [29]. In the “backward” version of the model, the paths of particles attributed with a certain mass of methane are simulated and tracked. The emission rate of a release location is identified by the mass-flux through the control volume at that particular location [29]. In addition to performing this analysis, the raw concentration data was provided by Boreal Laser to the

University of Waterloo, and emissions estimates were obtained by combining the concentration, GPS, and anemometry data through an inversion of the Gaussian plume model (GPM) that is elaborated on in Chapter 3 of this thesis. The empirical results for the truck-based TDLAS technology for both dispersion models can be seen in Figure 2-20 and Figure 2-21.

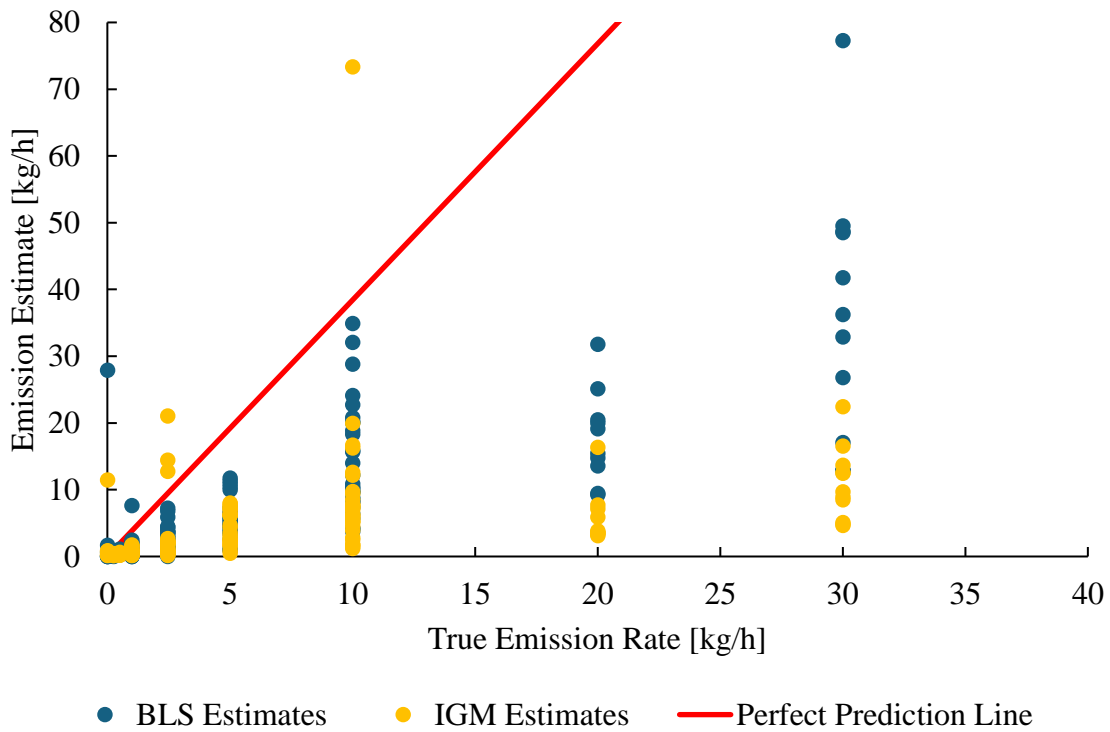


Figure 2-20: Summary of truck-based TDLAS emissions estimates for the April 2022 field measurement campaign using the BLS and IGM analysis

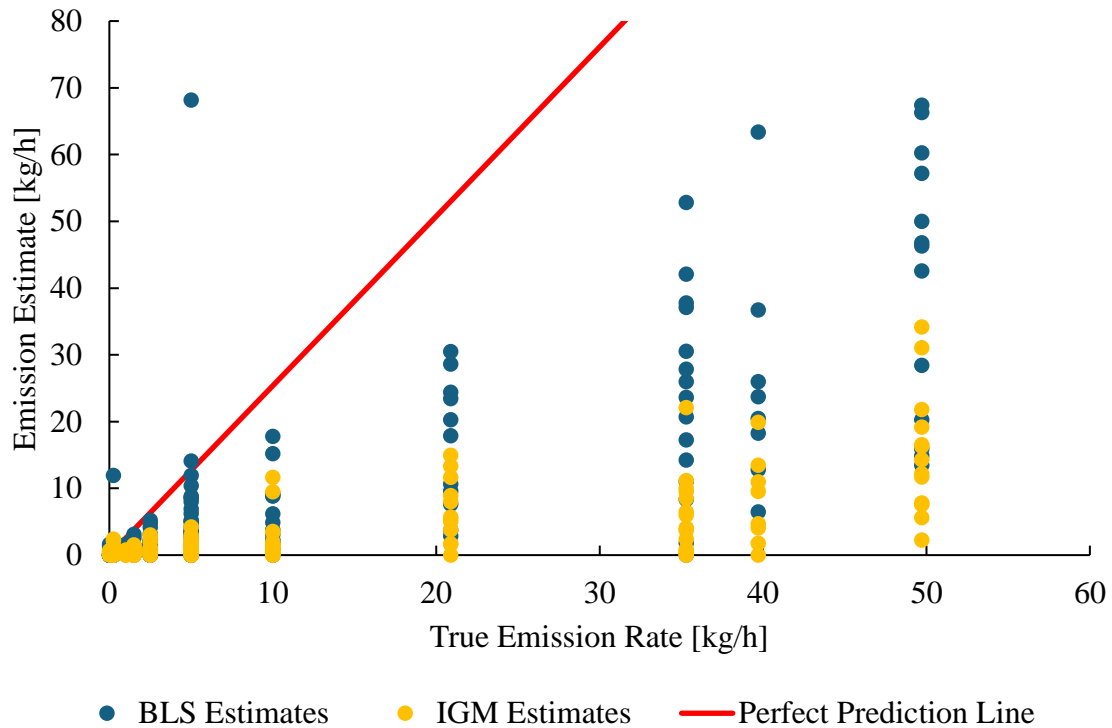


Figure 2-21: Summary of truck-based TDLAS emissions estimates for the April 2022 field measurement campaign using the BLS and IGM analysis

In both field measurement campaigns, the performance of the IGM analysis was similar to the estimates relying on the BLS model; in both sets of results, the average error associated with the IGM was slightly less than the BLS. However, there was a stronger bias associated with the model, in that the IGM estimates were consistently underestimating the true emission rate, while the estimates from the BLS model were a mix of overestimation and underestimation of the true emission rate. Factors that were identified that could contribute to inaccuracies and errors associated with these estimates included the wind speed, the variability of the wind, and the measurement distance. The investigation of these factors using CFD modelling and a Bayesian inference is the focus of this thesis. Specifically, the focus is on the development and application of a model-based approach to uncertainty for only the truck-based TDLAS measurements using a

Gaussian model for plume dispersion. This is because the GPM used with the TDLAS measurements provides a convenient, simple, and invertible model for which error analysis can be performed. Through this analysis, the goal is to develop a generalized, Bayesian approach to uncertainty analysis that can be applied to a wider range of technologies.

3 Vehicle-based Methane Emissions Quantification

This thesis focuses on the understanding of the emissions uncertainty associated with a truck-based TDLAS technology. This chapter details plume dispersion characteristics that are relevant for methane measurement, with particular emphasis on meandering and relative dispersion. Then, it provides an overview of vehicle-based measurements, and the Gaussian plume model (GPM). The GPM is one of the most commonly used dispersion models with vehicle-based methane quantification, and the model that is the focus of this work. This chapter will review a derivation of the GPM, before concluding with a description of how uncertainties associated with vehicle-based emission estimates are modelled.

3.1 Characteristics of plume dispersion

Understanding plume dispersion is fundamental for predicting how CH_4 disperses from an emission source. By identifying key relevant plume dynamics, insights into how uncertainties arise can be attained by comparing the simplifications of a dispersion model to the true characteristics of the plume. These characteristics are caused and influenced by various environmental and meteorological factors, such as the wind speed and direction, and topography. Of particular interest is the idea that plume dispersion can be broadly described by two distinct regions: a meandering region, and a relative dispersion region [23, 55].

Meandering is caused by wind fluctuations and turbulence [63, 64], and is generally defined as the displacement of the centre of mass of the plume due to turbulent eddies that are larger than the plume diameter [23, 65]. The meandering regime is the downwind range where this phenomenon dominates the plume transport. This is typically very close to the source location, where the plume diameter is smaller, and the turbulent eddies are larger in scale than the plume diameter. The

meandering motion causes the plume to sweep back and forth across the downwind region, leading to significant variability and intermittency in CH₄ concentrations [66, 67].

The other region that characterizes plume transport is the relative dispersion region. Relative dispersion refers to the dispersion of a plume relative to its centre of mass due to diffusion within the plume itself [23, 65]. The diffusion within the plume is caused by small-scale turbulent eddies, that are smaller in size than the plume diameter [68]. Thus, as the plume spreads horizontally and vertically further downwind, the relative dispersion phenomenon dominates the overall plume transport.

The difference between meandering and relative dispersion is very important for understanding uncertainties introduced by dispersion models used to translate concentration and meteorological data into an emission rate estimate. Due to the time averaged nature of some dispersion models, including the GPM, these models only account for dispersion of methane relative to the mean centreline of the plume, rather than instantaneous fluctuations in the centreline of the plume itself [23]. The result of this is that the concentrations predicted by the GPM deviate significantly from instantaneous concentration measurements, particularly in the meandering regime of the plume [66]. This deviation introduces model uncertainty to the subsequent emission rates, that must be accounted for. Supporting this, previous studies have shown that in the near-field regime (close to the source), skewed or log-normal distributions tend to more accurately represent plume dispersion quantities, while in the far-field regime further downwind, gamma or Gaussian distributions more accurately represent plume quantities [23, 1, 69]. Depending on the study, the near-field regime is defined roughly as within 50m of the plume source location, while the far-field regime is defined as greater than 80-100m downwind of the plume source.

3.2 Overview of vehicle-based methane emissions quantification

Vehicle-based methane quantification involves methane sensors mounted to a truck or drone which performs cross-sectional concentration measurements (“plume transects”) downwind of an emitting source [23, 1, 24]. The release rate, q , which is assumed to be time-independent, can be related to spatially resolved concentration measurements via an advection function.

$$\tilde{c}(\mathbf{r}) = \tilde{d}(\mathbf{r})q \quad (3-1)$$

where $\mathbf{r} = [r_x, r_y, r_z]^T$ is the position vector; c is the concentration data; q is the emission rate; and the “ \sim ” denotes a turbulent instantaneous (stochastic) quantity. The position vector, \mathbf{r} , is defined such that the x -direction aligns with the downwind direction, the y -direction aligns perpendicular to the wind (the crosswind direction), and the z -direction describes the height above the ground. $\tilde{d}(\mathbf{r})$ is in theory a solution of the advection-diffusion equation:

$$\frac{\partial \tilde{c}}{\partial t} = -\tilde{\mathbf{u}} \cdot \nabla \tilde{c} + k \nabla^2 \tilde{c} \quad (3-2)$$

where c is the scalar concentration field; k is the diffusion coefficient; t is time; and \mathbf{u} is the vector field of wind velocity [70]. This equation, however, does not have an analytical solution for general turbulent flows, due to the complexities of time-dependent turbulent flow fields and boundary conditions in this application. As such, an approximate solution is found by performing a Reynolds decomposition. Reynolds decomposition is a process of decomposing the quantities in turbulent flow into mean and fluctuating components. For example, the concentration, c , becomes:

$$c = \bar{c} + c' \quad (3-3)$$

where the overbar and ' denote the mean and fluctuating components of the concentration. For the advection-diffusion equation, the Reynolds decomposition results in:

$$\frac{\partial (\bar{c} + c')}{\partial t} = -(\bar{\mathbf{u}} + \mathbf{u}') \cdot \nabla (\bar{c} + c') + k \nabla^2 (\bar{c} + c') \quad (3-4)$$

Expanding and distributing terms in Eq. (3-4) results in:

$$\frac{\partial \bar{c}}{\partial t} + \frac{\partial c'}{\partial t} = -(\bar{\mathbf{u}} \cdot \nabla \bar{c} + \mathbf{u}' \cdot \nabla \bar{c} + \bar{\mathbf{u}} \cdot \nabla c' + \mathbf{u}' \cdot \nabla c') + k \nabla^2 \bar{c} + k \nabla^2 c' \quad (3-5)$$

Further simplification can be made with steady state, incompressible flow assumptions, as well as by taking a time average of Eq. (3-5). With the steady state assumption, $\frac{\partial}{\partial t} = 0$. By time averaging, the fluctuating components of the equation become equal to 0, assuming that the mean turbulent quantities are constant over time. It is important to note, however, that the time-average of the product of two fluctuating components is not necessarily equal to 0. That is to say that the time-average of any ($u'c'$) terms is not necessarily zero and must be accounted for. With these assumptions, Eq. (3-5) becomes

$$0 = -(\bar{\mathbf{u}} \cdot \nabla \bar{c} + \nabla \cdot \overline{\mathbf{u}'c'}) + k \nabla^2 \bar{c} \quad (3-6)$$

In Eq. (3-6), the $\bar{\mathbf{u}} \cdot \nabla \bar{c}$ term represents the mean advection of the concentration due to the mean wind. The $\nabla \cdot \overline{\mathbf{u}'c'}$ term represents the turbulent flux and describes how fluctuations in the turbulent field contribute to the transport of a plume. Finally, the $k \nabla^2 \bar{c}$ term is the turbulent diffusion term. It describes how turbulence contributes to the diffusion of the mean concentration field. Typically, measurement models for vehicle-based methane quantification describe the mean advection of a plume by introducing assumptions, simplifications, and terms to approximate the turbulent flux and diffusion. These assumptions and simplifications introduce model error that needs to be quantified. In the following sections of this chapter, a literature review of how model uncertainty has been investigated in previous work is presented. Then, a brief derivation of the Gaussian plume model used in this work is presented, along with how the model uncertainty is handled and investigated.

3.3 Gaussian Plume Model

The Gaussian plume model (GPM) is a well-known, well-defined dispersion model that describes the mean advection of a plume [23, 28, 71]. Due to its simplicity, it is one of the most frequently used dispersion models for vehicle-based methane quantification and represents a convenient starting point for the development of model-based uncertainty analysis. The GPM approximates Eq. (3-6) by using a series of assumptions and modelling parameters to simplify Eq. (3-6). Firstly, the GPM assumes a constant wind speed, u , aligned in the x-direction (downwind direction). It further assumes that turbulent diffusion dominates the domain, however in the downwind direction, the transport is dominated primarily by u and that \bar{c} varies very little in the downwind direction [28, 71]. With these assumptions, the simplified equation becomes

$$u \frac{\partial c}{\partial x} = k \left(\frac{\partial^2 c}{\partial y^2} + \frac{\partial^2 c}{\partial z^2} \right) \quad (3-7)$$

A boundary condition is then applied, equating the mass flow at a downwind plane to be equal to the initial source rate, q .

$$q = \iint u c dy dz \quad (3-8)$$

where the y and z directions are defined as the crosswind and vertical directions respectively. This boundary condition is shown schematically in Figure 3-1.

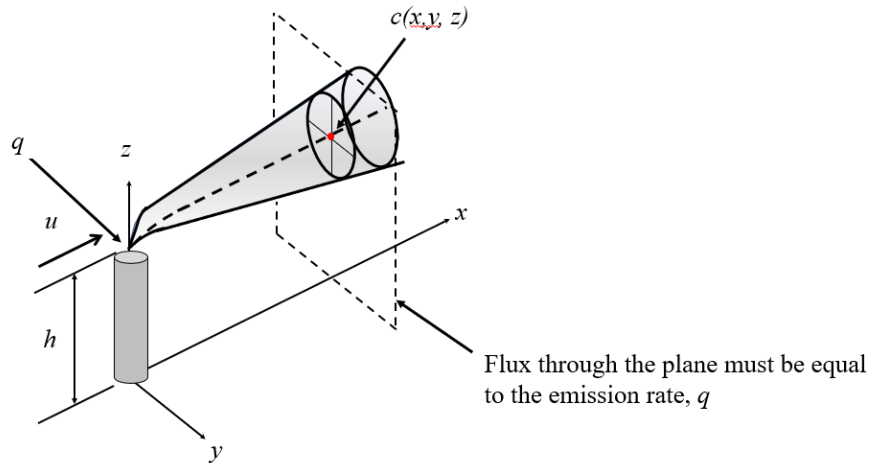


Figure 3-1: Diagram of GPM boundary condition for flux through a downwind plane.

The diffusion of the plume is then modelled using empirically defined dispersion parameters, σ_y and σ_z , which describe the spread of the plume in the crosswind and vertical directions, respectively, with units of meters. These dispersion parameters are often defined by the downwind distance, and the Pasquill stability class [72]. The stability class ranges from classes A to F; a stability class of A represents the most unstable atmospheric conditions, and consequently larger plume spread, while the opposite is true of the most stable stability class, F. There are different ways of determining the stability class for a given flow, however a convenient method due to the simplicity in data collection, is to determine the stability class based on the wind speed, and the solar irradiation [72]. The solar irradiation, or “insolation” of the ground is important, as the heating of the ground can create strong, upward-moving currents of heated air from the ground, leading to a more well-mixed and unstable atmosphere [73]. Table 3-1 shows how the stability class is determined using this method.

Table 3-1: Determination of stability class from wind speed and solar radiation [72] [74] [75]

Windspeed	Daytime Solar Insolation (W/m ²)			Nighttime Insolation	
	Strong (>600)	Moderate (300-600)	Slight (<300)	Cloudy	Clear
< 2 m/s	A	A-B	B	E	F
2-3 m/s	A-B	B	C	E	F
3-5 m/s	B	B-C	C	D	E
5-6 m/s	C	C-D	D	D	D
> 6 m/s	C	D	D	D	D

The solar insolation is approximated by time of year, time of day, and cloud cover. For example, clear skies at midday during the summer would correspond to “strong” insolation. For the data used in this thesis, the insolation corresponded to either moderate, or slight insolation, depending on heuristic observations of the cloud cover. The parameters, σ_y and σ_z , are then determined using

$$\sigma_y = ax^b \quad (3-9)$$

$$\sigma_z = cx^d + f \quad (3-10)$$

where a , b , c , d , and f are all constants that are functions of the stability class and the downwind distance.

With the dispersion parameters defined, and the boundary condition in Eq. (3-8), the solution of the GPM is an analytically tractable differential equation for the mean concentration field:

$$\begin{aligned}\bar{c}(q, \mathbf{r}, \Phi) &= \frac{q}{2\pi u \sigma_y \sigma_z} \left[\exp\left(-\frac{r_y^2}{2\sigma_y^2}\right) \right] \left\{ \exp\left[-\frac{(r_z - h)^2}{2\sigma_z^2}\right] + \exp\left[-\frac{(r_z + h)^2}{2\sigma_z^2}\right] \right\} \\ &= d^{\text{GPM}}(\mathbf{r}, \Phi) q\end{aligned}\quad (3-11)$$

where h is the height of the source; and $\Phi = [u, \sigma_y, \sigma_z]^T$ is a vector of ancillary parameters. The term containing r_y and σ_y accounts for the dispersion of the plume in the crosswind direction, while the terms containing r_z and σ_z account for the dispersion of the plume vertically. The reason for the second vertical dispersion term is to account for the reflection of the plume from the ground back to the measurement height. For the IGM analysis described in Chapter 2, this model was inverted to solve for q given the concentration and positional data from the TDLAS measurements, and the anemometry data needed for the wind speed and determination of the plume dispersion parameters.

As with any model, the assumptions and simplifications used in the derivation of the GPM lead to model error that causes uncertainty in emissions estimates. For example, the GPM approximates the mean concentration field, rather than the instantaneous concentration field, which is what is actually measured when performing plume transects, particularly when in the meandering regime of the plume. The assumption of constant wind velocity and direction also contributes to this model uncertainty. In addition, the dispersion parameters, σ_y and σ_z do not perfectly describe the diffusion of the plume, and as will be seen in the following chapters of this thesis, contribute to significant model error. In identifying the many ways that the model error associated with the GPM contributes to overall emission estimate uncertainty, it becomes necessary to investigate and define the model error.

3.4 Uncertainty Analysis and Model Error

The downwind concentration predicted by the GPM is related to the true concentration field with a model error term:

$$\tilde{c}(\mathbf{r}) = \bar{c}(q, \mathbf{r}, \Phi) + \delta c^{\text{model}}(q, \mathbf{r}, \Phi) = d^{\text{GPM}}(\mathbf{r}, \Phi)q + \delta c^{\text{model}}(q, \mathbf{r}, \Phi) \quad (3-12)$$

where $\delta c^{\text{model}}(q, \mathbf{r}, \Phi)$ is the error term. Due to the turbulent fluctuations within the flow field, and the fact that the errors arising from assumptions made in the derivation of the GPM are unknowable, the model error is a random variable, and is assumed to obey a normal, unbiased distribution. When dealing with concentrations that are measured (e.g. from a truck-based sensor), it is necessary to introduce a measurement error term

$$c^{\text{meas}}(\mathbf{r}) = \bar{c}(q, \mathbf{r}, \Phi) + \delta c^{\text{model}}(q, \mathbf{r}, \Phi) + \delta c^{\text{meas}} \quad (3-13)$$

The δc^{meas} term accounts for the measurement error described in Figure 1-3. However, the measurement error is expected to be much lower than the model error and is therefore excluded from the following analysis. By substituting Eq. (3-1) into Eq. (3-13), and rearranging, the model error term can be described as

$$\begin{aligned} \delta c^{\text{model}}(q, \mathbf{r}, \Phi) &= \tilde{c}(\mathbf{r}) - \bar{c}(q, \mathbf{r}, \Phi) = \left[\tilde{d}(\mathbf{r}) - d^{\text{GPM}}(\mathbf{r}, \Phi) \right] q \\ &= \left[1 - \frac{d^{\text{GPM}}(\mathbf{r}, \Phi)}{\tilde{d}(\mathbf{r})} \right] \tilde{c}(\mathbf{r}) = \tilde{\varepsilon}(\mathbf{r}, \Phi) \tilde{c}(\mathbf{r}) \end{aligned} \quad (3-14)$$

where the error term, $\tilde{\varepsilon}(\mathbf{r}, \Phi)$ is dimensionless and stochastic. Following the work performed by Caulton et al., this error term is investigated using a high-fidelity computational fluid dynamics (CFD) simulation that is described in a following chapter in this thesis.

4 Emission Rate Inference

This chapter provides an overview of how the emission rate, with associated uncertainty is inferred from the data collected during the field measurement campaigns. For this inference, a Bayesian framework is employed, as it is a particularly useful tool when dealing with the stochastic errors associated with methane emissions estimates. This chapter continues from the discussion of Bayesian inference in Section 1.4 and outlines the specific likelihood function used in this analysis. The chapter continues with a discussion of the treatment of priors within the analysis, as well as how emissions estimates and uncertainty can be quantified from the resulting posterior PDF.

4.1 Likelihood Function

The likelihood PDF represents the probability of observing the data gathered given an emission rate estimate and model parameters. The likelihood function describes all the information given by concentration measurements about the emission rate. The likelihood PDF used in this analysis builds upon the Gaussian likelihood function presented by Zhou et al. [1, 55]:

$$p(c_y|q) = \frac{1}{\sigma_c \sqrt{2\pi}} \exp\left(-\frac{1}{2} \left(\frac{c_y - c_y^M(q)}{\sigma_c}\right)^2\right) \quad (4-1)$$

where c_y^{meas} is the transect-integrated measured concentration; c_y^m is the transect-integrated modelled concentration for a candidate q^{est} ; and σ_c is an uncertainty scale parameter consisting of measurement, model, and stochastic error [1]. This likelihood function follows Keats et al., who derived an initial Gaussian likelihood function for describing both the model error and measurement error with separate uncertainty terms for each variable [76].

For this thesis, the concentration data and the model error are treated differently. Rather than forming a likelihood function with the transect integrated or averaged concentration, this thesis

treats each point concentration measurement independently. The concentrations in a transect are described as $\mathbf{c} = [c_1^{\text{meas}}, c_2^{\text{meas}} \dots c_j^{\text{meas}}]^T$, where j denotes a specific point along a measurement transect. With concentration data reported at a frequency of 1 Hz, and a vehicle speed on the order of 3-5 m/s, it was assumed that concentration measurements were sufficiently far apart that each measurement can be treated as independent. Thus, the errors propagated to the inferred emission rate by each measurement are independent. What follows from that is a likelihood function that is a modified version of Eq. (4-1).

$$p(c_j^{\text{meas}} | q^{\text{est}}) = \frac{1}{(2\pi)^{n/2} \prod_{j=1}^n \sigma_{cj}} \exp\left(-\sum_{j=1}^n \left[\frac{\{c_j^{\text{meas}} - c_j^m(q^{\text{est}})\}^2}{2\sigma_{cj}^2} \right]\right) \quad (4-2)$$

where c_j^{meas} is the concentration measurement at a specific measurement location, j , within the transect; c_j^m is the modelled concentration for a candidate q^{est} at a specific measurement location within the transect; σ_{cj} is the model uncertainty associated with a specific point concentration measurement, which again, is assumed to dominate the total uncertainty; and n represents the total number of point concentration measurements within a transect. Accurate determination of the uncertainty, σ_{cj} , relies on some knowledge of the model error, which is investigated through CFD analysis in the following chapter of this thesis.

4.2 Treatment of Priors

In Bayesian analysis, the prior PDFs represent what is known about a particular variable before measurements take place. For this analysis, a uniform, non-negativity prior is applied to the emission rate; all that is known about q prior to the measurements is that q cannot be less than 0 kg/h. The wind speed is obtained deterministically from the anemometry data as the average reading from the anemometer over the course of a transect measurement. The wind direction is

defined as the direction of the vector between the source position, and the peak concentration. As will be discussed in the following chapter of this thesis, it was found that uncertainties in the dispersion parameters, σ_y and σ_z , were significant sources of uncertainty in emission rate estimates. As such, these parameters are fitted with non-negative, or “clipped”, Gaussian priors, that allow for the error of neighboring stability classes would fit within one standard deviation of the fitted distribution. For example, for three different stability classes, A, B, and C, there are corresponding values for the horizontal dispersion parameter, σ_{yA} , σ_{yB} , and σ_{yC} . In the case that the meteorological conditions indicate stability class B, the dispersion parameter is fitted with a Gaussian prior centred on σ_{yB} , such that σ_{yA} and σ_{yC} are contained within one standard deviation of the distribution. In effect, the the values of σ_{yA} and σ_{yC} are contained within the plausible interval centred on σ_{yB} . This process is performed independently for each transect and a visualization of this can be seen in Figure 4-1.

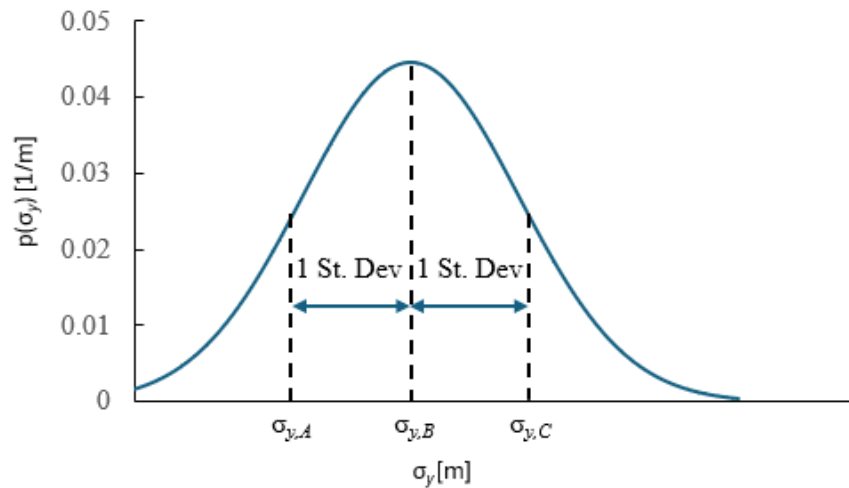


Figure 4-1: Visualization of the Gaussian prior on σ_y .

4.3 The Posterior PDF

The result of the Bayesian inference is a joint posterior PDF that combines the release rate and the dispersion parameters. To obtain the posterior PDF of the emission rate, this PDF is marginalized over the two dispersion parameters:

$$p(q|\mathbf{c}) = \int_{-\infty}^{\infty} \int_{-\infty}^{\infty} p(q, \Phi|\mathbf{c}) d\sigma_y d\sigma_z \quad (4-3)$$

From this posterior distribution, the highest probability emission rate, q^{map} , comes from the *maximum a posteriori* (MAP), where q^{map} is taken as the release rate corresponding to the highest probability in the posterior PDF. The emission rate uncertainty is quantified using 90% CIs; in theory, there is a 90% probability that the true release rate is contained within the CI. Figure 4-2 shows visually how the MAP and CIs are determined. Note that q^{high} and q^{low} refer to the emission rates corresponding to the upper and lower limits of the 90% CI respectively.

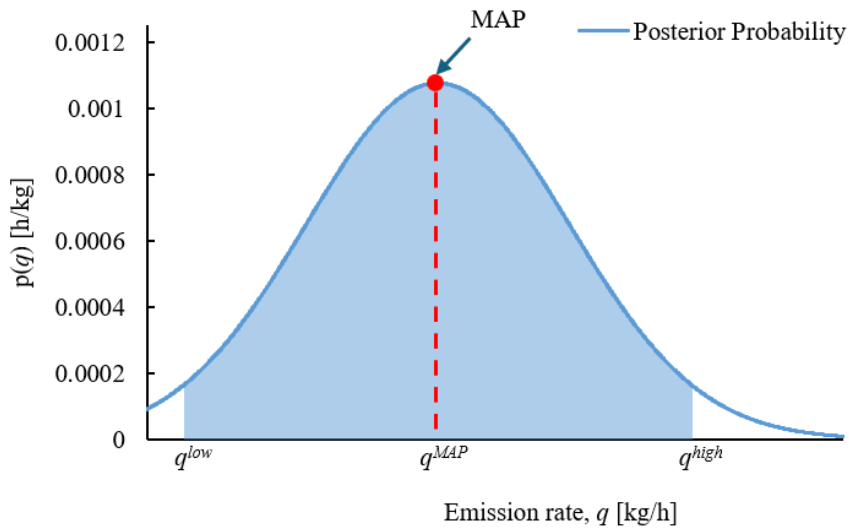


Figure 4-2: Visualization of the posterior distribution, q^{MAP} , and credibility interval.

The definitions of the CIs are ambiguous, as any interval containing a fixed probability of the posterior can be defined as the CI for the specified probability. Two common choices for defining

the CIs are highest posterior density (HPD) and “equal tails” CIs (ETCIs). ETCIs are often used do to the simplicity in formulating the CI [77]. ETCIs are formulated such that the probability on either side of the distribution is equivalent. For example, with a 90% CI, 5% of the total probability mass is excluded on either side of the CI. HPD CIs, however, are formed such that only the values with the lowest probability are excluded, while satisfying the desired probability mass [77]. Conceptually, these intervals can be formed by sorting data by their associated probability densities, and progressively eliminating the datapoint with the lowest probability density until the desired probability mass (e.g. 90%) is achieved. The remaining data represents the data contained within the HPD CI. For a unimodal (single peak) distribution, as is the case with the posterior distributions obtained through this analysis, the HPD CI will always be one continuous interval. For an un-skewed, unclipped Gaussian distribution, the HPD CI and the ETCI are identical. The difference between the two types of CI is seen when dealing with skewed, clipped, or otherwise asymmetric distributions. For example, in the distribution seen in Figure 4-3, an ETCI would clip the interval at the far right of the distribution, as well as near the zero-axis. This would result in some of the data with the highest probability near the zero-axis being excluded from the resulting CI. An HPD CI however would include the highest probability values, and only exclude the lower probability values at the right side of the distribution. In general, the HPD approach provides a more coherent view of where the parameter values are most probable and is therefore a better choice for asymmetric distribution.

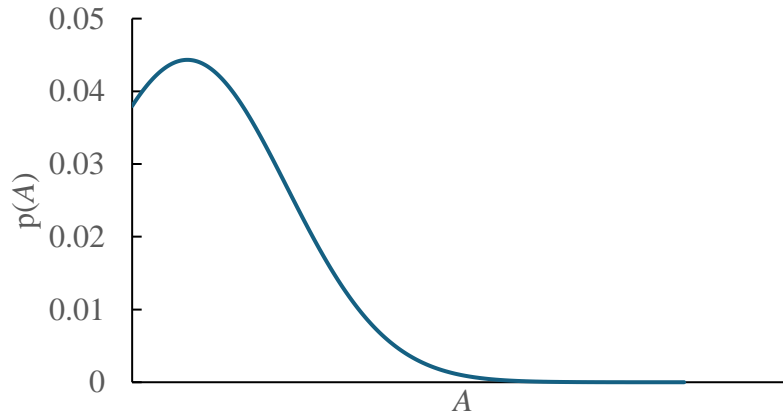


Figure 4-3: Asymmetric distribution, typical of the posterior distributions of the emission rate.

Due to the fact that the emission rate is strictly non-negative, it is possible (and even common) for the resulting posterior distribution to resemble a skewed or clipped Gaussian distribution. Therefore, to accurately represent the true probabilities of the emission rate, it was necessary to construct HPD intervals to ensure that only the emission rates with the lowest probability were excluded from the interval.

5 CFD Investigation into Model Error

As mentioned in the previous chapter, some understanding of the model error is crucial in forming a likelihood function that accurately represents the relationship between the emission rate, the data observed, and the model implemented. This chapter discusses the CFD simulations that were used to investigate the model error associated with the GPM, that was then used in the likelihood function. An overview of the initial, low-fidelity Reynold's Averaged Navier Stokes (RANS) simulations is provided, as well as details on the issues encountered when using these initial simulations. The chapter then outlines the more intensive, high-fidelity simulations that were performed, and how comparisons from these simulations were used to investigate the error associated with the GPM. The objective of the CFD analysis was to synthetically generate a "ground-truth" set of concentration data that was representative of the plume characteristics of the field trial. By comparing this "ground-truth" to the predictions of the GPM under similar release and atmospheric conditions, some investigation of the errors directly associated with the model was performed.

5.1 Initial RANS simulations

As an initial investigation into the error of the GPM, a series of Reynolds-Averaged Navier-Stokes (RANS) simulations were performed using OpenFOAM [78]. The core principle of RANS simulations involves the application of Reynolds-averaging to the Navier-Stokes equations, which govern the motion of fluid substances [79]. The Navier-Stokes equations are derived from the conservation of mass, momentum, and energy within a fluid flow. These equations, in their instantaneous form, are notoriously complex when applied to turbulent flows due to the chaotic nature of turbulence [79, 80]. Reynolds-averaging decomposes the instantaneous fluid properties

into mean and fluctuating components, similar to the discussion on the Reynolds decomposition of the advection-diffusion equation, Eq. (3-2), presented in Section 3.1. This decomposition results in the Reynolds-averaged Navier-Stokes equations, which describe the mean flow characteristics while accounting for the effects of turbulence through additional terms known as Reynolds stresses [81]. The key challenge in RANS simulations is the accurate modeling of these Reynolds stresses, as they are not directly resolved but instead modeled using turbulence models.

For the purposes of this investigation, the release of methane from a pipe, representative of the controlled releases from the modular vent stack during the field measurements, was simulated. The use of RANS simulations was initially attractive due to the lower computational costs associated with the procedure [80]. However, due to the approximations in the modelling of the Reynolds stresses, these simulations are not as effective in capturing more complex turbulent structures that are important to way the plume actually disperses [80, 82]. Thus, the simulated plume was not reflective of the emissions that were measured during the field campaigns. In particular, the phenomenon of plume meandering was absent in the simulations, and the plume was instead very narrow, and the centreline of the plume was throughout the domain. As such, it was determined that more intensive simulations were needed for this investigation, and the RANS simulations were treated as a “proof of concept” in terms of the simulation of methane dispersion for model error investigation.

5.2 Detached Eddy Simulation (DES)

Following the initial findings from the RANS simulations, it became clear that a more sophisticated approach was required to accurately capture the complex dynamics of methane plume dispersion observed during field trials. The limitations of RANS, particularly in its inability

to resolve the finer turbulent structures and the phenomenon of plume meandering, necessitated the use of a higher-fidelity simulation technique. As a result, Detached Eddy Simulation (DES) was chosen as the next step in the computational investigation.

Detached Eddy Simulation is a hybrid technique that combines RANS simulations of regions where turbulence is small, and the flow is predictable, with Large Eddy Simulation (LES) of regions where the turbulence is more important and the flow is more complex [83]. The concept of LES is to resolve only the relevant large-scale turbulence structures through filtering of the Navier-Stokes equations [84] to more accurately represent the transient turbulent structures compared to RANS simulations, though the LES method incurs more computational costs. The use of LES for plume modelling is fairly widespread due to its ability to more accurately capture plume dispersion in turbulent air [65]. This includes the work of Caulton et al. [23], who used LES modelling to investigate the GPM. This work is outlined in Chapter 1, and forms a basis for the CFD investigation outlined in this thesis. In combining the two simulation strategies (RANS and LES), the DES technique provides a way to resolve the turbulence that RANS simulations would otherwise miss, while not incurring significant computational costs compared to an LES of the full domain [83].

For this investigation, a DES of a 37 kg/h CH₄ release from a 1.7m stack (representative of the 1.7m tall modular stack) was performed using OpenFoam v2112 [78], modelling the CH₄ concentration as a passive scalar. The computational domain is 16.5m tall, 45m wide, and 130m in length. The domain is discretized using approximately 22 million grid points. The DES relies on LES of most of the computational domain, except near the wall regions, which employ a RANS approach. One key step in the replication of the controlled release data was the application of synthetic turbulence upwind of the stack location. By applying synthetic turbulence with a

stochastic boundary condition 10m upwind of the source location to a freestream velocity of 2.0 m/s, the large-scale turbulent structures representative of real-world measurements was adequately recreated in the DES. A snapshot of the DES can be seen in Figure 5-1.

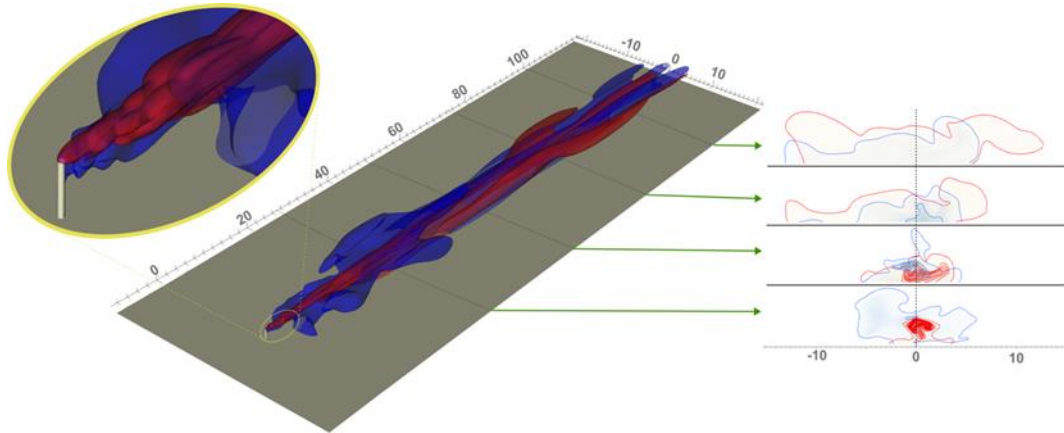


Figure 5-1: Isocontours of methane concentration from CFD simulation at two separate time instances. Four cross-plane slices of the local concentration are shown for identical isocontour lines for both cases.

5.3 Comparison of CFD concentration data to GPM predictions

As mentioned previously, the model error investigation consisted of comparisons between the concentrations obtained from the CFD simulation to the predictions of the GPM with similar model parameters, Φ . Even with the higher-fidelity DES, the simulated plume was found to be significantly narrower than what was observed in real-world conditions and indeed narrower than the predictions of the GPM. Again, this error was attributed to uncertainty in the dispersion parameters, σ_y and σ_z , which govern the spread of the plume in the horizontal and vertical directions respectively. As such, when analyzing the numerical CFD data, these parameters are inferred by a least-squares fit between the GPM and the CFD data. When analyzing the experimental data, these parameters are fit with the Gaussian prior outlined in the previous chapter of this thesis. The reason

for discrepancies between the plume widths for the GPM, the DES, and the real-world measurements was not specifically investigated, however one potential explanation is the fact that the DES does not account for some of the ambient conditions, such as localized changes in the wind direction downwind from the source, wind shear, and other ambient turbulence structures. These conditions would contribute to increased plume spread downwind, and the absence of these in the DES could explain why the simulated plume was narrower than the real-world measurements.

The model error, ε , is investigated by comparing the CFD concentrations to the GPM predictions. In addition to a small number of fully resolved “snapshots” of the simulated plume, concentration data was obtained at specific “probe” locations downwind of the source location for all timesteps. These probe locations represented plume transects at 50m, 75m, and 100m. By taking the CFD data as a ground truth, the model error can be defined as:

$$\tilde{\varepsilon}(\mathbf{r}, \Phi) = \left[1 - \frac{d^{\text{GPM}}(\mathbf{r}, \Phi)}{\tilde{d}(\mathbf{r})} \right] = \left[1 - \frac{\bar{c}(q, \mathbf{r}, \Phi)}{\tilde{c}_{\text{CFD}}(q, \mathbf{r})} \right] \quad (5-1)$$

Due to the turbulence associated with the simulated plume, the error term is a stochastic quantity. It is also expected that the error term will be independent of the emission rate, q , as the emission from the stack is not momentum driven. Instead, the error term represents only the errors associated with inaccuracies and simplifications in the dispersion modelling of the GPM. As mentioned in the first chapter of this thesis, the near-field region of the plume is of particular importance, due to the increased effects of plume meandering in this region.

Figure 5-2 shows a map of ε for the entire domain for a snapshot of the plume. From the different snapshots of ε , it is possible to derive distributions of ε for various points in a transect. In this case, Figure 5-3 shows the distribution of ε across all timesteps for a transect 100m downwind

of the source location, using 90% CIs to constrain the error bars associated with each point in the transect. Finally, Figure 5-4 shows an instantaneous comparison of the DES concentrations to the GPM predictions 100m downwind of the source location.

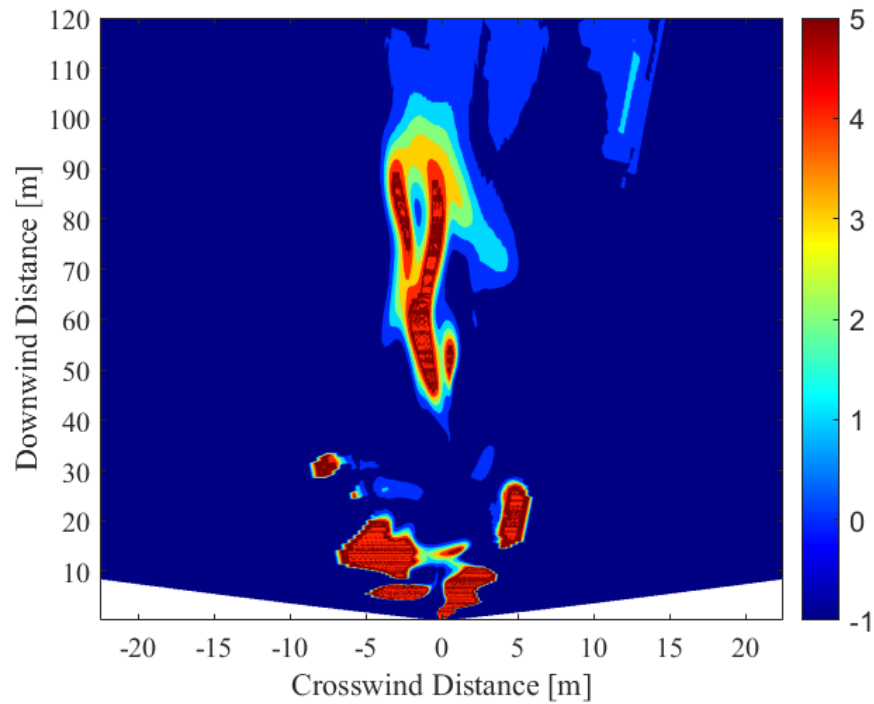


Figure 5-2: Instantaneous map of ϵ at a measurement height of $z = 1$ m.

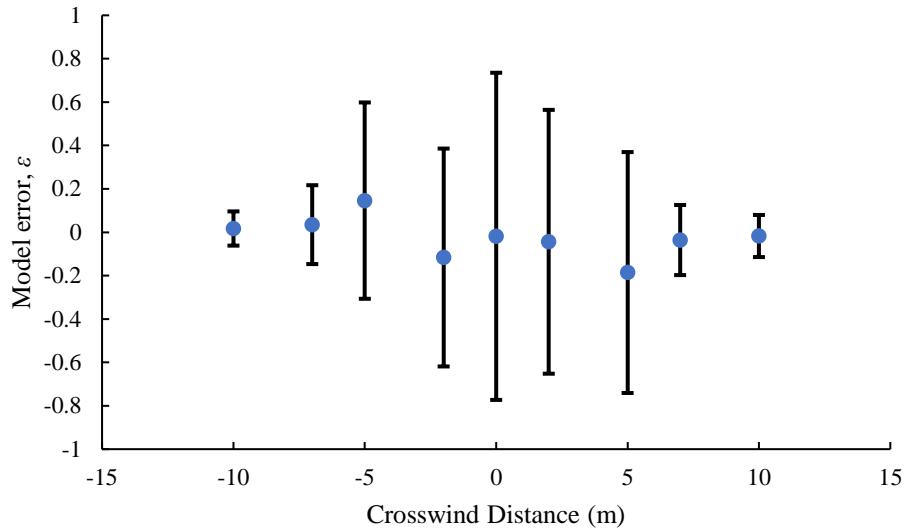


Figure 5-3: Average values for ϵ for a transect located 100 m downwind of the release point. Error bars correspond to a 90% credible interval.

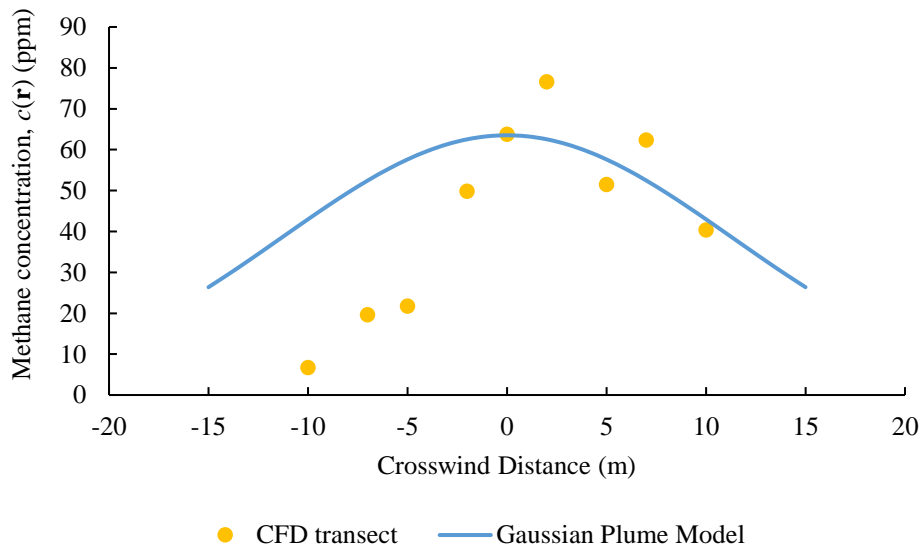


Figure 5-4: Comparison of GPM to LES concentrations for an instantaneous transect located 100 m downwind of the source location.

In analyzing the results of the DES to GPM comparison, ϵ appears relatively unbiased and normal in distribution for distances greater than approximately 100m downwind. Nearer to the

source location (within about 80m), it can be seen in the data that ε becomes larger and biased with increasing error with the GPM. This can be attributed to the effects of the meandering regime closer to the plume, where instantaneous fluctuations in the plume's centre of mass due to larger scale turbulence dominates the dispersion of the methane compared to the plume spread that the GPM actually models. Linking these results back to the model error in the likelihood function, because ε is defined directly as errors in the concentrations predicted by the GPM, σ_{cj} can be directly constructed from the distributions of ε for specific points in the transect, and then used in the Gaussian likelihood function for specific point concentration data from the field measurements.

6 Results of Field Data Analysis

After determining the model error, the Bayesian inference is performed for the plume transect data obtained from the field measurement campaigns. This chapter presents the results of this inference, and the implications of these results. This chapter starts with a discussion on how uncertainty is defined for the purpose of investigating factors that effect uncertainty. The high level, overall results are presented, with visualization of the posterior PDFs and CIs. Finally, this chapter discusses what factors appear to, and appear not to affect the uncertainty of inferred emission rates.

6.1 Defining uncertainty for investigating the results

Before examining the results of this work, it is important to note that there are different ways of describing and comparing the uncertainties between measurements, looking at the relative uncertainty, or the absolute uncertainty. Due to the wide range of emission rates investigated, in this work the uncertainties are defined as the relative uncertainties, ε_{rel} , and represent the width up the CI relative to the q^{MAP} :

$$\varepsilon_{rel} = \frac{q^{95\%} - q^{5\%}}{q^{MAP}} \quad (6-1)$$

where ε_{rel} is the relative uncertainty; $q^{95\%}$ and $q^{5\%}$ represent the upper and lower limits of the 90% CI. A Spearman rank-order correlation test is used to evaluate the correlation between ε_{rel} and the factors investigated. The Spearman test is an alternative to the Pearson test, which evaluates linear correlations between two variables [85]. Unlike the Pearson test, the Spearman test allows for non-linear relationships, is less sensitive to outliers, and describes the general trend of how the dependent variable increases or decreases in relation to changes in the independent variable [85,

86]. The absolute value of the correlation coefficient is used to determine the strength of the correlation, for example as outlined in Table 6-1.

Table 6-1: Strengths of Correlations [87]

Absolute Value of Coefficient	Strength of Correlation
Greater than 0.8	Very Strong
0.6 to 0.8	Moderately Strong
0.3 to 0.6	Fair
Less than 0.3	Poor/Negligible

Another way to investigate the factors affecting uncertainty is in looking at the frequency with which the true emission rate falls outside of the 90% CI. Since the 90% CI is defined such that there is a 90% probability of the true rate being within the CI, it follows that the true emission rate should fall outside of the 90% CI 10% of the time (with adequate sample size). Should conditions arise where this frequency is larger than 10% of the time, it would indicate that these conditions are contributing to larger uncertainties, and/or uncertainties that are not adequately captured in the model error investigation.

6.2 Overall results

In total, data from 129 transects across 98 releases were analyzed for this thesis. A summary of the transects performed for each type of releasing equipment and for each release rate can be seen in Table 6-2 and Table 6-3 respectively. Note that these tables only summarize data for which transect data from the technology provider was reported. For example, a number of release

scenarios are not represented in this data due to data logging errors with the concentration sensor and missing meteorological data.

Table 6-2: Summary of transects performed for different releasing equipment

Releasing Equipment	Number of Transects
1.7m Tall Vent Stack	34
3.4m Tall Vent Stack	8
4.8m Tall Vent Stack	22
Equipment Shed	10
Storage Tank	37
Unlit Flare	18

Table 6-3: Number of transects performed for each release rate.

Release Rate [kg/h]	Number of Transects
0.25	9
1	8
1.5	11
2.5	13
5	22
10	13
21	11
35	15
40	8

50	19
----	----

As mentioned previously, the posterior PDFs are obtained by using Eq. (4-3) to solve for the likelihood and priors, using the emission rate, q , as a variable, while the 90% CIs quantify the uncertainty. Figure 6-1 shows a representative set comparing the true emission rate to values of q^{MAP} with associated CIs. An example posterior PDF highlighted to visualize how the quantification works. Figure 6-2 shows the results for the entire set of transects analyzed. Note that in Figure 6-2, the CIs are omitted for visual clarity.

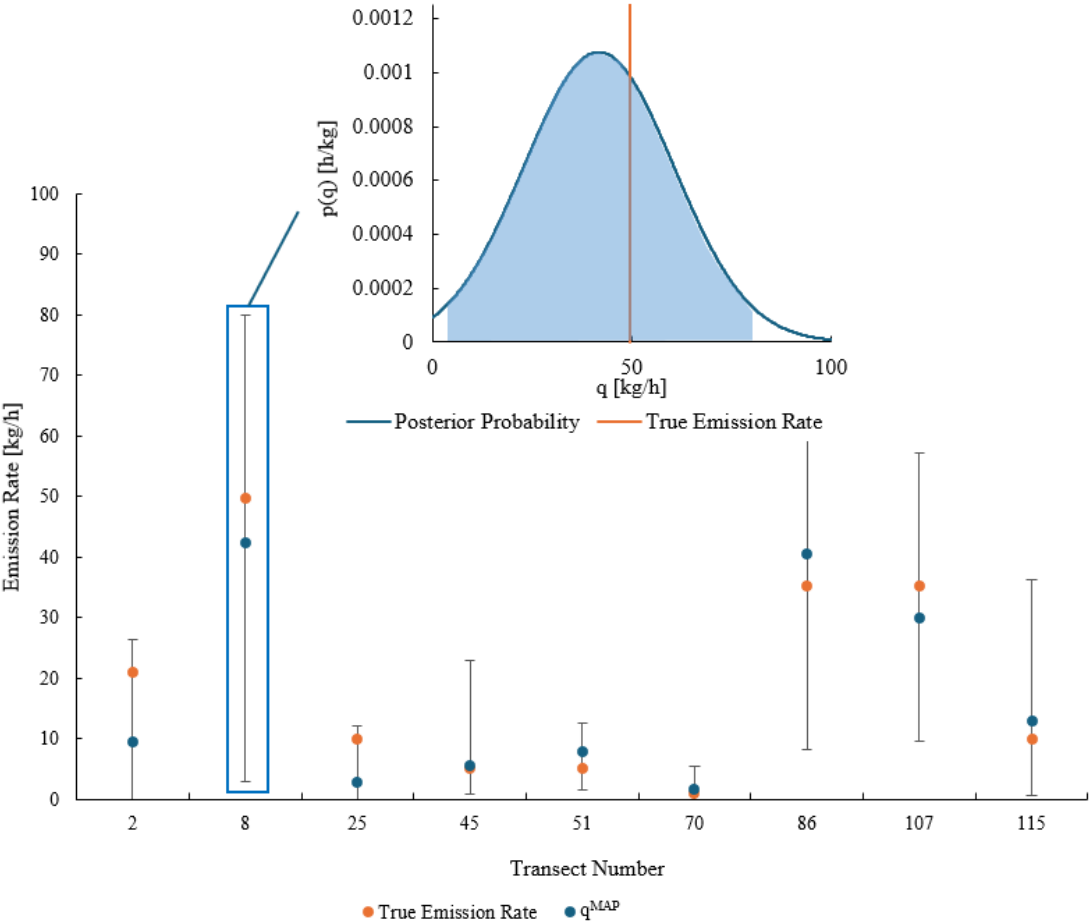


Figure 6-1: Representative set of q^{MAP} and CIs for the transects analyzed, with a visualization of the posterior PDF for transect number 8.

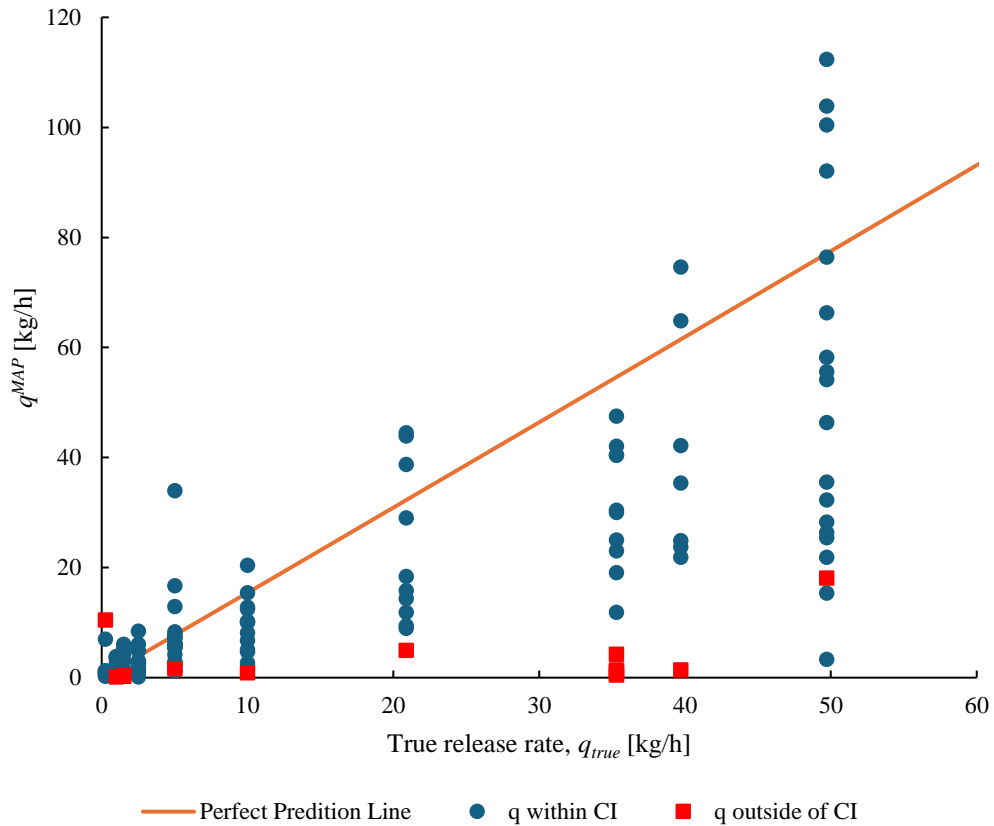


Figure 6-2: Comparison of q^{MAP} to the true emission rates for the entirety of the analyzed transects.

While the comparison of the MAPs to the true emission rates can give some information into the bias/skewedness of a quantification technique, the more important result is in whether or not the true emission rate falls within the CI. Overall, from the 129 transects analyzed, the true emission rate fell within the CI 115 times, or 89.15% of the time. This is in line with the expected frequency of 90%, indicating that the true uncertainty of the emission estimates is represented in the CIs. This further highlights the importance of viewing emissions uncertainty from a probabilistic standpoint, and points to the value of Bayesian inference as a tool for uncertainty analysis, rather than comparisons of point estimates to true release rates.

6.3 Factors affecting uncertainty

In addition to looking at the overall results with respect to uncertainty, it is important to identify what factors do or do not affect emission inference uncertainty, as this can point to limitations of a specific technology, the measurement model used, or the specific combination of the two. This section looks at the effects (if any) that the release rate, downwind measurement distance, absolute wind speed, and wind variability have on the uncertainties of emissions inferences.

6.3.1 True release rate

Figure 6-3 shows the relative uncertainty with respect to the true emission rate. As expected, there are no clear trends regarding the relative uncertainties and the true emission rate. The Spearman correlation coefficient between ε_{rel} and the true release rate was -0.19, indicating poor correlation between the two variables. Similarly, between the higher (≥ 10 kg/h) and lower (< 10 kg/h) emission rates, there were no significant trends with respect to the emission rate falling within or outside of the CI, as shown in Table 6-4.

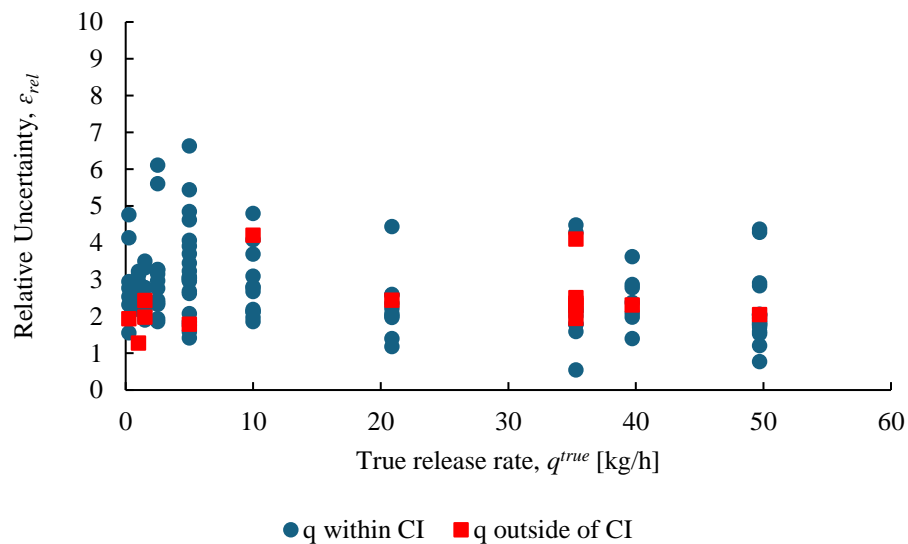


Figure 6-3: Relative uncertainty vs true release rate

Table 6-4: Frequency of q being outside of the CI vs true release rate

Value	Low releases (q < 10 kg/h)	High Releases (q >= 10 kg/h)
q within CI	58 Occurrences	57 Occurrences
q outside of CI	5 Occurrences	9 Occurrences
% of q outside of CI	7.9%	13.6%

These findings are consistent with the fact that the methane released from the source location is effectively a low-momentum jet, and the measurements are made far enough downwind to negate any momentum-driven effects. This also highlights the fact that the errors in the likelihood function, and subsequent width of the 90% CIs are driven almost entirely by errors in the GPM.

6.3.2 Downwind Distance

As seen in the CFD analysis, and in the literature review of previous work in vehicle-based methane quantification uncertainty, the downwind measurement distance can have a very large effect on the model error, particularly in the meandering regime close to the plume source. The results of the uncertainty investigation with respect to downwind transect distance are summarized in Figure 6-4 and Table 6-5.

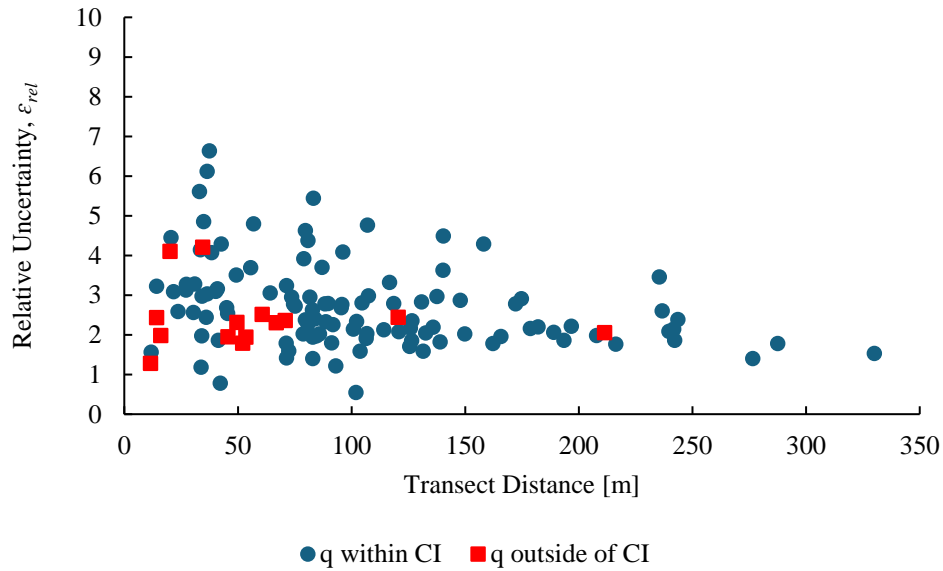


Figure 6-4: Relative uncertainty vs transect distance

Table 6-5: Frequency of q being outside of the CI vs measurement distance

Value	Near source (< 70 m)	Far from source (>70 m)
q within CI	33 Occurrences	82 Occurrences
q outside of CI	11 Occurrences	3 Occurrences
% of q outside of CI	25.0%	3.5%

There is a clearer trend of increased relative uncertainty when closer to the plume, evident in Figure 6-4. The Spearman correlation coefficient between ϵ_{rel} and the measurement distance was -0.31, indicating a moderately negative correlation between the two variables; as the measurement distance increased, the relative uncertainty decreased. Furthermore, Table 6-5 shows that the frequency of the true emission rate being outside of the CI is disproportionately represented in emission inferences derived from transects close to the plume. Despite these “close” transects representing only 34% of the total number of transects performed, they account for 79% of the

transects where the true emission rate was outside of the CI. This finding is consistent with the idea that the meandering of plumes close to the source location causes the GPM to depart significantly from reality when compared to the relative dispersion region further downwind from the source location [66]. Other studies have shown that at close distances (within 50m of the source location), lognormal distributions perform better for describing the dispersion of the plume, while a gamma or gaussian distributions perform better further away from the plume (beyond 80-100m depending on the study) [23, 1, 69]. The measurement distance had the highest correlation to the relative uncertainty, highlighting the importance of understanding how different regions of plume dispersion characteristics can affect uncertainty.

6.3.3 Wind Effects

Figure 6-5 shows the relative uncertainties with respect to the wind speed. The wind speed is defined here as the average measured windspeed from the anemometer during the time window where a specific transect measurement was taking place. While there is no significant correlation between the relative uncertainty of the emission inferences and the wind speed (the correlation coefficient was calculated as -0.14), in looking at the transects where the true emission rate was outside of the CI, these occurrences were disproportionately represented in instances where the wind speed was very low (defined as less than 1.5 m/s), shown in Table 6-6.

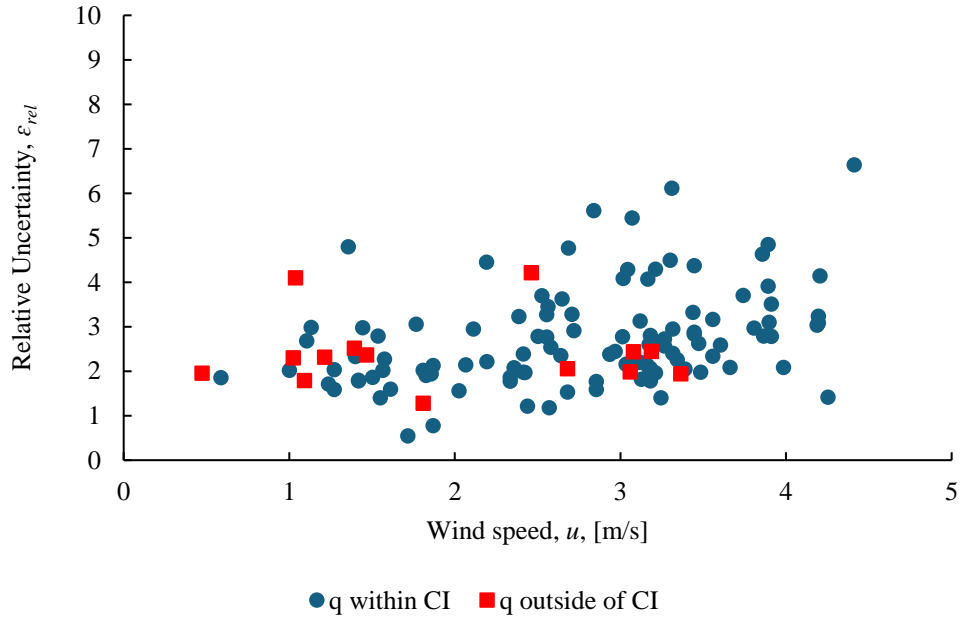


Figure 6-5: Relative uncertainty vs wind speed

Table 6-6: Frequency of q being outside of the CI vs wind speed

Value	Low wind (< 1.5 m/s)	High wind (>1.5 m/s)
q within CI	13 Occurrences	102 Occurrences
q outside of CI	7 Occurrences	7 Occurrences
% of q outside of CI	35.0%	6.4%

One of the factors that was important to investigate with respect to the wind was the variability of the wind, both in terms of its magnitude and its direction. It was thought that the effects of wind variability would be very important for the uncertainty, as instantaneous variations in the wind speed and wind direction during measurements are not accounted for by the GPM, which assumes a constant mean wind direction and magnitude. To investigate this, the statistical variance of both the wind speed and the wind direction was calculated for each measurement window. Similar to

the previous figures, the MAP results were then plotted against these values, seen in Figure 6-6 and Figure 6-7.

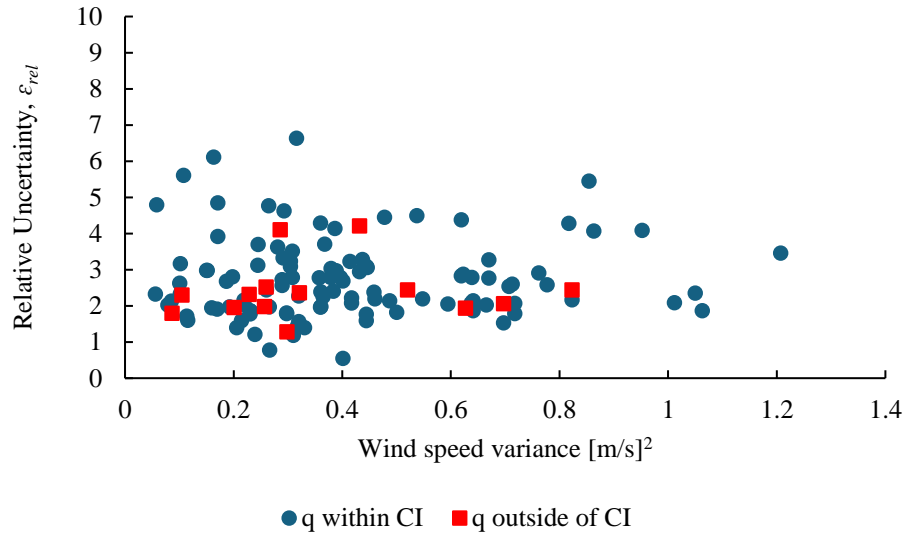


Figure 6-6: Relative uncertainty vs wind speed variance

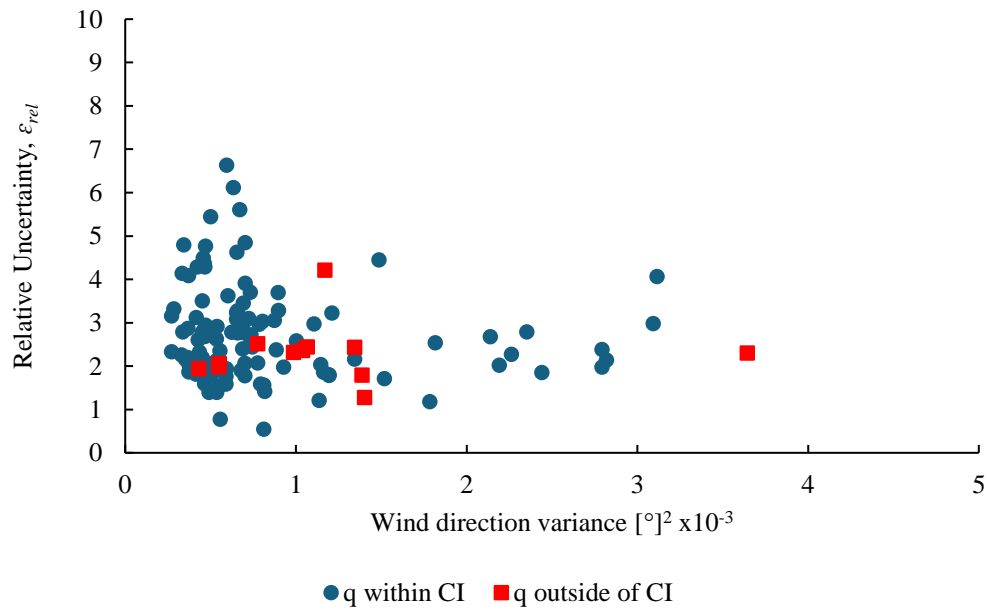


Figure 6-7: Relative uncertainty vs wind direction variance

From Figure 6-6 and Figure 6-7, there were no clear trends with respect to the relative uncertainty of emissions inferences and the wind speed variance. Furthermore, while there is some overrepresentation of instances of q being outside of the CI with high variance in the wind direction, the effect that variance in the wind direction has on the relative uncertainties is not clear. The correlation coefficients associated with the wind speed and wind direction variance were both near zero, indicating negligible correlation to the relative uncertainty. This result was unexpected, as it was originally thought that a departure from the assumptions made in the GPM (in this case, steady wind), would lead to larger model uncertainty, but that is not seen in these results. Instead, it may be the case that to some extent, increases in turbulence lead to conditions more consistent with the atmospheric dispersion that is modelled by the GPM, resulting in improvements in the model that outweigh the potential negative impacts of the steady-wind assumptions the GPM is built upon. For example, in the investigation Zhou et al. [1] performed into different likelihood functions (outlined in Chapter 1), they found that when obstacles to the flow were present, these obstacles caused an increase in turbulence downwind that promoted mixing of the plume, leading to the Gaussian likelihood function performing better than the log-normal likelihood functions. However, one would expect a limit to which increased turbulence in the flow field can improve GPM estimation. For example, when the wind direction was shifting dramatically during measurements, the operators from Boreal laser reported significant difficulty in being able to find and measure the plume downwind. Furthermore, the results in Figure 6-5 point to limitations of the GPM in terms of needing a minimum wind speed to properly define the plume. This is consistent with other literature that has found limitations in dispersion models including the GPM, particularly where these models become less applicable at low wind speeds due to irregularities in the plume diffusion [23, 87].

7 Conclusions and Future Work

7.1 Key Findings

The understanding of uncertainties in methane emissions quantification is crucial for the accurate application of regulations, LDAR programs, as well as in the predictions of the future effects of anthropogenic emissions on climate change. Referring to the original objectives of this project, the overall goal was to use a combination of Bayesian inference and CFD modeling to understand the model error associated with the GPM and apply this investigation to describe the uncertainty of emissions estimates obtained using the GPM.

One of the key results from this analysis is the fact that the true emission rates fell within the calculated 90% CIs with nearly a 90% frequency. This result validates the use of Bayesian inference for accurate uncertainty quantification in emission estimates, and emphasizes the importance of using probabilistic approaches, like Bayesian inference, particularly in environmental applications where uncertainties are inherently complex. The effective representation of uncertainties in the CIs suggests that the model error determined by the CFD analysis is well-calibrated to the specific application, which underscores the value in using high-fidelity modelling such as DES for investigations into dispersion model uncertainty. While this is not the first investigation into model error and uncertainty using these tools [23, 1, 50, 55], this work represents a significant advancement in this analysis in terms of how the uncertainties across all point concentration measurements are incorporated into the overall uncertainty for a particular plume transect. By investigating the model error across the entirety of point-concentration measurements throughout the transect, a more robust description of the error is used in the likelihood function, leading to better representation of the true uncertainty of emissions estimates when performing the Bayesian inference.

Other key findings from this work include the investigations into the factors affecting the uncertainty of emissions estimates. These findings have direct applications in industry, in terms of informing operators about the limitations and applicability of measurement techniques. For example, one of the main factors that was found to affect the uncertainties of the emission estimates was the measurement distance, where measurements very close to the plume in the “meandering region” were significantly more uncertain and less applicable than measurements further from the plume. In industry, this can be applied when considering optimal paths for vehicles taking measurements downwind of a plume. Depending on the assumptions made by the dispersion model used for quantification, operators must ensure that the plume characteristics at the measurement location are consistent with the model. In the case of measurements relying on the GPM for quantification, operators need to ensure that the measurements are taking place far enough downwind from potential sources, to ensure that the plume has fully developed and is stable enough that the GPM is applicable to the measurements. The same considerations must be made for the environmental conditions. It is important for operators to understand how these conditions affect the uncertainty and applicability of measurements and models, such as the fact that in this study, the GPM-derived emissions estimates seemed to be limited at very low wind speeds. Overall, this study highlights the importance for operators to consider the uncertainty of measurements and quantification techniques, and points to the value in the use of uncertainty quantification for the reporting of meaningful results.

7.2 Limitations

One of the primary limitations lies in the reliance on CFD simulations to model the methane dispersion under controlled conditions. While high-fidelity CFD analyses such as DES offer high-

resolution insights into flow patterns and turbulence, they also require significant computational resources and are sensitive to boundary conditions and grid resolution, which can have significant effects on the diffusion characteristics. One of the ways this study was impacted by the high computational costs of the DES analysis was a less systematic evaluation of the parameters of the dispersion model. As an example, the effects of significantly different wind speeds on the model error were not investigated with the CFD analysis; the model-error analysis was performed using a simulation of a single release at different timesteps. However, it is clear from the results of the Bayesian inference that at very low wind speeds, the model error becomes much larger than what was identified from the CFD analysis. With more computational resources, it would be possible to run similar CFD simulations with very low wind speeds to investigate the model error at these conditions. The results from this investigation could then be applied to the measurements at low wind speeds, and the results of the Bayesian inference for these measurements might then be improved.

Another limitation to the study is the topography of the field measurement site, as well as the topography of the CFD simulation. Releases for the most part were performed in an open, flat area surrounded by flat prairie. Similarly, the CFD simulation was completely flat, except for the stack from which the release was taking place. If the results of this analysis (or a similar analysis) were to be applied to a second set of measurements, it would be very important to consider any topographical differences between the different measurement sites. This would be especially important for measurement sites with many significant natural or artificial obstacles present, as this may in fact improve the accuracy of Gaussian plume modelling [1].

7.3 Recommendations for Future Work

As mentioned in the previous section, one potential avenue for future work would be a more parameterized CFD investigation into the model error. While this would incur significant computational costs with repeated, high-fidelity DES analyses, parameterization of the model error, and thus the likelihood function, could result in a deeper understanding of the uncertainties associated with this model and measurement technique. This could also be useful for applications to different models and/or measurement techniques, especially in situations where access to controlled release data is limited.

Another area for future work is the incorporation of more priors and different likelihoods in the Bayesian inference. For example, by looking at the wind speed variance and the wind direction variance, a PDF for the wind direction and wind speed could be constructed and implemented for the modelled concentrations in the Bayesian inference. The same can be said for the atmospheric dispersion parameters, σ_y and σ_z , where a more thorough investigation of meteorological data and of the parameters themselves could allow for the formation of a more physics-based prior for these parameters. On the subject of priors, future work could also include the implementation of more informative priors on the emission rate, q , or in the case of future measurements with multiple repeated plume transects, the use of a Bayesian updating procedure for the prior applied to q , similar to what is outlined by Zhou et al [1, 55]. Similar to Zhou et al. [1], it would also be interesting to investigate different likelihood functions for the data, particularly for measurements where the uncertainties in the Gaussian-based inference were very high.

Finally, future work should include the development of uncertainty analysis using Bayesian inference for a wider range of quantification technologies. One of the goals of this project was to have a procedure for uncertainty analysis that could be widely applied to the industry of methane

emissions quantification. While the results of this thesis have been focused on truck-based TDLAS estimates using the GPM, the general procedure outlined can be applied to any technology where the dispersion model is well-known and invertible. This work has shown that through CFD analysis, the errors associated with dispersion models can be identified. In performing this investigation for different technologies, and applying the outlined Bayesian inference for these technologies, a wide-reaching understanding of methane quantification uncertainty could be achieved throughout the industry. This would allow for uncertainty analysis to be incorporated into emissions estimates across the entire range of emission types, equipment, etc. leading to regulations and emissions reduction programs being implemented with the most accurate representation of the reality of methane emissions.

References

- [1] X. Zhou, A. Montazeri and J. D. Albertson, "Mobile sensing of point-source gas emissions using Bayesian inference: An empirical examination of the likelihood function," *Atmospheric Environment*, vol. 218, 2019.
- [2] Environment Canada, "National inventory report : greenhouse gas sources and sinks in Canada 2024.," Ottawa, ON, 2024.
- [3] Government of Canada, "Global Warming Potentials," 2 May 2024. [Online]. Available: <https://www.canada.ca/en/environment-climate-change/services/climate-change/greenhouse-gas-emissions/quantification-guidance/global-warming-potentials.html>. [Accessed June 2024].
- [4] Intergovernmental Panel on Climate Change, "IPCC Sixth Assessment Report," IPCC, 2023.
- [5] Government of Canada, "Regulations Amending the Regulations Respecting Reduction in the Release of Methane and Certain Volatile Organic Compounds (Upstream Oil and Gas Sector)," *Canada Gazette*, 16 December 2023.
- [6] Government of Canada, "Regulations Respecting Reduction in the Release of Methane and Certain Volatile Organic Compounds (Upstream Oil and Gas Sector)," *Canada Gazette*, 26 April 2018.
- [7] United States Environmental Protection Agency, "Waste Emissions Charge," U.S. Environmental Protection Agency, 2024. [Online]. Available: <https://www.epa.gov/inflation-reduction-act/waste-emissions->

- [13] Interstate Technology & Regulatory Council, "Evaluation of Innovative Methane Detection Technologies," Interstate Technology & Regulatory Council, Methane Team, 2018. [Online]. Available: <https://methane-1.itrcweb.org/navigating-this-web-site/>. [Accessed 2023].
- [14] D. R. Tyner and M. R. Johnson, "Where the Methane Is—Insights from Novel Airborne LiDAR Measurements Combined with Ground Survey Data," *Environmental Science and Technology*, vol. 55, no. 14, pp. 9773-9783, 2021.
- [15] National Academies of Sciences, "Improving Characterization of Anthropogenic Methane Emissions in the United States.," National Library of Medicine, Bethesda, MD, 2018.
- [16] Arolytics Inc., "AroFEMP Methane Modelling," 2023. [Online]. Available: <https://www.arolytics.com/arofemp>. [Accessed 2024].
- [17] Carbon Management Canada, "Our Team," 2024. [Online]. Available: <https://cmcghg.com/about-us/our-team/>. [Accessed 2024].
- [18] Clean Resources Innovation Network, "About CRIN," 2024. [Online]. Available: <https://www.cleanresourceinnovation.com/about>. [Accessed 2024].
- [19] Global Methane Initiative, "Petroleum Technology Alliance Canada," 2024. [Online]. Available: <https://www.globalmethane.org/challenge/ptac.html>. [Accessed 2024].
- [20] R. Kang, P. Liatsis and D. C. Kyritsis, "Emission Quantification via Passive Infrared Optical Gas Imaging: A Review," *Energies*, vol. 15, no. 9, p. 3304, 2022.

- [21] J. T. Shaw, A. Shah, H. Yong and G. Allen, "Methods for quantifying methane emissions using unmanned aerial vehicles: a review," *Philosophical Transactions of the Royal Society A*, vol. 379, no. 2210, 2021.
- [22] Y. Chen, E. D. Sherwin, E. S. Berman, B. B. Jones, M. P. Gordon, E. B. Wetherley, E. A. Kort and A. R. Brandt, "Quantifying Regional Methane Emissions in the New Mexico Permian Basin with a Comprehensive Aerial Survey," *Environmental Science and Technology*, vol. 56, no. 7, pp. 4317-4323, 2022.
- [23] D. R. Caulton, Q. Li, E. Bou-Zeid, J. P. Fitts, L. M. Golston, D. Pan, J. Lu, H. M. Lane, B. Buchholz, X. Guo, J. McSpirtt, L. Wendt and M. A. Zondolo, "Quantifying uncertainties from mobile-laboratory-derived emissions of well pads using inverse Gaussian methods," *Atmospheric Chemistry and Physics*, vol. 18, no. 20, pp. 15145-15168, 2018.
- [24] T. A. Fox, C. H. Hugenholtz, T. E. Barchyn, T. R. Gough, M. Gao and M. Staples, "Can new mobile technologies enable fugitive methane reductions from the oil and gas industry?," *Environmental Research Letters*, vol. 16, no. 6, 2021.
- [25] D. J. Varon, J. McKeever, D. Jervis, J. D. Maasackers, S. Pandey, S. Houweling, I. Aben, T. Scarpelli and D. J. Jacob, "Satellite Discovery of Anomalously Large Methane Point Sources From Oil/Gas Production," *Geophysical Research Letters*, vol. 46, no. 22, pp. 13507-13516, 2019.
- [26] National Renewable Energy Laboratory, "Natural Gas Emissions: Measure Top-down or Bottom-up?," 29 October 2018. [Online] [Accessed 2024].

- [27] Innovation Canada, "Technology Readiness Levels," Government of Canada, 2024. [Online]. Available: <https://ised-isde.canada.ca/site/innovation-canada/en/technology-readiness-levels>. [Accessed 2024].
- [28] W. J. Veigle and J. H. Head, "Derivation of the Gaussian Plume Model," *Journal of the Air Pollution Control Association*, vol. 28, no. 11, pp. 1139-1140, 1978.
- [29] B. Crenna, "An Introduction to Windtrax," 2022. [Online]. Available: <http://www.thunderbeachscientific.com/downloads/introduction.pdf>. [Accessed 2022].
- [30] FLIR Systems, "Applications and field results for Quantitative Optical Gas Imaging," in *Finding Petroleum*, 2018.
- [31] A. P. Ravikumar, J. Wang and A. R. Brandt, "Are Optical Gas Imaging Technologies Effective For Methane Leak Detection?," *Environmental Science and Technology*, vol. 51, no. 1, pp. 718-724, 2016.
- [32] R. D. Papa, M. Scafutto and C. R. D. S. Filho, "Detection of Methane Plumes Using Airborne Midwave Infrared (3–5 μm) Hyperspectral Data," *Remote Sensing*, vol. 10, no. 8, 2018.
- [33] Teledyne FLIR, "Optical Gas Imaging (OGI) Cameras for Hydrocarbons," 2024. [Online]. Available: <https://www.flir.com/products/flir-g-series/?vertical=optical%20gas&segment=solutions>. [Accessed 2024].
- [34] Montrose Inc., "Integrated Methane Services," 2024. [Online]. Available: <https://montrose-env.com/services/integrated-methane-services/>. [Accessed 2024].

- [35] OPGAL, "EYECGAS Multi," 2024. [Online]. Available: <https://www.opgal.com/product/eyecgas-multi/>. [Accessed 2024].
- [36] M. Govender, K. Chetty and H. Bullock, "A review of hyperspectral remote sensing and its application in vegetation and water resource studies," *Water SA*, vol. 33, no. 2, 2007.
- [37] M. Kastek, T. Piątkowski, R. Dulski, M. Chamberland, P. Lagueux and V. Farley, "Hyperspectral Imaging Infrared Sensor Used for Chemical Agent Detection and Identification," in *2012 Symposium on Photonics and Optoelectronics*, 2012.
- [38] GHGSat, "Technology," 2024. [Online]. Available: <https://www.ghgsat.com/en/technology/>. [Accessed 2024].
- [39] "HYPER-CAM Airborne Mine," 2024. [Online]. Available: <https://www.telops.com/wp-content/uploads/2023/06/2023-hyper-cam-airborne-mini-eng.pdf>. [Accessed 2024].
- [40] S. Chaulya and G. Prasad, *Sensing and Monitoring Technologies for Mines and Hazardous Areas*, 2016, 2016.
- [41] Winsensor, "What is a TDLAS Methane Sensor, Understanding the Technology and Its Applications," 2023. [Online]. [Accessed June 2024].
- [42] J. Clark, "The Beer-Lambert Law," *Libretexts Chemistry*, 29 January 2023. [Online]. [Accessed June 2024].
- [43] Boreal Laser, "Vehicle Based Gas Detection," 2022. [Online]. Available: <https://boreal-laser.com/products/vehicle-based-gas-detector/>. [Accessed 2022].

- [44] J. Reid and D. Labrie, "Second-harmonic detection with tunable diode lasers — Comparison of experiment and theory," *Applied Physics B*, vol. 26, pp. 203-210, 1981.
- [45] "Infrared laser absorption sensors for multiple performance parameters in a detonation combustor," in *Proceedings of the Combustion Institute*, 2015.
- [46] R. Osibanjo, R. Curtis and Z. Lai, "Infrared Spectroscopy," LibreTexts Chemistry, 2024. [Accessed September 2024].
- [47] G. D. Christian, *Analytical Chemistry - 6th Edition*, New York: John Wiley & Sons, INC, 2003.
- [48] K. Ramaprasad, J. Caldwell and D. McClure, "The vibrational overtone spectrum of liquid methane in the visible and near infrared: Applications to planetary studies," *Icarus*, vol. 35, no. 3, pp. 400-409, 1978.
- [49] C. Häni, M. Bühler, A. Neftel, C. Ammann and T. Kupper, "Performance of open-path GasFinder3 devices for CH₄," *Atmospheric Measurement Techniques*, vol. 14, pp. 1733-1741, 2021.
- [50] M. R. Johnson, B. M. Conrad and D. R. Tyner, "Creating measurement-based oil and gas sector methane inventories using source-resolved aerial surveys," *Communications Earth & Environment*, vol. 4, 2023.
- [51] D. Grunwald, A.-C. Fender, S. Erasmi and H. F. Jungkunst, "Towards improved bottom-up inventories of methane from the European land surface," *Atmospheric Environment*, vol. 51, pp. 203-211, 2012.

- [52] G. Molina-Castro*, "A Monte Carlo Method for Quantifying Uncertainties in the Official Greenhouse Gas Emission Factors Database of Costa Rica," *Frontiers in Environmental Science*, vol. 10, 2022.
- [53] B. M. Conrad, D. R. Tyner and M. R. Johnson, "Robust probabilities of detection and quantification uncertainty for aerial methane detection: Examples for three airborne technologies," *Remote Sensing of Environment*, vol. 288, 2023.
- [54] A. Wigle, A. Béliveau, D. Blackmore, P. Lapeyre, K. Osadetz, C. Lemieux and K. J. Daun, *Estimation and Applications of Uncertainty in Methane Emissions Quantification Technologies: A Bayesian Approach*, Waterloo, ON: University of Waterloo, 2024.
- [55] R. v. d. Schoot, D. Kaplan, J. Denissen, J. B. Asendorpf, F. J. Neyer and M. A. v. Aken, "A Gentle Introduction to Bayesian Analysis: Applications to Developmental Research," *Child Development*, vol. 85, no. 3, pp. 842-860, 2014.
- [56] A. Montazeri, X. Zhou and J. D. Albertson, "On the Viability of Video Imaging in Leak Rate Quantification: A Theoretical Error Analysis," *Sensors*, vol. 21, no. 17, 2021.
- [57] LI-COR Inc., "Trace Gas Analyzers," 2024. [Online]. [Accessed 2024].
- [58] X. Zhou, F. H. Passow, J. Rudek, J. C. v. Fisher, S. P. Hamburg and J. D. Albertson, "Estimation of methane emissions from the U.S. ammonia fertilizer industry using a mobile sensing approach," *Elementa*, vol. 7, no. 19, 2019.

- [59] Picarro, Inc., "G2204 Analyzer Datasheet," 2022. [Online]. Available: https://www.picarro.com/environmental/g2204_analyzer_datasheet. [Accessed June 2024].
- [60] S. Horii, "MLE, MAP and Bayesian Inference," 20 September 2019. [Online]. Available: <https://towardsdatascience.com/mle-map-and-bayesian-inference-3407b2d6d4d9>. [Accessed June 2024].
- [61] Carbon Management Canada, "Newell County Facility," 2023. [Online]. Available: <https://cmcghg.com/facilities-activities/newell-county-facility/>. [Accessed 2023].
- [62] Davis Instruments, "Vantage Vue Weather Station with WeatherLink Console - SKU 6242, 6242M," 2024. [Online]. Available: <https://www.davisinstruments.com/collections/best-sellers/products/vantage-vue-weather-station-with-weatherlink-console>. [Accessed May 2024].
- [63] Alicat Scientific, "2000 SLPM Flow Controller," 2024. [Online]. Available: <https://store.alicat.com/products/mcr-2000slpm-d>. [Accessed May 2024].
- [64] R. M. Young Company, "3D Ultrasonic Anemometer," 2024. [Online]. Available: <https://www.youngusa.com/product/ultrasonic-anemometer/>. [Accessed 2024 May].
- [65] F. Tagliaferri, M. Invernizzi, F. Capra and S. Sironi, "Validation study of WindTrax reverse dispersion model coupled with a sensitivity analysis of model-specific settings," *Environmental Research*, vol. 222, 2023.

- [66] A. Ražnjević, C. v. Heerwaarden, B. v. Stratum, A. Hensen, I. Velzeboer, P. v. d. Bulk and M. Krol, "Technical note: Interpretation of field observations of point-source methane plume using observation-driven large-eddy simulations," *Atmospheric Chemistry and Physics*, vol. 22, no. 10, pp. 6489-6505, 2022.
- [67] C. Hood, A. Stidworthy, K. Johnson, D. Carruthers, G. McCosh and V. H. A. Clegg, "Quantifying methane emissions using inverse dispersion modelling," Environment Agency, Bristol, United Kingdom, 2023.
- [68] A. Ražnjević, C. v. Heerwaarden and M. Krol, "Evaluation of two common source estimation measurement strategies using large-eddy simulation of plume dispersion under neutral atmospheric conditions," *Atmospheric Measurement Techniques*, vol. 15, no. 11, pp. 3611-3628, 2022.
- [69] A. K. Luhar, M. F. Hibberd and M. S. Borgas, "A skewed meandering plume model for concentration statistics in the convective boundary layer," *Atmospheric Environment*, vol. 34, no. 21, pp. 3599-3616, 2000.
- [70] D. Etling, "On plume meandering under stable stratification," *Atmospheric Environment*, vol. 24, no. 8, pp. 1979-1985, 1990.
- [71] R. J. Munro, P. C. Chatwin and N. Mole, "A Concentration pdf for the Relative Dispersion of a Contaminant Plume in the Atmosphere," *Boundary Layer Meteorology*, vol. 106, pp. 411-436, 2003.
- [72] E. Yee, P. R. Kosteniuk, G. M. Chandler, C. A. Biloft and J. F. Bowers, "Statistical characteristics of concentration fluctuations in dispersing plumes in the

- atmospheric surface layer," *Boundary-Layer Meteorology*, vol. 65, pp. 69-109, 1993.
- [73] S. L. Hautala, *Physics Across Oceanography: Fluid Mechanics and Waves*, University of Washington, 2020.
- [74] K. B. Pomeranz, "Conservation Laws and the Dispersal Equations for Chemical and Thermal Pollution," *American Journal of Physics*, vol. 39, no. 9, pp. 1069-1072, 1971.
- [75] National Oceanic and Atmospheric Administration, "Pasquill Stability Classes," U.S. Department of Commerce, 3 January 2022. [Online]. Available: <https://www.ready.noaa.gov/READYpgclass.php>. [Accessed May 2024].
- [76] V. M. Somsikov, "Solar radiation and atmospheric dynamics," *Natural Science*, vol. 6, no. 2, 2014.
- [77] R. Bhattacharya, "Atmospheric Dispersion," 2008. [Online]. Available: <https://ansn.iaea.org/Common/Topics/OpenTopic.aspx?ID=13012>. [Accessed 2024].
- [78] M. Mohan and T. A. Siddiqui, "ANALYSIS OF VARIOUS SCHEMES FOR THE ESTIMATION OF ATMOSPHERIC STABILITY CLASSIFICATION," *Atmospheric Environment*, vol. 32, no. 21, pp. 3775-3781, 1998.
- [79] A. Keats, E. Yee and F.-S. Lien, "Bayesian inference for source determination with applications to a complex urban environment," *Atmospheric Environment*, vol. 41, pp. 465-479, 2007.

- [80] L. Hespanhol, C. S. Vallio, L. M. Costa and B. T. Saragiotto, "Understanding and interpreting confidence and credible intervals around effect estimates," *Brazilian Journal of Physical Therapy*, vol. 23, no. 4, pp. 290-301, 2019.
- [81] H. Weller, G. Tabor, H. Jassak and C. Fureby, "A tensorial approach to computational continuum mechanics using object-oriented techniques," *Computers in Physics*, vol. 12, no. 6, 1998.
- [82] National Aeronautics and Space Administration, "Navier-Stokes Equations," 19 July 2024. [Online]. Available: <https://www1.grc.nasa.gov/beginners-guide-to-aeronautics/navier-strokes-equation/>. [Accessed 2024].
- [83] D. C. Wilcox, *Turbulence Modelling for CFD Third Edition*, La Cañada California: DCW Industries, 2006.
- [84] G. Alfonsi, "Reynolds-Averaged Navier-Stokes Equations for Turbulence Modeling," *Applied Mechanics Reviews*, vol. 62, no. 4, 2009.
- [85] R. H. Bush, T. S. Chyczewski, K. Duraisamy, B. Eisfeld, C. L. Rumsey and B. R. Smith, "Recommendations for Future Efforts in RANS Modeling and Simulation," in *American Institute of Aeronautics and Astronautics - Modeling of Turbulence*, San Diego, California, 2019.
- [86] K. D. Squires, R. Friedrich, B. Geurts and O. Métais, "Detached-Eddy Simulation: Current Status and Perspectives," in *Direct and Large-Eddy Simulation*, Springer, Dordrecht, 2004, pp. 465-480.
- [87] S. Jamshed, "Large Eddy Simulation," in *Using HPC for Computational Fluid Dynamics*, Academic Press, 2015, pp. 81-100.

- [88] M. Mukaka, "A guide to appropriate use of Correlation coefficient in medical research," *Malawi Medical Journal*, vol. 24, no. 3, 2012.
- [89] Laerd Statistics, "Spearman's Rank-Order Correlation," 2024. [Online]. Available: <https://statistics.laerd.com/statistical-guides/spearmans-rank-order-correlation-statistical-guide.php>. [Accessed 14 September 2024].
- [90] Y. H. Chan, "Correlational Analysis," *Singapore Medical Journal*, vol. 44, no. 12, pp. 614-619, 2003.
- [91] M. S. A. K. YADAV, M. P. SINGH, P. Agarwal and S. Nigam, "A MATHEMATICAL MODEL FOR THE DISPERSION OF AIR POLLUTANTS IN LOW WIND CONDITIONS," *Atmospheric Environment*, vol. 30, no. 8, pp. 1209-1220, 1996.
- [92] A. K. Luhar, M. F. Hibberd and M. S. Borgas, "A skewed meandering plume model for concentration statistics in the convective boundary layer," *Atmospheric Environment*, vol. 34, no. 21, pp. 3599-3616, 2000.

Appendix A: Summary Table of Candidate Methane Quantification Technologies

Technology	Survey Type	Detection Level	Conc. Dimension	MDL	Precision	Applicability	Limitations	TRL
Ultraviolet Doppler Optical Absorption Spectroscopy	Fixed Location	Facility	Point Concentration (0D)	0.5-1 ppm-m	95%	LDAR programs (standalone or in combination with screening technologies)	Rain, snow, fog, and/or clouds reduce measurement abilities due to strong attenuation in the UV-Vis region.	9
OGI/QOGI Camera	Handheld	Component	Single Channel (1D)	0.44 m3/day	50-80%	LDAR programs (standalone or in combination with screening technologies)	Require a temperature difference between the emission plume and the local background (0.5 degrees to detect the gas; 3.0 degrees to quantify the mass flow rate). Must be between 1.5-4.6 m from the plume. Operating temperatures between -20 to	7+

							+50 degrees Celsius.	
Dual Frequency Comb Spectroscopy	Fixed Location	Facility	Single Channel (1D)	2.10 m ³ /day	within 0.222 kg/hr with absolute deviation of 27%	LDAR programs (standalone or in combination with screening technologies)	Precipitation reduces signal path.	4-7
Airborne TDLAS (Bridger)	Aerial	Facility /Site	Imaging (2D)	29.22 m ³ /day at 1 m/s wind 73.06 m ³ /day at 3 m/s wind 21.92 m ³ /day under ideal conditions	68%	Monitoring emissions from pipeline along ROW and remote/sparse arrangements of well sites. Screening technology for LDAR programs.	Standing water and snow absorb incident laser, leading to conservative emission estimates. Research is ongoing in developing a system that addresses this problem. Wind speed estimations limit accuracy of quantification (>3 m/s). A sufficient	9

							swath is required to meet the maximum efficiency of the technology. Drone applications are also less efficient than aircraft-mounted TDLAS.	
Multispectral IR Camera	Handheld	Component	Imaging (2D)	13,211 m ³ /day	1 K from -15°C to 150°C	LDAR programs (standalone or in combination with screening technologies)	Most MS cameras have warm filters, which disallows measurements of gases at near ambient temperatures. (MS cameras with cold filters are being developed.)	9
Spectrometry WAF-P (GHGSat)	Satellite	Facilities /Site	Imaging (2D)	36,529 m ³ /day in 3 m/s wind speeds	13-60%	Monitoring emissions from pipeline along ROW and remote/sparse arrangements of well sites. Screening	Requires clear skies for observations; can revisit a site every 2 weeks.	7+

						technology for LDAR programs.		
Hyperspectral IR Camera	Fixed Location	Component/Facility	Imaging (2D)	5.81 m ³ /day (3.4 m distance) 10.34 m ³ /day (5.9 m distance) at 4.5 m/s wind speed	up to 0.25 cm ⁻¹	LDAR programs (standalone or in combination with screening technologies)	Operating temperatures between -20 and +40 degrees celsius. Sensitive to high wind speeds. Measurement distance must be within 100 m of the sources.	7+
Spectrometry TROPOMI	Satellite	Site	Imaging (2D)	153,424 m ³ /day	0.60%	Monitoring emissions from pipeline along ROW and remote/sparse arrangements of well sites. Screening technology for LDAR programs.	Limited by the visibility of the atmosphere (i.e., cloud coverage). Solar zenith can also limit the ability for detection.	7+
Gas Filter Correlation Radiometer	Aerial, Satellite	Site	Single Channel (1D)	Satellite: 547.95 m ³ /day	Developing; theoretically within 1 ppm	Monitoring emissions from pipeline along ROW and remote/sparse	Requires clear skies for observations. Measurements	4/7

						arrangements of well sites. Screening technology for LDAR programs.	require a high solar zenith angle.	
Pellistor (Catalytic Bead)	Handheld, Fixed Location,	Component/Facility	Point Concentration (0D)	500 ppm - 5%	100%	LDAR programs (standalone or in combination with screening technologies)	Sensitive to high humidity, large temperature differentials, and environmental contaminants.	9
FTIR Spectroscopy	Vehicle, Aerial, Fixed Location	Facility	Single Channel (1D)	11.4 ppb	63-73%	Monitoring emissions from pipeline along ROW and remote/sparse arrangements of well sites. Screening technology for LDAR programs.	The survey time required for measurements is inversely proportional to the spectral resolution (distance travelled by the mirror in the interferometer).	9
Ultrasound Imaging	Handheld, Fixed Location	Component	Single Channel (1D)	8.5 g/hr	90%	LDAR programs (standalone or in combination with screening technologies)	Requires pressure drop to detect emissions.	4/7
MethaneSAT Spectrometry	Satellite	Site	Imaging (2D)	2 ppb over 1.5 km ²	Satellite observations typically fall between <1-5%	Monitoring emissions from pipeline along ROW and remote/sparse	Sensitive to low solar zenith and high wind speeds.	7+

					(not Methane SAT specific)	arrangements of well sites. Screening technology for LDAR programs.		
Metal Oxide Semiconductor (MOS)	Handheld, Fixed Location	Facility /Site	Point Concentration (OD)	2-10 ppm	Within 0.36 ppm	Continuous monitoring of emissions on sites. LDAR Programs.	Sensitive to high humidity, large temperature differentials, and environmental contaminants. Exposure to large concentrations may de-sensitize the sensor irreversibly.	9
Mass-Flow Meter	Handheld, Fixed Location	Component	Point Concentration (OD)	1.4 standard liters per minute	Within 2%	LDAR programs (standalone or in combination with screening technologies)	No longer manufactured. Highly dependent on daily calibration procedures.	9
Laser Absorption Spectroscopy - Cavity Output	Fixed Location, Handheld UAVs, Vehicle	Facility	Point Concentration (OD)	30 ppb	87%	Monitoring emissions from pipeline along ROW and remote/sparse arrangements of well sites. Screening technology for LDAR programs.	Moderate interference from moisture - dried samples preferred for optimal analysis.	7+

Laser Absorption Spectroscopy - Closed Path (Multi)	Fixed Location, UAVs, Vehicle	Facility	Point Concentration (0D)	100 ppb	within 79 ppb	Monitoring emissions from pipeline along ROW and remote/sparse arrangements of well sites. Screening technology for LDAR programs.	Require specific environmental requirements for measurement.	7+
Mass Spectrometry	Handheld, Fixed Location	Component	Single Channel (1D)	1 ppb	Within 3.4%	Continuous monitoring of emissions on sites. LDAR Programs.	Requires controlled environment (i.e., vacuum system).	9
Gas Chromatography	Handheld, Fixed Location	Component	Single Channel (1D)	1 ppb	Within 3% to 6% of true conc.	Continuous monitoring of emissions on sites. LDAR Programs.	Calibration and purge required prior to use. Calibration frequency varies based on instrument.	9

Printed Nanotube Sensors	Fixed Location	Facility	Point Concentration (0D)	5 ppm	Developing - Currently focused on detection rather	Continuous monitoring of emissions on sites. LDAR Programs.	Unknown	4/7
--------------------------	----------------	----------	--------------------------	-------	--	---	---------	-----

					than actual quantification			
Laser Absorption Spectroscopy - Open Path	Fixed point, UAVs, Vehicle	Facility	Single Channel (1D)	2 ppm*m	90-97%	Monitoring emissions from pipeline along ROW and remote/sparse arrangements of well sites. Screening technology for LDAR programs.	Measurement path length from 5 - 500 m. Wind limitations 2-10 m/s	7+
Etalon	Handheld, Vehicle, Fixed Location	Component	Single Channel (1D)	100 ppb	0.1 μm + 0.3 $\mu\text{m}/\text{m}$	Continuous monitoring of emissions on sites. LDAR Programs.	Highly dependent on surface reflectivity of the crystals; reflecting surfaces must be parallel and flat.	7+
Laser Absorption Spectroscopy - Closed Path (Single)	Fixed point, UAVs, Vehicle	Facility	Point Concentration (0D)	Relative to total pressure of the cell; 88 ppb	90-97%	Monitoring emissions from pipeline along ROW and remote/sparse arrangements of well sites. Screening technology for LDAR programs.	Require specific environmental requirements for measurement.	7+

Appendix B: QOGI Datasheets



FLIR GF300/GF320

Infrared Camera for Methane and VOC Detection

The FLIR GF300/GF320 is a revolutionary infrared camera capable of detecting Methane and Volatile Organic Compound (VOC) fugitive emissions from the production, transportation, and use of oil and natural gas. This camera can scan large areas and visualize potential gas leaks in real-time, so you can check thousands of components over the course of one survey. Designed with the user in mind, the GF300/GF320 is lightweight, offers both a viewfinder and LCD monitor, and has direct access to controls. Embedded GPS data helps in identifying the precise location of faults and leaks, for faster repairs.

Visualize Gas Emissions in Real-time

The FLIR GF300/GF320 is unbeatable at detecting gas emissions, with a High Sensitivity Mode that lets you visualize even the smallest leaks in real-time. Use this visual verification to pinpoint the exact source of the emissions and begin repairs immediately. In addition, the GF320 is capable of measuring temperatures up to 350 °C with ± 1 °C accuracy, allowing you to note temperature differentials and improve gas plume detection.

Increase Worker Safety

Surveys performed with GF300/GF320 cameras are nine-times faster than those performed with gas sniffers. They're also safer: optical gas imaging does not require close contact with components in order to detect gas. This reduces the risk of exposure to invisible and potentially harmful chemicals. In addition, the camera can scan areas of interest that are difficult to reach using conventional methods. The ergonomic design, with a bright LCD and articulated viewfinder, takes the strain out of a full day of surveys.

Stop Leaks, Save Money, Help the Environment

By fixing gas leaks, you can save your company thousands in lost gas and lost profits, while at the same time improving regulatory compliance and protecting the environment. The FLIR GF300/GF320 complies with all current regulations for Optical Gas Imaging (OGI). See our website for a full listing.

The GF300/GF320 detects the following gases:

Methanol	Methane	Benzene	Ethane	Propylene
Ethanol	Pentane	1-Pentene	Isoprene	Butane
Ethylbenzene	MEK	Toluene	Propane	Octane
Heptane	MIBK	Xylene	Ethylene	Hexane

www.flir.com



The World's **Sixth Sense**™

Specifications

Model		GF300 / GF320
Detector Type	FLIR Indium Antimonide (InSb)	
Spectral Range	3.2 – 3.4 μ m	
Resolution	320 x 240 pixels	
Detector Pitch	30 μ m	
NETD/Thermal Sensitivity	<15 mK @ +30°C (+86°F)	
Sensor Cooling	Stirling Microcooler (FLIR MC-3)	
Electronics / Imaging		
Image Modes	IR Image, visual image, high sensitivity mode (HSM)	
Frame Rate (Full Window)	60 Hz	
Dynamic Range	14-bit	
Video Recording / Streaming	Real-time non-radiometric recording: MPEG4/H.264 (up to 60 min./clip) to memory card Real-time non-radiometric streaming: RTP/MPEG4	
Visual Video	MPEG4 (25 min./clip) to memory card	
Visual Image	3.2 MP from integrated visible camera	
GPS	Location data stored with every image	
Camera Control	Remote camera control via USB	
Measurement		
Standard Temperature Range	-20°C to +350°C (-4°F to +662°F)	
Accuracy*	$\pm 1^\circ\text{C}$ ($\pm 1.8^\circ\text{F}$) for temperature range (0°C, to +100°C, +32°F to +212°F) or $\pm 2\%$ of reading for temperature range (>+100°C, >+212°F)	
Optics		
Camera f/number	f/1.5	
Available Fixed Lenses	14.5° (38 mm), 24° (23 mm)	
Focus	Automatic (one touch) or manual (electric or on the lens)	
Image Presentation		
On-Camera Display	Built-in widescreen, 4.3 in. LCD, 800 x 480 pixels	
Automatic Gain Control	Continuous/manual, linear, histogram	
Image Analysis*	10 spotmeters, 6 boxes with max./min./average, profile, delta temperatures, emissivity & measurement corrections	
Color palettes	Iron, Gray, Rainbow, Arctic, Lava, Rainbow HC	
Zoom	1-8x continuous, digital zoom	
General		
Operating Temperature Range	-20°C to +50°C (-4°F to +122°F)	
Storage Temperature Range	-30°C to +80°C (-22°F to +140°F)	
Encapsulation	IP 54 (IEC 60529)	
Bump / Vibration	25 g (IEC 60068-2-27) / 2 g (IEC 60068-2-6)	
Power	AC adapter 90-260 VAC, 50/60 Hz or 12 V from a vehicle	
Battery System	Rechargeable Li-ion battery	
Weight w/ Battery & Lens	1.94 kg (4.27 lbs)	
Size (L x W x H) w/ Lens	305 x 189 x 161 mm	
Mounting	Standard, 1/4"-20	

* GF320 model only



FLIR Systems, Inc.
9 Townsend West
Nashua, NH 03063
USA
PH: +1 866.477.3887

PORTLAND
Corporate Headquarters
FLIR Systems, Inc.
27700 SW Parkway Ave.
Wilsonville, OR 97070
USA
PH: +1 866.477.3887

EUROPE
FLIR Systems
Luxemburgstraat 2
2321 Meer
Belgium
PH: +32 (0) 3865 5100

www.flir.com/ogi
NASDAQ: FLIR

CANADA
FLIR Systems, Ltd.
920 Sheldon Court
Burlington, ON L7L 6L6
Canada
PH: +1 800.613.0507

CHINA
FLIR Systems Co., Ltd
Rm 1613-16, Tower II
Grand Central Plaza
138 Shatin Rural
Committee Road Shatin
New Territories
Hong Kong
PH: +852 2792 8955

LATIN AMERICA
FLIR Systems Brasil
Av. Antonio Bardella, 320
Sorocaba, SP 18052-852
Brasil
PH: +55 15 3238 7080

Equipment described herein may require US Government authorization for export purposes. Diversion contrary to US law is prohibited. Imagery for illustration purposes only. Specifications are subject to change without notice. ©2015 FLIR Systems, Inc. All rights reserved. (Updated 11/03/15)

www.flir.com



The World's Sixth Sense™

EyeCGas 2.0 Features

Concentration in real time using only OGI

EyeCGas 2.0 is the world's most sensitive and durable handheld OGI camera. Detecting over 400 VOCs, Methane and CO2. EyeCGas 2.0 is Intrinsically Safe and complies with the EPA's "Quad 0a" (0000a) regulations.

Using its wide range of features and functionalities, it enables surveyors to scan large areas quickly, efficiently and identify gas leaks while staying safe. Allowing for quick repairs and reducing revenue loss.

4 YEAR WARRANTY



STREAMING

Real-time video streaming and wireless images/videos sharing during inspections.

3RD PARTY ANALYZERS & LDAR SOFTWARE INTEGRATION

Connects to 3rd party analyzers (TVA 2020, RMLD, PHX42 and more). Display data on camera screen in real-time and store video files. Integrate your existing LDAR software (Guideware, CNTRL, Chateau, and more) for easy reporting.



REPLACEABLE LENS

- 30mm lens (standard)
- 75mm lens (for improved long-range detection)

REPLACEABLE FILTERS

Exclusive ability to change spectral filters:

- Default filter (Methane & over 400 VOC's)
- Higher Carbons filter (improved higher carbon and long range detection of VOC's)
- CO2 (carbon dioxide detection)



INTRINSICALLY SAFE

The most durable OGI camera by design. Water and dust protected IP65. Intrinsically safe, ATEX Zone2, IECEx, ANSI/ISA Class I, Div.2, CSA C22.2 Class I, Div. 2.

GLARE SHIELD

Enhances the image by x3 and avoids sun glare.



HIGHER SENSITIVITY

NEDT <10mK with proprietary image processing algorithm detecting 0.35g/hr (Methane). Certified to meet EPA 0000a requirements.

Built-in QUANTIFICATION

Quantify Methane and other VOCs in a simple and user-friendly interface, while seamlessly creating a report at the end of each inspection.



Opgal Optronic Industries Ltd. | +1 332 236 7048 | info@opgal.com | www.opgal.com

EyeCGas 2.0 TECHNICAL SPECIFICATIONS	
IMAGING PERFORMANCE	
THERMAL IMAGER	
THERMAL SENSITIVITY	<10mK@ 25°C
OPTICS	f/1.1; 18° with 30mm lens; Manual focus
DIGITAL ZOOM	x2,x4, x8 and x16 (only for visible camera)
DIGITAL VIDEO CAMERA	
EMBEDDED DIGITAL CAMERA	HD, fixed focus, for situational awareness
DETECTOR	
TYPE	Cooled High Sensitivity, 320 x 240 pixels
SPECTRAL RANGE	3 to 4.4µm
POWER INPUT	
POWER	12VDC; 13W
BATTERY LIFE	>4.5 hours continuous operation
PHYSICAL CHARACTERISTICS	
WEIGHT (WITH BATTERY AND LENS)	2.6kg (5.9 lbs)
COLOR	Grey and Black
SIZE IN (LXHXW)	9" x 4.3" x 5.1" (230 x 110 x 130) mm
INTERFACE	Tripod mounting UNC 1/4", rotation safe
THERMOGRAPHY	
MEASUREMENT	Spot temperature measurement
RANGE	-20°C to +350 °C
ACCURACY	At Least ± 1 °C (0 – 100 °C), ± 2% (> 100 °C), ± 2°C (-20 - 0 °C)
COLOR PALETTES	6 color palettes (Rainbow, Iron, ISO red, ISO green, Grey Scale and Vivid)
QUANTIFICATION	
GAS QUANTIFICATION	Image processing VOC gas quantification for desktop or handheld application (offline/online operation), Concentration measurement (ppm-m)
DISPLAY	
DISPLAY UNIT	3.5" Color LCD 640X480
ENVIRONMENTAL CONDITIONS	
OPERATING TEMPERATURE RANGE	-20°C to + 50°C
STORAGE TEMPERATURE RANGE	-40°C to + 70°C
TEMPERATURE AND HUMIDITY	IEC 60068-2-30 Temp. +25°C / +40°C Humidity 95% RH
EMC/ EMI	EN 60079-0:2012/A11:2013, EN 60079-11:2012, EN 60079-15:2010, IEC 60079-0:2017, IEC 60079-11:2011, IEC 60079-15:2010, IEC 60079-31:2013
VIBRATION	2.4 GRMS Random Vibration
WATER AND DUST PROTECTION	IP65
HALT - HIGH ACCELERATED LIFE TEST	Max temp: 55°C, Min temp: -20°C
SAFETY	EN60950-1:2006
HAZARDOUS LOCATIONS SAFE	CSA C22.2 No. 213-M1987, Non-Incendive Electrical Equipment for Use in Class I, Division 2, ANSI/ISA-12.12.01 - Class I and II, Division 2, and Class III, ATEX intrinsically safe for Zone 2 ratings as: Ex II 3 GD; Ex ic nA nC IIC T6 Gc; Ex ic tc IIIC T85°C DC
ENVIRONMENTAL CONDITIONS WHEN PACKED IN CARRYING CASE	
FREE FALL (DROP) TEST	ASTM-D 4169-06 Schedule A
LOOSE CARGO VIBRATION TEST	ASTM-D 4169-08 Schedule F Test method D999
VIBRATION	ASTM-D 4169-08 Schedule F Test method D999
GAS LEAK DETECTION PERFORMANCE	
OPERATION FEATURES	Auto and Enhanced Modes
WITH SPECTRAL FILTER OF 3.2µM TO 3.4µM FOR VOCs GASES DETECTION	400+ compounds such as: Methane, Acetic acid, Benzene, Butadiene, Butene, Butane, Dimethyl-Benzene, Ethane, Ethylene, Ethyl benzene, Ethylene oxide, Hexane, Heptane, Isobutylene, Isopropyl alcohol, Isoprene, Methanol, MEK Methyl Ethyl Ketone, Octane, Pentene, Propane, Propanal
DIGITAL VIDEO AND AUDIO RECORDING	
VIDEO AND AUDIO RECORDING	Digital video recorder build-in generates a .ts format video on all modes.
SNAPSHOT CAPABILITIES	Snapshot command generates a .jpg file on any of the available modes
STORAGE	Up to 20 hours and more of video storage over a 64GB solid state memory
COMMUNICATION INTERFACES	
USB	Data transfer, video streaming and video images file transfer
Wi-Fi	2.4 GHz for video streaming and file transfer
Bluetooth	Bluetooth 4.2 with other devices: RMLD, TVA2020 ,LDAR software etc...
GPS	Built in or external
SUPPLIED ACCESSORIES	
Batteries (2), Battery Charger, USB Cable, Neck strap, Glare Shield, Carrying Case, Cleaning Kit.	

Appendix C: Aerial LWIR Datasheet



Hyper-Cam Module Mini

A NEW GENERATION OF COMPACT AIRBORNE HYPERSPECTRAL IMAGING SYSTEMS.

The Hyper-Cam Airborne Mini paves the way towards a striking revolution in infrared hyperspectral imaging. This lightweight FTIR sensor is designed for use in compact aerial platforms without compromising measurement performance. The easy and flexible operation makes the Hyper-Cam Airborne Mini a versatile tool, well-suited to meet the requirements of the most demanding applications, including ground target signature collection, mineral mapping and gas detection and identification.

KEY BENEFITS

COMPACT & LIGHTWEIGHT:

Easy to install with a total weight of only 24 kg and a volume of less than 2 cubic feet.

SELECTABLE SPECTRAL RESOLUTION:

The Hyper-Cam Airborne Mini offers the best spectral resolution available, and is user-selectable up to 0.5 cm⁻¹. This, coupled with swappable fore-optics, optimizes ground coverage.

HIGH SPATIAL RESOLUTION:

The Hyper-Cam Airborne Mini provides the highest spatial resolution on the market. It uses the latest 320 x 256-pixel cooled SLS detector to ensure excellent 2D image quality.

HIGH TEMPORAL RESOLUTION:

Hyperspectral data are recorded as a function of time allowing characterization of time-dependent events like gas cloud dispersion and combustion. Measurement time varies with acquisition parameters and allows for the fastest recording of dynamic events.

EXTREME FLEXIBILITY:

The Hyper-Cam Airborne Mini comes with a separate optical head and processing unit, and a powerful software suite for the commands, controls and processing of data.

Also offered are an optional software development kit (SDK) as well as an automatic gas detection/identification/quantification plug-in.

TYPICAL USES

- Gas detection, identification and quantification.
- Stack emission monitoring.
- Airborne mineral mapping.
- Airborne tracking of dangerous chemicals.
- Ground target IR signature measurement.



SPECIFICATIONS

SPECIFICATIONS	
OPERATIONAL MODES	Mapping, Targeting
SPECTRAL RANGE	7.4 - 11.8 μm
PIXEL FIELD OF VIEW	750 μrad
TOTAL ANGULAR RANGE	13.5 x 10.9°
OPTICAL HEAD INCLUSIONS	Image Motion Compensation Mirror Boresighted Visible Camera GPS/INS+ Platform
POWER CONSUMPTION	< 260 W
HEAD & PLATFORM SIZE	28 x 35 x 38 cm
CONTROL BOX SIZE	23 x 21 x 18 cm
HEAD & PLATFORM WEIGHT	< 20 kg
CONTROL BOX WEIGHT	< 4 kg
TYPICAL NESR	< 35 nW/(cm ² sr cm ⁻¹)



REVEAL SOFTWARE SUITE

- Efficient mission planning.
- Comprehensive commands & acquisition.
- Intuitive post-processing, calibration, geo-correction & mosaicing.
- Automatic image stitching and map generation after mission.
- Real-time gas detection, identification and quantification (optional plug-in).



Gas emission from oil plant.

Please note that these specifications are subject to change.

FOR MORE INFORMATION | TELOPS.COM

TELOPS HEADQUARTERS
contact@telops.com
 Tel.: +1 (418) 864-7808

TELOPS USA
vince.morton@telops.com
 Tel.: +1 (831) 419-7507

TELOPS FRANCE
eric.guyot@telops.com
 Tel.: +33 1 70 27 71 34

TELOPS CHINA
zhaoyongg@vip.sina.com
 Tel.: +86 13801185178

Appendix D: Boreal Gasfinder3-VB Datasheet

LASER BASED - VEHICLE BASED GAS DETECTOR ISA DATA SHEET			
General	1	Manufacturer	Boreal Laser Inc.
	2	Analyzer Model No.	GasFinder3-VB (Vehicle Based) Assembly (e.g. BL-GF3-VB- _- _- _-)
	3	Warranty Period	10 years on Laser (Light Source) and 3 years Full Warranty
Detector Specifications	4	Detection/Operating Principle	Tunable Diode Laser Absorption Spectroscopy (TDLAS)
	5	Sensor Type	One (1) Semiconductor Diode Laser which emits Laser Light in the Near Infrared (NIR)
	6	Eye Safety	Class 1 AEL under IEC 60825-1
	7	Function	Detects/monitors free gaseous molecules of one (1) specific target gas
	8	Calibration	Factory calibrated with no requirement for periodic/inherent calibration
	9	Field Calibration	None Required or Available
	10	Automatic Validation	Internal Reference Cell (Interrogated once a minute)
	11	User Function Testing	External Response Cell to "bump", "test" or "challenge" (Optional Accessory)
	12	Response Time	One sample per second
	13	Recovery Time	Instantaneous (Each sample is Independent of the last)
	14	Accuracy	±2% of Reading
	15	Internal Temperature Compensation	Dynamic (Piezo Resistive) or Manual Entry: -55°C to +150°C (-67°F to +302°F)
	16	Internal Pressure Compensation	Dynamic (MEMS) or Manual Entry: 50 to 200 KPaA (7.25 to 29 PSIA)
	17	Drift	±0.1% over operating temperature and pressure ratings
Enclosure Specifications	18	Warm-up / Start-up Time	2 Minutes
	19	User Intervention on Start-up	None Required
	20	Active Measurement Path - Temperature	-55 to +300°C (-67 to 600°F)
	21	Active Measurement Path - Humidity	0-100% RH (Non-Condensing)
	22	Active Measurement Path - Pressure	50 to 200 KPaA (7.25 to 29 PSIA)
	23	Fault Diagnostics	Fail Safe Operation with Status Codes visible via HMI Service Module, Interface and Logfiles
	24	Internal Data Logging	User has access to 20 years worth of storage capacity via USB Stick
	25	Obscuration / Beam Block	Operates down to 97% Obscuration (40x Turndown)
	26	Solar Blind	No False Positives from Solar Interference
	Power Requirements	27	Area Classification
28		Operating Temperature Range	-55 to +65°C (-67 to 149°F)
29		Storage Temperature	-55 to +65°C (-67 to 149°F)
30		Ingress Protection	Weather Tight
31		Enclosure Material	Potted Aluminium
32		Enclosure Dimensions (LxWxH)	260 x 200 x 160 mm (10.2 x 7.9 x 6.3 in)
33		Enclosure Weight	5.0 kg (11.0 lbs)
34		Cable Glands/Fittings	Military Connectors for Power and Communication
35		Power/Communication Terminals	12 or 24 VDC Power Supplies with Military Connector for Power Connection
Analog Output	36	Input Voltage	24 VDC (24-30 VDC)
	37	Power Consumption	20 Watts under Normal Operation
	38	In-Rush Current	2.5A for 100ms
	39	Recommended External Fuse	4A Fast Blow Fuse
	40	Number of Analog Loops	One (1) HART 7 over Analog Loop
	41	Supply of Loop Power	Active/Source (Device Powered Loop)
	42	Configurable Analog Output Options	Concentration (ppm-m, ppm, or mg/Nm ³), Light Level (Rx), & R2 Confidence Factor (R2)
	43	Analog Range Settings	User Programmable via HMI Touchscreen
MODBUS	44	Analog Load Impedance	1,000 ohms (4 Devices)
	45	Analog Range	0-20 mA
	46	Low Light Alarm (Beam Block)	2.7 mA
Interface	47	General System Fault	3.6 mA
	48	MODBUS	RS-485 - See Address Register Map for more information
Lo-Range Methane (CH4L)	49	Commonly Used Registers	Concentration (ppm-m) - 41001, Light Level (Rx) - 41101, & Confidence Factor (R2) - 41061
	50	HMI Touchscreen	Full Interface Capabilities: Configuration, Alignment, Access to Logfiles, and Upload Firmware
	51	Minimum Detectable Limit (MDL)	0.66 ppm
	52	Sensitivity	0.16 ppm
	53	Full Scale	2,833 ppm
Vehicle Based (VB) Measurement Cell	54	Lowest Actionable Concentration	1.32 ppm (2x MDL)
	55	Maximum Recommended Cable Length	20 m (60 ft)
	56	Optical Configuration	Transceiver and Retro-Reflector (Mono-Static) with Three (3) Multipass Configuration
	57	Measurement Cell Dimensions	1,300 x 300 x 200 mm (51.2 x 11.8 x 9.1 in)
Alignment Mount	58	Measurement Cell Weight	14.8 kg (32.5 lbs)
	59	Beam Divergence	16mm (5/8") @ 0.5m (1.6ft) = (32 milliradian x path length (m) = laser dot size (mm))
	60	Window Material	Lexan, Mylar, or Teflon
	61	Truck Mount: Headache Rack	Headache Rack Mounting bracket
	62	Generic Mounting Bracket	Tubular Mounting Bracket
Recommended Accessories	63	No Mounts Required	No Mounts Included
	64	Replacement Filter	BL-RCAB
Latest Revision	65	Alignment Kit	BL-OAK-VB
	66		1/07/22

Appendix E: Release notebook from the April 2022 field measurement campaign

Date	Start time	Release Rate m³/d (kg/hr)	Equipment
20-Apr	15:28	340 (10)	Stack
20-Apr	15:33	340 (10)	Stack
20-Apr	15:33	340 (10)	Stack
20-Apr	15:37	340 (10)	Stack
20-Apr	15:39	340 (10)	Stack
20-Apr	15:43	340 (10)	Stack
20-Apr	15:46	340 (10)	Stack
20-Apr	15:47	340 (10)	Stack
20-Apr	15:49	340 (10)	Stack

20- Apr	15:51	340 (10)	Stack
20- Apr	15:52	340 (10)	Stack
20- Apr	16:05	0 (0)	Stack
20- Apr	16:05	0 (0)	Stack
20- Apr	16:19	170 (5)	Stack
20- Apr	16:19	170 (5)	Stack
20- Apr	16:23	170 (5)	Stack
20- Apr	16:23	170 (5)	Stack
20- Apr	16:26	170 (5)	Stack
20- Apr	16:28	170 (5)	Stack
20- Apr	16:35	170 (5)	Stack

20- Apr	16:40	170 (5)	Stack
20- Apr	16:41	170 (5)	Stack
20- Apr	16:45	170 (5)	Stack
20- Apr	16:45	170 (5)	Stack
20- Apr	16:57	83.6 (2.46)	Stack
20- Apr	16:57	83.6 (2.46)	Stack
20- Apr	17:00	83.6 (2.46)	Stack
20- Apr	17:02	83.6 (2.46)	Stack
20- Apr	17:03	83.6 (2.46)	Stack
20- Apr	17:09	83.6 (2.46)	Stack
20- Apr	17:12	83.6 (2.46)	Stack

20- Apr	17:12	83.6 (2.46)	Stack
20- Apr	17:17	83.6 (2.46)	Stack
20- Apr	17:18	83.6 (2.46)	Stack
20- Apr	17:22	83.6 (2.46)	Stack
20- Apr	17:22	83.6 (2.46)	Stack
20- Apr	17:25	83.6 (2.46)	Stack
20- Apr	17:32	34 (1)	Stack
20- Apr	17:38	34 (1)	Stack
20- Apr	17:40	34 (1)	Stack
20- Apr	17:42	34 (1)	Stack
20- Apr	17:46	34 (1)	Stack

20- Apr	17:48	34 (1)	Stack
20- Apr	17:53	34 (1)	Stack
20- Apr	17:55	34 (1)	Stack
20- Apr	17:58	34 (1)	Stack
20- Apr	18:08	0 (0)	Stack
20- Apr	18:08	0 (0)	Stack
20- Apr	18:21	34 (1)	Stack
20- Apr	18:21	34 (1)	Stack
20- Apr	18:25	34 (1)	Stack
20- Apr	18:30	340 (10)	Stack
20- Apr	18:30	340 (10)	Stack

20- Apr	18:32	340 (10)	Stack
20- Apr	18:35	340 (10)	Stack
20- Apr	18:34	340 (10)	Stack
20- Apr	18:37	340 (10)	Stack
20- Apr	18:42	340 (10)	Stack
20- Apr	18:46	340 (10)	Stack
20- Apr	18:47	340 (10)	Stack
20- Apr	18:50	340 (10)	Stack
20- Apr	18:52	340 (10)	Stack
20- Apr	18:53	340 (10)	Stack
20- Apr	18:57	340 (10)	Stack

20- Apr	19:10	83.6 (2.46)	Stack
20- Apr	19:10	83.6 (2.46)	Stack
20- Apr	19:13	83.6 (2.46)	Stack
20- Apr	19:14	83.6 (2.46)	Stack
20- Apr	19:16	83.6 (2.46)	Stack
20- Apr	19:18	83.6 (2.46)	Stack
20- Apr	19:18	83.6 (2.46)	Stack
20- Apr	19:23	83.6 (2.46)	Stack
21- Apr	10:07	34 (1)	Tank
21- Apr	10:08:54	34 (1)	Tank
21- Apr	10:15:25	34 (1)	Tank

21- Apr	10:16	34 (1)	Tank
21- Apr	10:18:40	34 (1)	Tank
21- Apr	10:19	34 (1)	Tank
21- Apr	10:21:42	34 (1)	Tank
21- Apr	10:24:21	34 (1)	Tank
21- Apr	10:27	34 (1)	Tank
21- Apr	10:28:11	34 (1)	Tank
21- Apr	10:31:25	34 (1)	Tank
21- Apr	10:34:10	34 (1)	Tank
21- Apr	10:43:56	34 (1)	Tank
21- Apr	10:55:54	83.6 (2.46)	Tank

21- Apr	10:55:30	83.6 (2.46)	Tank
21- Apr	10:58:26	83.6 (2.46)	Tank
21- Apr	11:00:05	83.6 (2.46)	Tank
21- Apr	11:00:35	83.6 (2.46)	Tank
21- Apr	11:02:41	83.6 (2.46)	Tank
21- Apr	11:05	83.6 (2.46)	Tank
21- Apr	11:11:23	83.6 (2.46)	Tank
21- Apr	11:13:41	83.6 (2.46)	Tank
21- Apr	11:16:40	83.6 (2.46)	Tank
21- Apr	11:19:32	83.6 (2.46)	Tank
21- Apr	11:21:11	83.6 (2.46)	Tank

21- Apr	11:23:41	83.6 (2.46)	Tank
21- Apr	11:25:24	83.6 (2.46)	Tank
21- Apr	11:28:18	83.6 (2.46)	Tank
21- Apr	11:29:31	83.6 (2.46)	Tank
21- Apr	11:30:20	83.6 (2.46)	Tank
21- Apr	11:31:56	83.6 (2.46)	Tank
21- Apr	11:41:58	0 (0)	Tank
21- Apr	11:43:25	0 (0)	Tank
21- Apr	11:45:30	0 (0)	Tank
21- Apr	11:51:45	340 (10)	Tank
21- Apr	11:49:30	340 (10)	Tank

21- Apr	11:53:30	340 (10)	Tank
21- Apr	11:54:56	340 (10)	Tank
21- Apr	11:57:35	340 (10)	Tank
21- Apr	11:58:40	340 (10)	Tank
21- Apr	11:57:40	340 (10)	Tank
21- Apr	12:01:20	340 (10)	Tank
21- Apr	12:02:45	340 (10)	Tank
21- Apr	12:05:11	340 (10)	Tank
21- Apr	12:07:01	340 (10)	Tank
21- Apr	12:09:40	340 (10)	Tank
21- Apr	12:10:59	340 (10)	Tank

21- Apr	12:13:32	340 (10)	Tank
21- Apr	13:31:30	170 (5)	Tank
21- Apr	13:31:15	170 (5)	Tank
21- Apr	13:35:04	170 (5)	Tank
21- Apr	13:35:45	170 (5)	Tank
21- Apr	13:38:00	170 (5)	Tank
21- Apr	13:37:06	170 (5)	Tank
21- Apr	13:39:30	170 (5)	Tank
21- Apr	13:39:26	170 (5)	Tank
21- Apr	13:41:11	170 (5)	Tank
21- Apr	13:41:50	170 (5)	Tank

21- Apr	13:43:52	170 (5)	Tank
21- Apr	13:45:13	170 (5)	Tank
21- Apr	13:47:41	170 (5)	Tank
21- Apr	13:49:06	170 (5)	Tank
21- Apr	13:51:41	170 (5)	Tank
21- Apr	13:53:06	170 (5)	Tank
21- Apr	13:55:21	170 (5)	Tank
21- Apr	13:57:11	170 (5)	Tank
21- Apr	13:49	170 (5)	Tank
21- Apr	13:51	170 (5)	Tank
21- Apr	13:53	170 (5)	Tank

21- Apr	13:55	170 (5)	Tank
21- Apr	13:57	170 (5)	Tank
21- Apr	14:06:40	340 (10)	Tank
21- Apr	14:08:23	340 (10)	Tank
21- Apr	14:07:56	340 (10)	Tank
21- Apr	14:10:21	340 (10)	Tank
21- Apr	14:10:45	340 (10)	Tank
21- Apr	14:11:46	340 (10)	Tank
21- Apr	14:14:30	340 (10)	Tank
21- Apr	14:15:00	340 (10)	Tank
21- Apr	14:15:56	340 (10)	Tank

21- Apr	14:17:01	340 (10)	Tank
21- Apr	15:21:20	680 (20)	Stack
21- Apr	15:24:00	680 (20)	Stack
21- Apr	15:23:46	680 (20)	Stack
21- Apr	15:26:26	680 (20)	Stack
21- Apr	15:27:30	680 (20)	Stack
21- Apr	15:28:59	680 (20)	Stack
21- Apr	15:29:25	680 (20)	Stack
21- Apr	15:32:40	680 (20)	Stack
21- Apr	15:32:30	680 (20)	Stack
21- Apr	15:34:58	680 (20)	Stack

21- Apr	15:37:35	680 (20)	Stack
21- Apr	15:40:49	680 (20)	Stack
21- Apr	15:41	680 (20)	Stack
21- Apr	15:43:30	680 (20)	Stack
21- Apr	15:46:20	680 (20)	Stack
21- Apr	15:49:50	680 (20)	Stack
21- Apr	15:52:50	680 (20)	Stack
21- Apr	15:53:24	680 (20)	Stack
21- Apr	15:54:25	680 (20)	Stack
21- Apr	15:56:11	680 (20)	Stack
21- Apr	15:56:50	680 (20)	Stack

21- Apr	15:58:58	680 (20)	Stack
21- Apr	16:00:01	680 (20)	Stack
21- Apr	16:14:45	1020 (30)	Stack
21- Apr	16:15:30	1020 (30)	Stack
21- Apr	16:17:21	1020 (30)	Stack
21- Apr	16:18:05	1020 (30)	Stack
21- Apr	16:20:01	1020 (30)	Stack
21- Apr	16:23:18	1020 (30)	Stack
21- Apr	16:31:20	1020 (30)	Stack
21- Apr	16:31:50	1020 (30)	Stack
21- Apr	16:34:11	1020 (30)	Stack

21- Apr	16:36:07	1020 (30)	Stack
21- Apr	16:36:36	1020 (30)	Stack
21- Apr	16:40:15	1020 (30)	Stack
21- Apr	16:39:31	1020 (30)	Stack
21- Apr	16:42:30	1020 (30)	Stack
21- Apr	16:42:51	1020 (30)	Stack
21- Apr	16:45:32	1020 (30)	Stack
21- Apr	16:46:10	1020 (30)	Stack
21- Apr	16:48:16	1020 (30)	Stack
21- Apr	16:51:08	1020 (30)	Stack
21- Apr	16:51:40	1020 (30)	Stack

21- Apr	16:54:30	1020 (30)	Stack
22- Apr	09:37:12	0 (0)	Stack
22- Apr	09:39:12	0 (0)	Stack
22- Apr	09:47:05	0 (0)	Stack
22- Apr	09:54:10	17 (0.5)	Stack
22- Apr	09:56:02	17 (0.5)	Stack
22- Apr	09:57:21	17 (0.5)	Stack
22- Apr	09:59:15	17 (0.5)	Stack
22- Apr	10:00:51	17 (0.5)	Stack
22- Apr	10:02:55	17 (0.5)	Stack
22- Apr	10:03:52	17 (0.5)	Stack

22- Apr	10:05:10	17 (0.5)	Stack
22- Apr	10:07:15	17 (0.5)	Stack
22- Apr	10:07:16	17 (0.5)	Stack
22- Apr	10:10:05	17 (0.5)	Stack
22- Apr	10:10:21	17 (0.5)	Stack
22- Apr	10:13:36	17 (0.5)	Stack
22- Apr	10:14:09	17 (0.5)	Stack
22- Apr	10:16:50	17 (0.5)	Stack
22- Apr	10:16:59	17 (0.5)	Stack
22- Apr	10:18:41	17 (0.5)	Stack
22- Apr	10:20:13	17 (0.5)	Stack

22- Apr	10:21:54	17 (0.5)	Stack
22- Apr	10:35:07	8.5 (0.25)	Stack
22- Apr	10:34:29	8.5 (0.25)	Stack
22- Apr	10:37:22	8.5 (0.25)	Stack
22- Apr	10:40:33	8.5 (0.25)	Stack
22- Apr	10:40:33	8.5 (0.25)	Stack
22- Apr	10:43:39	8.5 (0.25)	Stack
22- Apr	10:44:07	8.5 (0.25)	Stack
22- Apr	10:46:53	8.5 (0.25)	Stack
22- Apr	10:47:37	8.5 (0.25)	Stack
22- Apr	10:49:59	8.5 (0.25)	Stack

22- Apr	10:51:08	8.5 (0.25)	Stack
22- Apr	10:53:03	8.5 (0.25)	Stack
22- Apr	10:55:45	8.5 (0.25)	Stack
22- Apr	10:56:41	8.5 (0.25)	Stack
22- Apr	11:00:35	8.5 (0.25)	Stack
22- Apr	11:03:11	8.5 (0.25)	Stack
22- Apr	11:03:54	8.5 (0.25)	Stack
22- Apr	11:06:21	8.5 (0.25)	Stack
22- Apr	11:06:56	8.5 (0.25)	Stack
22- Apr	11:09:00	8.5 (0.25)	Stack
22- Apr	11:22:01	170 (5)	Stack

22- Apr	11:23:04	170 (5)	Stack
22- Apr	11:25:58	170 (5)	Stack
22- Apr	11:27:37	170 (5)	Stack
22- Apr	11:29:08	170 (5)	Stack
22- Apr	11:30:30	170 (5)	Stack
22- Apr	11:32:16	170 (5)	Stack
22- Apr	11:33:20	170 (5)	Stack
22- Apr	11:35:51	170 (5)	Stack
22- Apr	11:36:10	170 (5)	Stack
22- Apr	11:49:15	83.6 (2.46)	Stack
22- Apr	11:50:29	83.6 (2.46)	Stack

22- Apr	11:52:11	83.6 (2.46)	Stack
22- Apr	11:53:20	83.6 (2.46)	Stack
22- Apr	11:55:21	83.6 (2.46)	Stack
22- Apr	11:57:32	83.6 (2.46)	Stack
22- Apr	11:58:33	83.6 (2.46)	Stack
22- Apr	11:59:35	83.6 (2.46)	Stack
22- Apr	12:09:37	34 (1)	Stack
22- Apr	12:10:25	34 (1)	Stack
22- Apr	12:13:11	34 (1)	Stack
22- Apr	12:31:16	34 (1)	Stack
22- Apr	12:30:37	34 (1)	Stack

22- Apr	12:34:11	34 (1)	Stack
22- Apr	12:37:21	34 (1)	Stack
22- Apr	12:40:21	34 (1)	Stack
22- Apr	12:41:01	34 (1)	Stack
22- Apr	12:43:21	34 (1)	Stack
22- Apr	12:45:30	34 (1)	Stack
22- Apr	12:46:35	34 (1)	Stack
22- Apr	12:47:57	34 (1)	Stack
22- Apr	12:52:40	34 (1)	Stack
22- Apr	12:52:40	34 (1)	Stack
22- Apr	12:55:21	34 (1)	Stack

22- Apr	12:55:00	34 (1)	Stack
23- Apr	12:02	170 (5)	Stack
23- Apr	12:13	170 (5)	Stack
23- Apr	12:32	170 (5)	Stack
23- Apr	12:48	170 (5)	Stack
23- Apr	13:31	1360 (40)	Stack
23- Apr	13:37	1360 (40)	Stack
23- Apr	13:45	1360 (40)	Stack
23- Apr	13:58	1360 (40)	Stack
23- Apr	14:07	1360 (40)	Stack
23- Apr	14:13	1360 (40)	Stack

23- Apr	14:18	1360 (40)	Stack
23- Apr	14:24	1360 (40)	Stack
23- Apr	14:29	680 (20)	Stack
23- Apr	14:34	680 (20)	Stack
23- Apr	14:38	680 (20)	Stack
23- Apr	14:47	680 (20)	Stack
23- Apr	14:52	680 (20)	Stack
23- Apr	14:57	680 (20)	Stack
23- Apr	15:02	680 (20)	Stack
23- Apr	15:08	680 (20)	Stack
23- Apr	15:13	680 (20)	Stack

23- Apr	15:18	680 (20)	Stack
23- Apr	15:29	1700 (50)	Stack
23- Apr	15:34	1700 (50)	Stack
23- Apr	15:38	1700 (50)	Stack
23- Apr	15:44	1700 (50)	Stack
23- Apr	15:48	1700 (50)	Stack
23- Apr	15:55	1700 (50)	Stack
23- Apr	16:00	1700 (50)	Stack
23- Apr	16:06	1700 (50)	Stack
23- Apr	16:10	1700 (50)	Stack
23- Apr	16:16	1700 (50)	Stack

23- Apr	16:21	1700 (50)	Stack
23- Apr	16:26	1020 (30)	Stack
23- Apr	16:30	0 (0)	Stack
23- Apr	16:36	1020 (30)	Stack
23- Apr	16:40	1020 (30)	Stack
23- Apr	16:45	1020 (30)	Stack
23- Apr	16:50	1020 (30)	Stack
23- Apr	16:55	1020 (30)	Stack
23- Apr	16:59	1020 (30)	Stack
23- Apr	17:04	1020 (30)	Stack
23- Apr	17:09	1020 (30)	Stack

23- Apr	17:14	1020 (30)	Stack
23- Apr	17:18	1360 (40)	Stack
23- Apr	17:23	1360 (40)	Stack
23- Apr	17:27	2040 (60)	Stack
23- Apr	17:33	2040 (60)	Stack
24- Apr	11:20	680 (20)	Unlit Flare
24- Apr	11:25	680 (20)	Unlit Flare
24- Apr	11:30	680 (20)	Unlit Flare
24- Apr	11:36	680 (20)	Unlit Flare
24- Apr	11:42	680 (20)	Unlit Flare
24- Apr	11:48	680 (20)	Unlit Flare

24- Apr	11:53	680 (20)	Unlit Flare
24- Apr	11:59	680 (20)	Unlit Flare
24- Apr	12:04	680 (20)	Unlit Flare
24- Apr	12:09	680 (20)	Unlit Flare
24- Apr	12:14	1700 (50)	Unlit Flare
24- Apr	12:19	1700 (50)	Unlit Flare
24- Apr	12:23	1700 (50)	Unlit Flare
24- Apr	12:28	1700 (50)	Unlit Flare
24- Apr	12:33	1700 (50)	Unlit Flare
24- Apr	12:38	1700 (50)	Unlit Flare
24- Apr	12:42	1700 (50)	Unlit Flare

24- Apr	12:47	1700 (50)	Unlit Flare
24- Apr	12:51	1700 (50)	Unlit Flare
24- Apr	12:55	1700 (50)	Unlit Flare
24- Apr	13:00	1360 (40)	Unlit Flare
24- Apr	13:05	1360 (40)	Unlit Flare
24- Apr	13:10	1360 (40)	Unlit Flare
24- Apr	13:14	1360 (40)	Unlit Flare
24- Apr	13:19	1360 (40)	Unlit Flare
24- Apr	13:24	340 (10)	Unlit Flare
24- Apr	13:29	340 (10)	Unlit Flare
24- Apr	13:35	340 (10)	Unlit Flare

24- Apr	13:44	0 (0)	Unlit Flare
24- Apr	13:49	1020 (30)	Unlit Flare
24- Apr	13:54	1020 (30)	Unlit Flare
24- Apr	14:04	1020 (30)	Unlit Flare
24- Apr	14:09	1020 (30)	Unlit Flare
24- Apr	14:14	1020 (30)	Unlit Flare
24- Apr	14:20	1020 (30)	Unlit Flare
24- Apr	14:26	2720 (80)	Unlit Flare

Appendix F: Release notebook from the September 2022 field measurement campaign

Release Type	Time Start	Release Rate (m³/day)	Wind Speed (m/s)	Wind Direction	Pressure (kPa)	Temp (°C) from mass-flow controller
SEPTEMBER 25TH						
Large stack	10:00	0	1	SW	N/A	N/A
Large stack	10:20	340	1.5	S	207.9	21.29
Large stack	10:36	1200	1	SW	380.6	22.71
Large stack	10:51	1690	1.5	WSW	380.9	17.28
Large stack	11:07	710	1.5	W	410.2	12.52
Large stack	11:20	1350	1.5	W	389.2	19.66
Large stack	11:29	2720	1.5	W	317.7	16.6
Short stack 1.7m	11:38	2720	2.5	W	315.9	4.88
Short stack 1.7m	11:51	0	1	W	0	0

Short stack 1.7m	11:54	710	2.5	W	406.8	14.01
Short stack 1.7m	12:03	1200	2.5	WNW	387.6	21.14
Short stack 1.7m	12:20	340	2.5	NW	421	23.58
Short stack 1.7m	12:38	0	1	WSW	0	0
Short stack 1.7m	12:44	1690	1.5	W	290.5	30.18
Short stack 1.7m	13:08	1350	2.5	SW	356.4	19.26
Large stack	13:12	0	1.5	SW	N/A	N/A
Large stack	13:22	1350	1.5	SSW	338.3	28.6
Large stack	13:31	170	2.5	SW	421.5	28.52
Large stack	13:39	1200	3	SW	337.5	30.66
SEPTEMBER 26TH						
1.7m Stack	09:31	170	0	NA	307	21.41
1.7m Stack	10:02	51	0	NA	285	26.62

1.7m Stack	10:23	710	1	SW	282.4	25.81
1.7m Stack	10:52	8.5	0	NA	228	28.77
1.7m Stack	11:05	0	1	SW	0	0
1.7m Stack	11:21	51	1.5	E	243.8	30.2
1.7m Stack	11:31	710	1.5	SSE	227.5	32.18
1.7m Stack	11:42	8.5	1.5	E	377.2	30.53
1.7m Stack	11:53	51	1.6	SE	320.7	31.8
1.7m Stack	12:04	710	1.5	SE	262.7	32.98
1.7m Stack	12:12	8.5	2	SE	347	31.57
1.7m Stack	12:24	0	1.4	S	0	0
1.7m Stack	12:33	710	2	S	334.9	33.03
1.7m Stack	12:52	710	2	S	334.9	33.03

1.7m Stack	12:59	51	1.5	SE	427.6	33.9
1.7m Stack	13:18	8.5	2.5	S	409.7	34.72
Flare stack	13:39	1690	3.5	S	397.7	33.35
Flare stack	14:09	710	2.5	SW	435.4	25.31
Flare stack	14:23	1200	3.5	SW	423.6	31.28
Flare stack	14:37	1350	3	SW	413.7	30.15
Flare stack	14:50	340	3	SW	420.7	30.57
Small stack (3 piece - 4.84m)	15:06	0	3	SW	0	0
Small stack (3 piece - 4.84m)	15:10	170	3	SW	397.2	32.65
Small stack (3	15:31	1690	2	SSW	234.5	34.83

piece - 4.84m)						
Small stack (3 piece - 4.84m)	15:42	710	2	S	407.8	29.4
Small stack (3 piece - 4.84m)	15:51	1200	2.5	S	380.9	30.99
Small stack (3 piece - 4.84m)	16:02	1350	1.4	S	377.8	30.37
Small stack (3 piece - 4.84m)	16:13	340	2	S	420.7	29.34
Small stack (3 piece - 4.84m)	16:24	0	2.6	SSW	445.6	31.92
Small stack (3	16:32	8.5	1.7	S	432.0 31.8	31.8

piece - 4.84m)						
Small stack (3 piece - 4.84m)	16:40	85	2.5	S	412.5	32.31
Small stack (3 piece - 4.84m)	16:50	51	2	S	420.5	32.19
SEPTEMBER 27TH						
Green tank	09:28	170	2.5	SSE	446.2	12.65
	09:58	85	2.8	SSE	414.5	12.68
	10:09	0	2	SSE	428.8	14.5
	10:19	340	2.6	SSE	411.1	15.03
	10:31	8.5	2.4	SSE	425	15.91
	10:35	51	2.4	SSE	417	16.53
	10:48	34	2.2	SSE	417.5	17.18
Green tank reversed hose orientation	11:08	34	1.8		412	21.14
	11:21	51	1.9	S	410.1	24.83
	11:29	8.5	2.8	S	423.6	26.46

	11:38	340	2.1	S	410.4	27.77
	11:50	0	2.2	S	429.4	28.49
	11:58	85	3	S	414.2	29.95
	12:08	170	1.5	S	416	31.65
Short stack, 1.7 height	14:23	1690	1.5	SW	384.4	39.64
	14:36	34	2.5	SW	428	35.5
	14:44	710	2.5	W	423.5	37.7
	14:51	8.5	3	W	430.4	38.2
	14:58	0	3	W	0	0
	15:08	1200	2.5	W	413.5	39.59
	15:14	51	3	W	430	39.04
	15:20	170	1.4	W	421.3	38.89
	15:26	85	3	WSW	424.5	39.63
	15:32	340	1.2	W	427.7	39.52
	15:40	1350	1.5	WSW	402.4	40.03
	15:50	51	1.4	W	453.2	37.29
	15:59	8.5	1.5	W	442.9	39.05
	16:06	0	3.1	W	437.8	39.17
	16:13	710	3.2		420.6	38.26
	16:21	51	2.5	WSW	430.8	37.55
	16:29	8.5	3.1	W	431	38.08
	16:36	710	1.5	SW	421.3	38.05
	16:44	51	0	NA	429.5	38.25

	16:50	8.5	1.2	N	428	38.78
	17:00	710	1.7	W	424.4	38.25
SEPTEMBER 28TH						
1.7m stack	09:23	1350	1.7	S	338.6	16.92
	09:32	1200	0	NA	383.3	18.56
	09:47	1690	1.7	SSW	358.9	19.12
	09:57	1200	0	NA	386.3	16.03
	10:07	1690	1.2	SE	306.7	17.01
	10:15	1350	1.6	S	384.1	16.86
	10:29	1690	1.2	SW	393.2	22.93
	10:39	1350	0.6	SW	361.8	23.2
	10:47	1200	1.1	SE	381.6	23.21
Tall 3- piece stack	11:06	1200	1.4	SW	421.1	29.2
	11:23	340	1.8	S	438.1	27.44
	11:28	0	0.8	SE	538.7	29.19
	11:36	85	1	S	460.7	30.77
	11:45	170	1.7	SSW	447.9	32.76
	11:51	1690	1.5	SW	385.5	34.97
Medium 2-piece stack	13:17	1200	0.9	S	409.1	38.51
	13:36	340	2.4	SE	431.3	34.68
	13:43	0	2.7	SE	466.2	35.71
	13:51	85	1.5	SW	430.9	35.43

	13:58	170	2	SW	437.1	36.17
	14:05	1690	2.2	SW	384.5	37.12
Vent from shack, tape on pipe	15:24	85	N/A	N/A	437.1	31.5
	15:30	51	N/A	N/A	436.5	31.77
	15:36	170	N/A	N/A	436	32.1
	15:44	0	N/A	N/A	440.3	32.92
	15:50	340	N/A	N/A	429.9	32.92
	15:57	8.5	N/A	N/A	437	32.77
Vent from shack, tape off	16:06	340	N/A	N/A	429.3	32.77
	16:14	170	N/A	N/A	432.5	33.59
	16:20	51	N/A	N/A	432	33.4
	16:25	85	N/A	N/A	433.5	33.53
SEPTEMBER 30TH						
Tall Flare Stack	12:55	340	2.3	NNW	431.2	27.38
	13:28	710	5.2	NW	436.4	31.92
	13:43	1200	6.5	NW	422.3	29.1
	13:48	1690	3.8	NW	396.7	26.47
	13:54	2720	3.3	NW	449.7	20.57
	14:00	1200	1	NNW	421.5	16.9
	14:02	1690	1.8	NW	406.9	18.32

	14:04	0	N/A	N/A	N/A	N/A
1.7m Stack	14:09	170	3.1	NNW	434.6	25.49
	14:17	1690	1.9	NNW	422.1	23.48
	14:23	340	3	N	452.9	27.6
	14:30	8.5	3.4	NNW	493.6	28.17
	14:35	0	N/A	N/A	N/A	N/A
	14:41	1200	3.3	N	441.2	28.72
	14:47	85	2	NW	461.1	28.83
	15:04	51	5	N	464.2	29.69
Flare stack	15:36	170	2.5	NNW	465.6	28.94
	15:44	0	4.3	NNW	92.9	27.31
	15:47	8.5	4.1	NNW	469	28.59
	15:54	85	3.7	NNW	458.4	29.48
	16:00	51	4	NNW	462.4	30.33
Short stack	16:10	51	3.6	NNW	465.6	28.96
	16:16	710	2.9	NW	445.3	26.14
	16:23	2720	3.4	NNW	360.7	22.14
	17:15	1350	3	NNW	419.7	21.12
	17:19	340	2	NW	436	20.58
	17:23	2720	3	NW	350.9	19.42
	17:27	51	2.5	NNW	457.1	17.17
	17:32	710	3.4	NNW	438.9	17.11

	17:37	170	2.5	NNW	450.6	17.47
OCTOBER 1ST						
Flare stack	10:25 :00	170	2.5	NE	439.1	24.98
Flare stack	10:35 :40	8.5	2.5	NE	422	23.93
Flare stack	10:44 :00	1200	2.5	NE	325.6	24.27
Flare stack	10:49 :30	340	1.6	NE	391.1	23.3
Flare stack	10:55 :40	51	2.2	NE	417.3	23.7
Flare stack	11:02 :10	85	2.5	NE	406.5	24.17
Flare stack	11:08 :35	0	1.8	NE	-	-
Flare stack	11:15 :40	710	2.1	ENE	410.7	26.39
Flare stack	11:23 :00	2720	2	ENE	314.6	25.24
Flare stack	11:30 :10	1690	2.1	ENE	384.7	17.11

1.4m stack	11:39 :40	1690	1.2	E	405.6	19.8
1.4m stack	11:46 :20	2720	0.5	E	335.2	18.59
1.4m stack	11:52 :30	710	0.1	ESE	414.5	18.07
1.4m stack	11:58 :00	0	1.4	ENE	-	-
1.4m stack	12:03 :50	85	0	N/A	427.6	22.9
1.4m stack	12:09 :20	51	1	NE	421.5	26.61
1.4m stack	12:16 :15	340	1	NE	427	30.13
1.4m stack	12:21 :50	1200	2.4	NNE	408.2	31.21
1.4m stack	12:28 :10	8.5	0	N/A	465.7	30.87
1.4m stack	12:33 :30	170	2.1	ENE		31.86
Tank (with wind)	14:20	170	1.5	NE	434.5	34.23

Tank (with wind)	14:31 :15	85	2.2	E	424	34.93
Tank (with wind)	14:40 :00	0	2	ESE	-	-
Tank (with wind)	14:47 :30	340	2.6	E	425.6	34.86
Tank (with wind)	14:55 :40	8.5	1.9	ENE	429.6	34.84
Tank (with wind)	15:02 :05	51	0.8	NE	432	34.57
Tank (with wind)	15:08 :35	34	2.3	E	427.1	34.93
flare stack	16:04	170	2.6	E	439.6	26.32
flare stack	16:15 :55	8.5	3.3	ESE	431.7	25.38
flare stack	16:23 :30	1200	2.6	SE	405.6	23.44
flare stack	16:28 :15	340	2.6	SE	430.3	23.25
flare stack	16:34 :00	51	2.4	SE	427.7	23.2

1.4 m stack	16:39 :40	0				
1.4 m stack	16:41 :35	340	2.0	SE	431.6	22.94
1.4 m stack	16:47 :35	2720	2.1	SE	305.2	22.01
1.4 m stack	16:53 :20	85	1.6	SE	431.4	19.77
1.4 m stack	16:59 :10	1200	1.9	SE	412.1	20.23